esa SP-1013

The Achievements of

ESA SCIENTIFIC SATELLITES

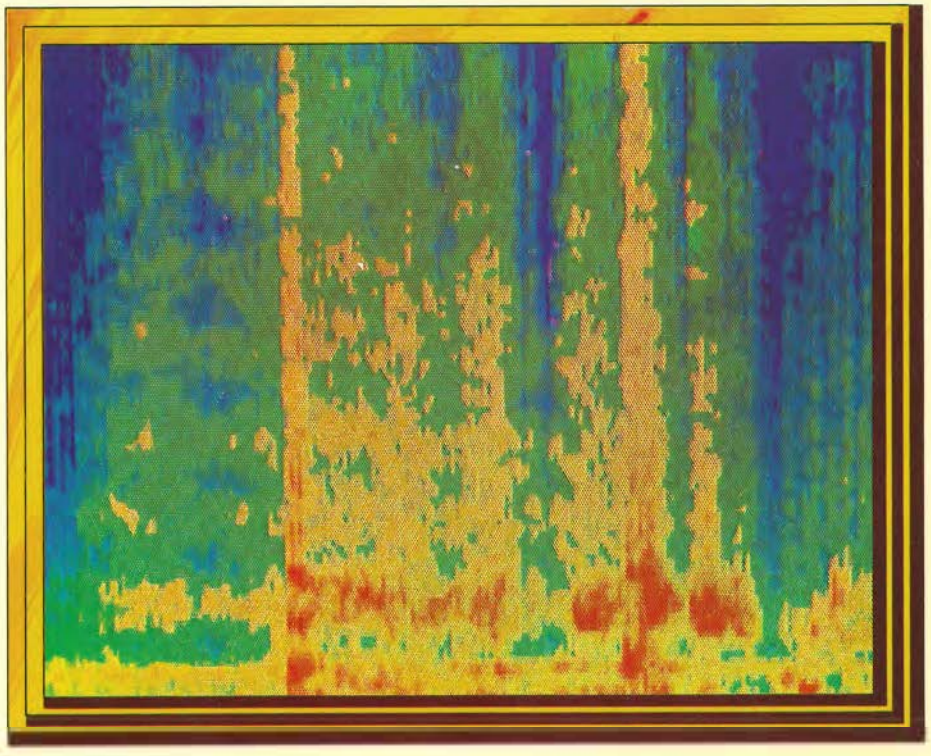

1968 1978

esa SP-1013
April 1979

The Achievements of

ESA Scientific Satellites

1968–1978

Prepared by:
ESA's Space Science Department

european space agency
agence spatiale européenne

Cover picture: *Information on magnetospheric waves observed on Geos-1 displayed on a colour television screen addressed by a computer. The result is a frequency/time plot in which intensity is colour coded: strong signals appear red, weaker signals blue.*

Frontispiece (p. 4): *Contours of high-energy gamma-ray emission from the Milky Way as measured by Cos-B, drawn in the galactic coordinate system.*

Published by: *ESA Scientific & Technical Publications Branch* (*April* 1979).

Printed at: *ESTEC, Noordwijk, The Netherlands*

Distribution Office: *ESA Information Retrieval Service*,
8-10, *rue Mario-Nikis*, 75738 *Paris*

Price Code: E2 (75 FF).

Contents

Introduction

With the launch of Geos-2 in July 1978, the European Space Agency began its twelfth consecutive success story (Table 1). Technically, all the spacecraft put into orbit have performed sufficiently well to enable the intended missions to be accomplished, and no experiment on which a mission was critically dependent has suffered catastrophic failure. Indeed the technical performance of the scientific packages developed in national institutes has been extremely good and has at least equalled the performance of the spacecraft subsystems developed in industry.

The reports contained in this book aim to describe what was hoped for when each of the first nine satellites was planned, to list the experiments carried and to summarise some of the most important scientific achievements.

The ESA effort in this field appears so small in comparison with the programmes of the USA and the USSR that we are frequently asked whether it makes sense for ESA to compete at all. It may be that the first two ESA satellites (ESRO-2 and ESRO-1, launched by NASA free of charge) uncovered few startlingly new phenomena, but they certainly did make significant scientific contributions, especially in the case of co-ordinated studies in which their data were combined with those obtained from HEOS-1.

From HEOS-2 on, however, it can fairly be claimed that each spacecraft has made a unique and novel contribution. Perhaps the easiest to describe in a dramatic way are the achievements of Cos-B, that star performer now well into its fourth year of operation and helping to unravel the mysteries of the gamma-ray sky.

A feature of the ESA programme right from the outset has been the willingness of most experimenters to share data and derive maximum advantage from co-ordinated studies. It may be that in this aspect, and in squeezing maximum science from the available raw data, Europe has done slightly better than other parts of the world. In some cases the absence of new flight opportunities may

Table 1. *ESRO ESA Scientific Satellites launched* (1968–1978)

Satellite	Launch date	End of useful life	Mission
ESRO-2	May 1968	May 1971	Cosmic rays, solar X-rays
ESRO-1A	October 1968	June 1970	Auroral and polar cap phenomena, ionosphere
ESRO-1B	October 1969	November 1969	As ESRO-1A
HEOS-1	December 1968	October 1975	Interplanetary medium, bow shock
HEOS-2	January 1972	August 1974	Polar magnetosphere, interplanetary medium
TD-1	March 1972	May 1974	Astronomy (UV, X- and gamma-ray)
ESRO-4	November 1972	April 1974	Neutral atmosphere, ionosphere, auroral particles
Cos-B	August 1975		Gamma-ray astronomy
Geos-1	April 1977	July 1978	Dynamics of the magnetosphere
ISEE-2	October 1977		Sun Earth relations and magnetosphere
IUE	January 1978		Ultraviolet astronomy
Geos-2	July 1978		As Geos-1

Table 2. *Number of publications up to June* 1978 *based on the results of ESA's scientific satellites*

Satellite	Publications
ESRO-2	45
ESRO 1A & B	128
HEOS-1	113
HEOS-2	103
TD-1	154
ESRO-4	96
Cos-B	53
Geos-1	44

even be an advantage! Each year ESA uses the occasion of the COSPAR meeting to prepare a fairly comprehensive report, which presents the main results of its scientific satellite programme. The report of June 1978 (*ESA SP*-1007) *includes a cumulative bibliography listing publications based on ESA satellite results* (*Table* 2).

The scientific results for Geos-2, *ISEE and IUE are just beginning to appear, and it is clear that even if these missions were to be unfortunately terminated at this stage, major new scientific results would continue to be published for years to come. It is hoped that these results will be summarised too in a future edition of the present document.*

In compiling reports like those which follow, ESA's Space Science Department staff depend heavily on the goodwill of those European scientists who have built the experiments and analysed the data. Summaries tend to be arbitrary and subjective and the material finally appearing may not do justice to many who have contributed to the overall success. We gratefully acknowledge the co-operation we have received.

I would like finally to mention those ESA project scientists who contributed in years past but who no longer find themselves in positions to write the summary reports. These were in particular Drs R Jaeschke (*ESRO*-1), *B G Taylor* (*HEOS*) *and J van Boeckel* (*TD*-1).

ESRO-2

Cosmic rays & solar particles

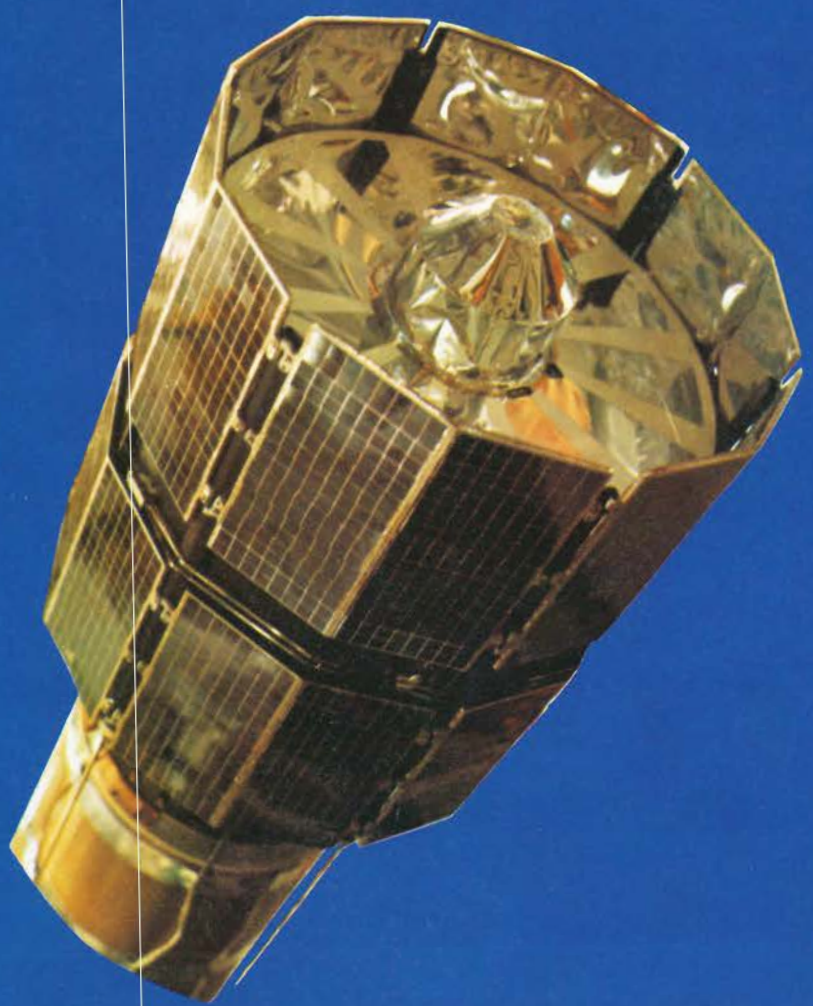

ESRO-2/Iris was the first of ESRO/ESA's satellites to be launched. An earlier attempt to orbit the flight model in 1967 *failed because the launch vehicle broke up. The re-furbished prototype was successfully placed in orbit by a NASA launcher from the Western Test Range, California, on* 17 *May* 1968. *It re-entered the atmosphere on* 8 *May* 1971 *after completing* 16 282 *orbits.*

Scientific mission

The spacecraft carried seven experiments (Table 1) the main missions of which were:

1) to study solar X-radiation in order to reach a better understanding of processes on the Sun itself and to correlate X-ray variations with heating and ionisation of the Earth's atmosphere;
2) to investigate high-energy particles from the Sun and the Galaxy in order to study particle propagation in space and the configuration of the magnetosphere;
3) to measure the electron component of primary cosmic radiation in order to obtain information to help with an evaluation of galactic magnetic fields.

Orbit and spacecraft

To fulfil the requirements of the scientific mission, the orbit was chosen to be near polar, 98° retrograde (always sunlit) and to follow the Earth's terminator. The apogee was approximately 1100 km and the perigee about 350 km. The spacecraft was spin-stabilised, rotating at about 40 rpm. A magnetorquer system was carried to maintain the spin axis perpendicular to the Earth/Sun line and parallel to the Earth's spin axis.

The spacecraft itself was a 12-sided prism, 78 cm in diameter and 86 cm in length (Fig. 1). Solar cells mounted on the 12 flat sides of the external surfaces provided 31 W of power at the beginning of life. The total weight was 84.6 kg (including 20.4 kg of experiments). This simple structural design, which proved to be successful for ESRO-2, was re-used for ESRO-4 with some minor modifications and was the basis for the design of ISEE-B.

Table 1. ESRO-2/Iris experiments

Experiment	*Investigating Group*	*Measurement*	*Technique*
S25	Imperial College, London (A Bewick)	Time variations in the radiation belt population.	Two Geiger-Müller counters with different geometric factors.
S27	Imperial College, London (R J Hynds)	Solar and radiation belt protons and alpha particles, protons in energy range 1-100 MeV.	Telescope of four surface barrier solid state detectors interspersed with copper absorbers.
S28	Imperial College, London (A C Durney)	High-energy solar protons and α particles both in the rigidity range 0.4-0.8 GeV.	Telescope using scintillator, proportional counters and Cerenkov techniques.
S29	University of Leeds (P Marsden)	The flux and energy spectrum of high energy primary electrons (1-13 GeV).	Gas Cerenkov detector to reject protons followed by lead-scintillator sandwich to identify electrons.
S36	University College, London, Leicester University (M L Shaw & P Stanford)	Solar X rays, 1-20 Å	Proportional counters with varying window thickness.
S37	Laboratorium voor Ruimteonderzoek, Utrecht (B Brinkman)	Solar X rays, 44-60 Å	Proportional counters with thin mylar windows.
S72	CENS, France (J Engelmann)	Solar and galactic protons (35 MeV–1 GeV) and α particles (140-1200 MeV).	Telescope of 2 solid-state detectors surrounded by a plastic scintillator anti-coincidence shield.

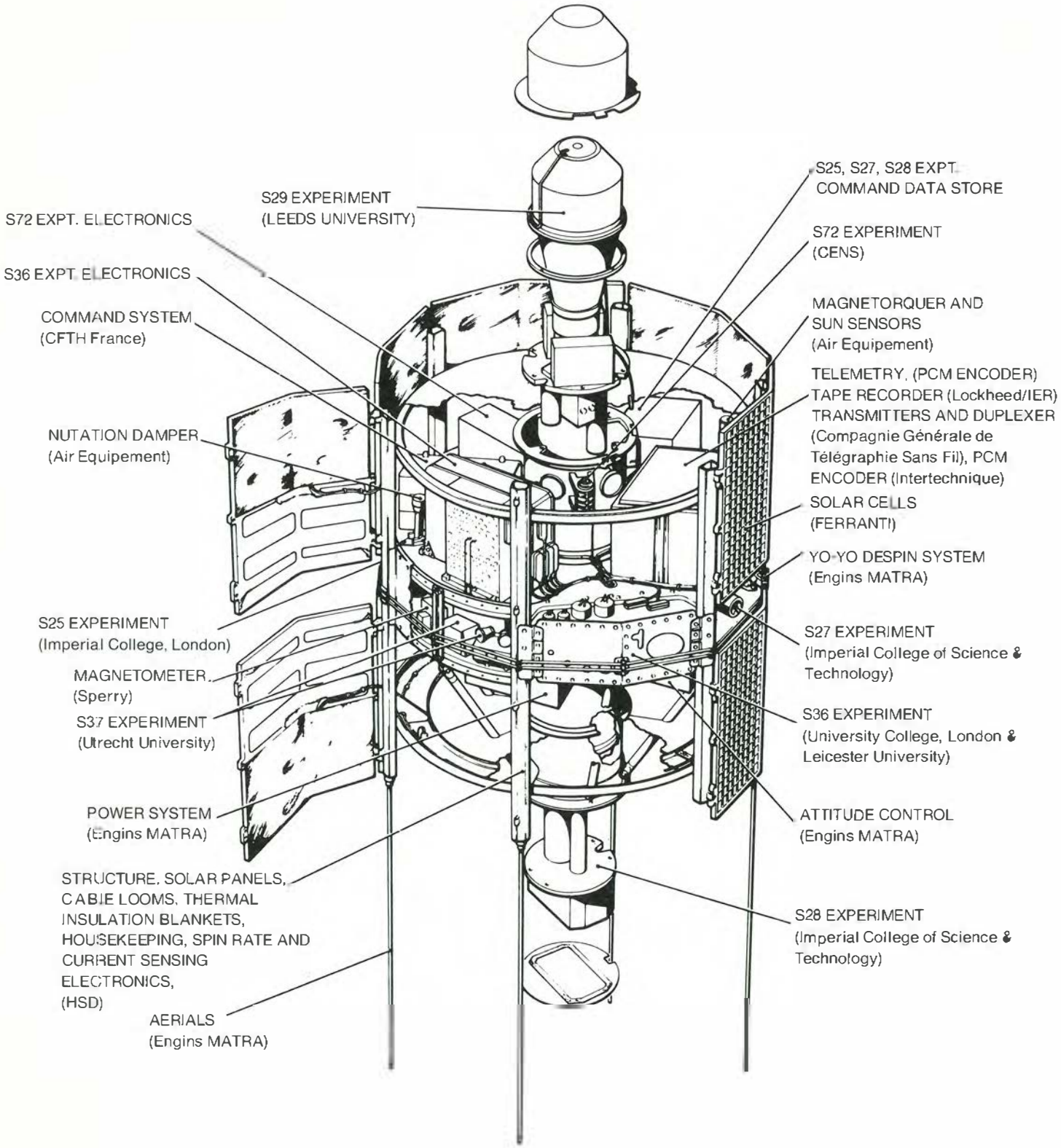
S72 EXPT. ELECTRONICS
S36 EXPT. ELECTRONICS
COMMAND SYSTEM
(CFTH France)
NUTATION DAMPER
(Air Equipement)
S25 EXPERIMENT
(Imperial College, London)
MAGNETOMETER
(Sperry)
S37 EXPERIMENT
(Utrecht University)
POWER SYSTEM
(Engins MATRA)
STRUCTURE, SOLAR PANELS,
CABLE LOOMS, THERMAL
INSULATION BLANKETS,
HOUSEKEEPING, SPIN RATE AND
CURRENT SENSING
ELECTRONICS,
(HSD)
AERIALS
(Engins MATRA)
S29 EXPERIMENT
(LEEDS UNIVERSITY)
S25, S27, S28 EXPT.
COMMAND DATA STORE
S72 EXPERIMENT
(CENS)
MAGNETORQUER AND
SUN SENSORS
(Air Equipement)
TELEMETRY, (PCM ENCODER)
TAPE RECORDER (Lockheed/IER)
TRANSMITTERS AND DUPLEXER
(Compagnie Générale de
Télégraphie Sans Fil), PCM
ENCODER (Intertechnique)
SOLAR CELLS
(FERRANTI)
YO-YO DESPIN SYSTEM
(Engins MATRA)
S27 EXPERIMENT
(Imperial College of Science &
Technology)
S36 EXPERIMENT
(University College, London &
Leicester University)
ATTITUDE CONTROL
(Engins MATRA)
S28 EXPERIMENT
(Imperial College of Science &
Technology)

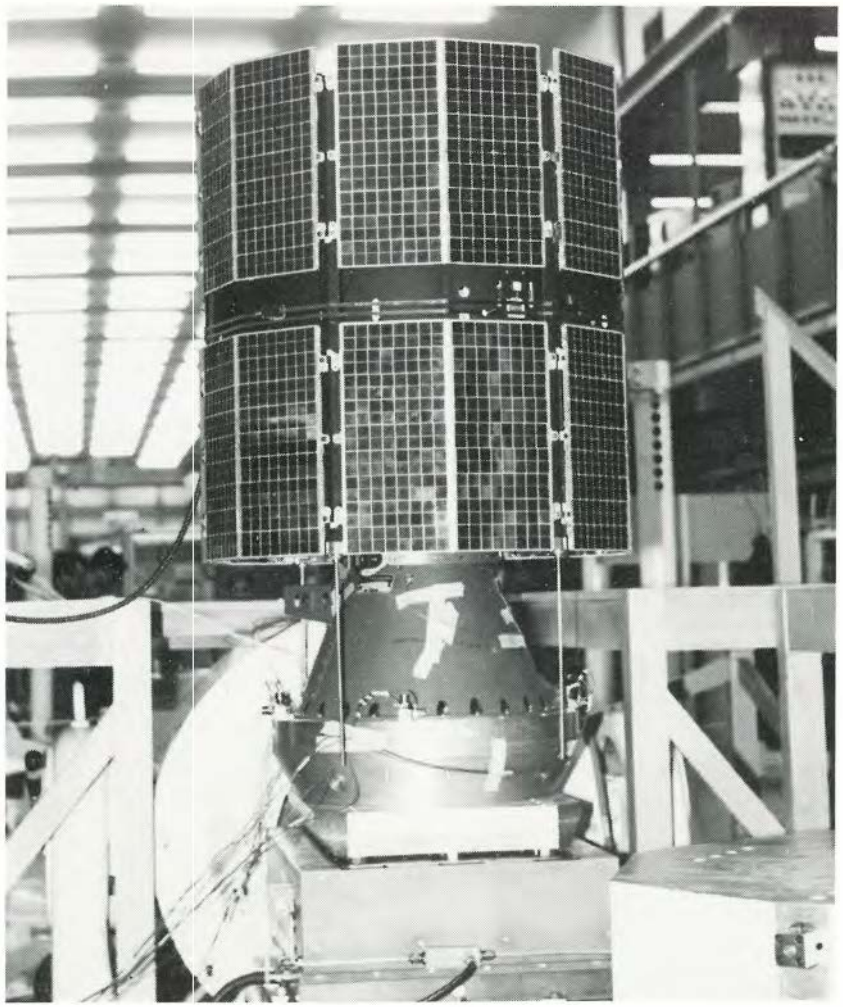

Figure 1. ESRO-2 Iris flight unit 2 on the vibration table (1967).

Performance in orbit

Early in December 1968, after $6\frac{1}{2}$ months of operation, a drive-belt breakage put the tape recorder out of action. Previous to this the data recovery rate was more than 90%, and during some periods reached 98%. After the failure, recovery was restricted to real-time data only and dropped to 20%. It was maintained at that level by intensive effort during about a year, but after May 1970, it was allowed to drop further. In the absence of tape recordings, the best acquisition area was over the northern polar cap, where the Tromsø, Spitzbergen and Fairbanks stations gave fairly comprehensive coverage, except for an embarrassing gap between the last two stations.

The tape-recorder failure was catastrophic for the scientific mission of experiments S36 and S37. The main interest of the other experiments was in high-latitude measurements, so they were fortunate in having the high-latitude stations available. Good coverage of the northern polar cap enabled the experimenters to correlate ESRO-2 observations with HEOS-1 measurements during the solar-flare events of 25 and 27 February 1969.

On re-entry after three years in operation, four of the seven experiments (S25, S28, S29 and S72) were still operating well. Experiments S36 and S37 had not given any significant data return since the loss of the tape recorder, and S27 had been switched off after the front solid-state detector in its telescope had failed.

Achievements

The most interesting data provided by ESRO-2 have now been analysed. Little new material has been published in the literature in the past four years. The following is a summary of the most important scientific results.

The analysis of the data is notable for the high degree of co-operation between experimenters of similar interest. For example, several papers were produced as a result of the combined efforts of workers on S25, S27, S28 and S72. The experimenters were fortunate in that HEOS-1 was able to supply interplanetary observations at the same time (although not until mid-December 1968, i.e. after the tape recorder failure), which permitted a fine analysis of the events in February 1969. Data from ESRO-1A and ESRO-1B were also used in some of the papers on particle precipitation.

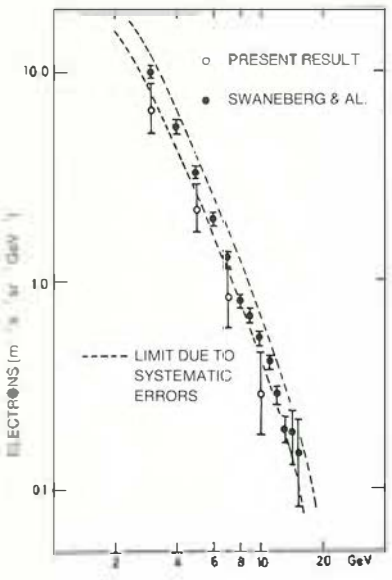

Figure 2. The primary-electron spectrum obtained by Leeds University on ESRO-2 compared with the previous best results obtained by Swaneberg & al.

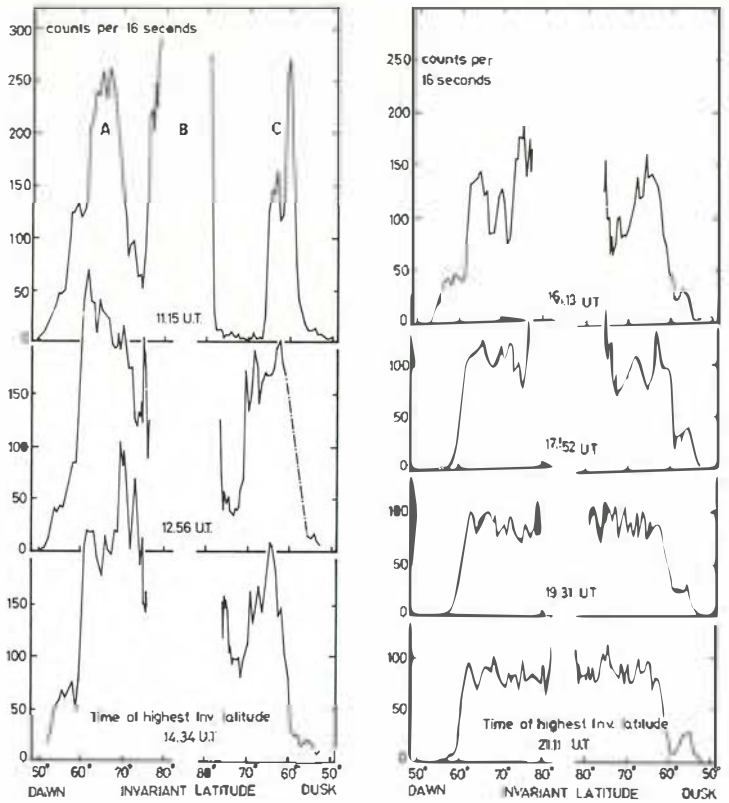

Figure 3. Northern polar-cap observations of the time variation of the intensity structure of 90-350 MeV protons made on 18 November 1968 from ESRO-2. The first seven northern polar-cap passes after the flare are shown. The spacecraft was approximately following the dawn dusk meridian at this time.

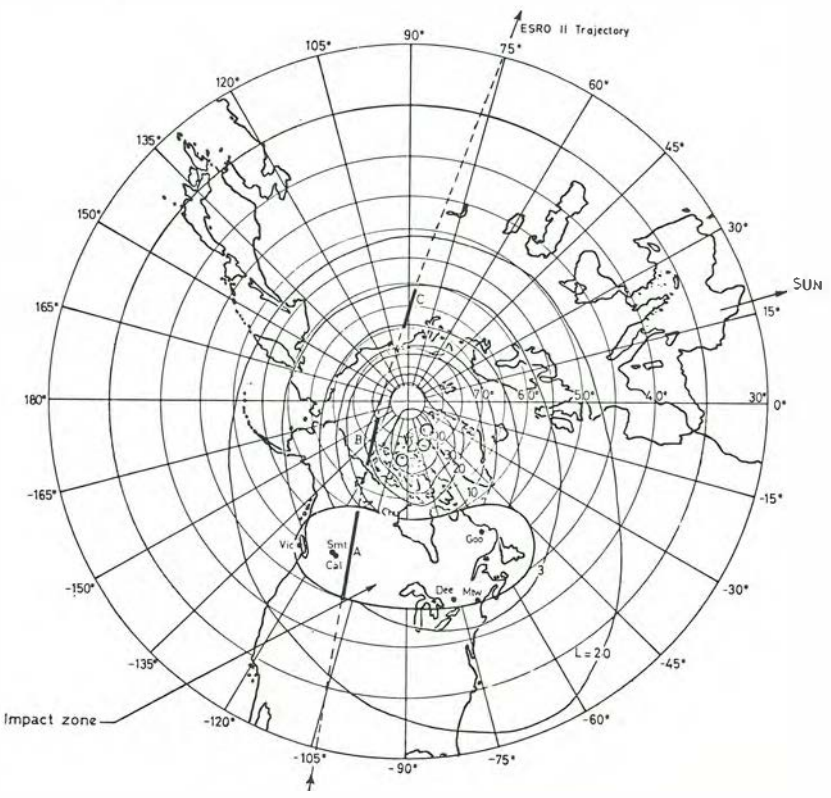

Figure 4. Trajectory of ESRO-2 during the first pass over the northern hemisphere after the flare of 18 November 1968. The heavily lined parts of the trajectory are the approximate positions of peaks A. B and C shown in Figure 3. The impact zone observed by neutron monitors on this date is illustrated; notice the correlation of this zone with peak A.

X-ray flares

The two experimenter groups with X-ray instruments combined to analyse in detail a 'gradual-rise-and-fall' (GRF) solar X-ray event that occurred on 6 July 1968. Experiment S36 covered the spectral range between 1 and 18 Å and experiment S37 covered the 44–55 Å range, thus making the measurements complementary. GRF events had previously been assumed to result from the superposition of two or more flares. Careful examination of the profile of the July event, however, when combined with theoretical calculations, led to the conclusion that this event at least was the result of emission from the flare itself followed by emission from the loop prominences associated with the flare and perhaps emission from sources behind the solar limb.

Models for free-free continuum and line emission due to thermal plasmas combined with the assumption that radiation in the source region was thermal made it possible to obtain temperatures and emission measures versus time figures. It was shown that in the 2.2-3.0 Å band the cooling rate of the corona associated with the prominences was compatible with an electron density of $1 \times 10^{11}/cm^3$ if a single injection of particles into the corona was assumed. A value of 2×10^{10} electrons/cm^3 was found for the 5.8–8.8 Å band. These figures allowed an estimate of the injected energies to be made which was found to be approximately 10^{29} ergs for the 2.2–3.0 Å band and 4×10^{31} ergs for the 5.8–8.8 Å band.

Primary electron spectrum

The Leeds University experiment (S29) was designed to measure the spectrum of primary electrons in the 1–13 GeV energy range. The spectrum shown in Figure 2 is the result of careful calibration and the analysis of 2000 orbits. Electron measurements in space have proved to be very difficult, mainly because of the unknown background radiation. It is therefore not always easy to decide whether differing answers obtained from different spacecraft should be attributed to instrumental effects or to long-term variations. For this reason the extended lifetime of ESRO-2 was useful in that the same detector was available to monitor possible changes with time. None were found.

Penetration of solar particles into the magnetosphere

Undoubtedly the most fruitful ESRO-2 studies have been those on the arrival of solar particles at high latitudes. The observations have clearly shown the striking variations of intensity that can occur over the polar cap. An example of these is shown in Figure 3 where ~100 MeV proton intensities are plotted against invariant latitudes for seven successive passes over the northern polar cap immediately following the flare on 18 November 1968. This figure was plotted straight from the raw data of S28 and is still a classic of its kind. Figure 4 shows the trajectory of the first ESRO-2 pass over the northern hemisphere immediately following the flare and illustrates how the spacecraft crossed the impact zone as registered by neutron monitors. The heavily lined parts of the trajectory show where the ESRO-2 counting rates were enhanced.

The particle-counting instruments on board the spacecraft were arranged to give a good coverage of the proton energy spectrum. Results of the four particle experiments are plotted together in Figure 5, for data taken after the flare on 25 February 1969. The analysis concentrated on two periods, the one following the flare of 18 November 1968 and the other covering the active period of 25-28 February 1969. Although the tape recorder had failed by the time the February observations were made, good coverage was achieved by the tracking stations in the northern polar cap. The third ESLAB/ESRIN Symposium (Noordwijk, September 1969) was dedicated to the latter observation period.

A trajectory plotting programme was developed at Imperial College in order to discover how the solar protons entered the magnetosphere, and this proved a very powerful tool when applied to the data. It was demonstrated conclusively that a large number of energetic solar protons reach the polar cap via the tail. ESRO-2 was not able to show how these particles gained access to the tail, but a computer analysis using some likely magnetic configurations did produce a type of trajectory that could reverse the direction of the particles and inject them onto the tail field lines. This technique gave a good description of the intensity variations across the tail and accounted for the gross features in the observations such as those shown in Figure 3. The Imperial College group followed up the 'spin-off' from these correlations and pointed out that invariant latitude versus magnetic local time (MLT) is not a suitable co-ordinate system for studying polar cap phenomena. They proposed a co-ordinate system based on trajectory calculations. By following trajectories of particles from their point of entry into the tail, along the tail and down onto the polar cap region, it is possible to map out – into an invariant latitude-MLT plot – the contours representing the regions of entry into the tail of the particles

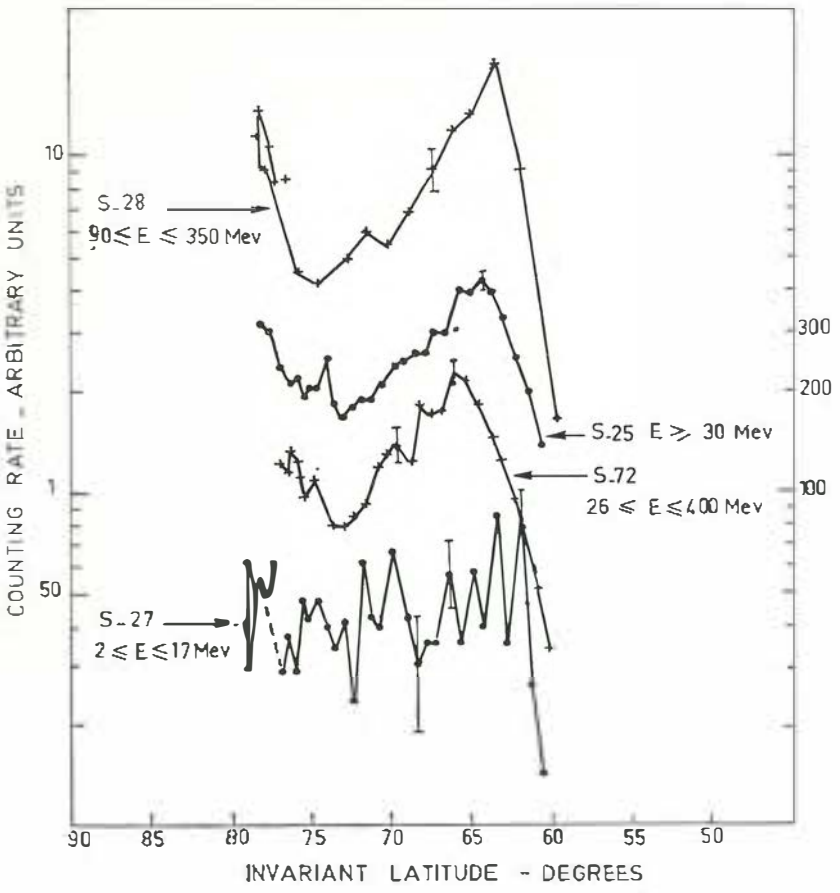

Figure 5. Proton counting rates as a function of invariant latitude over the northern polar cap for four different detectors on ESRO-2 for the period 1048 to 1101 UT on 25 February 1969. The energy range covered is 2–400 MeV.

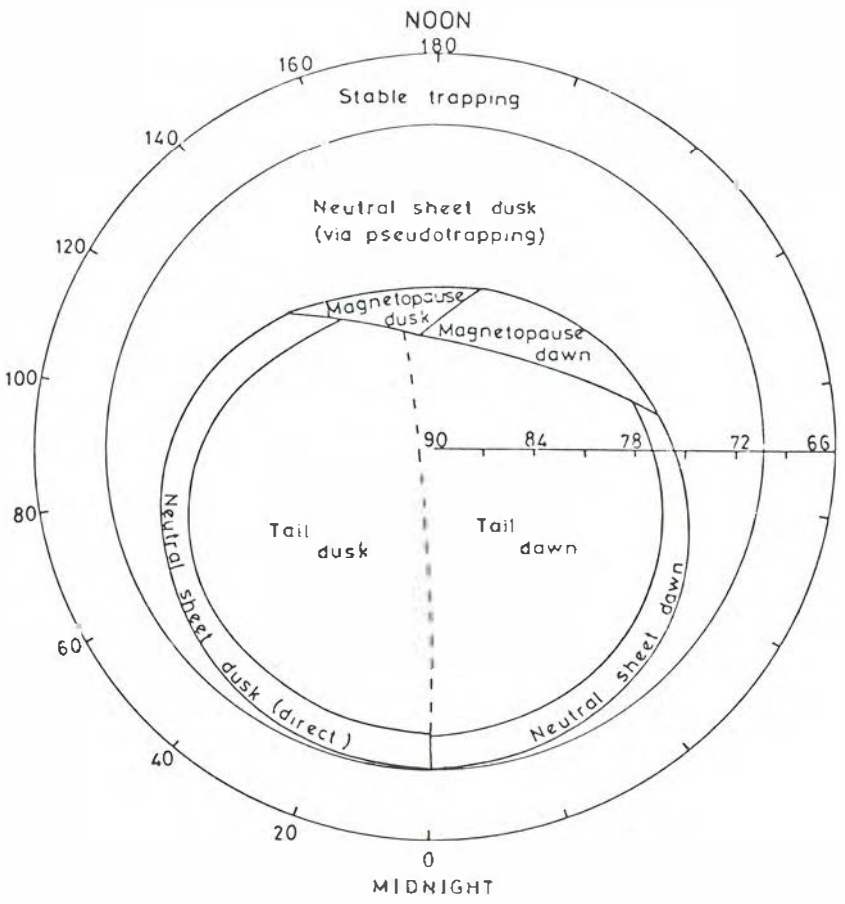

Figure 6. An invariant latitude vs. magnetic local time plot with contours mapped onto it showing the entry regions into the magnetotail for protons of 3.4 MeV. The magnetic field model used is that of Williams & Mead (1965), with a tail field strength of 12.5 γ.

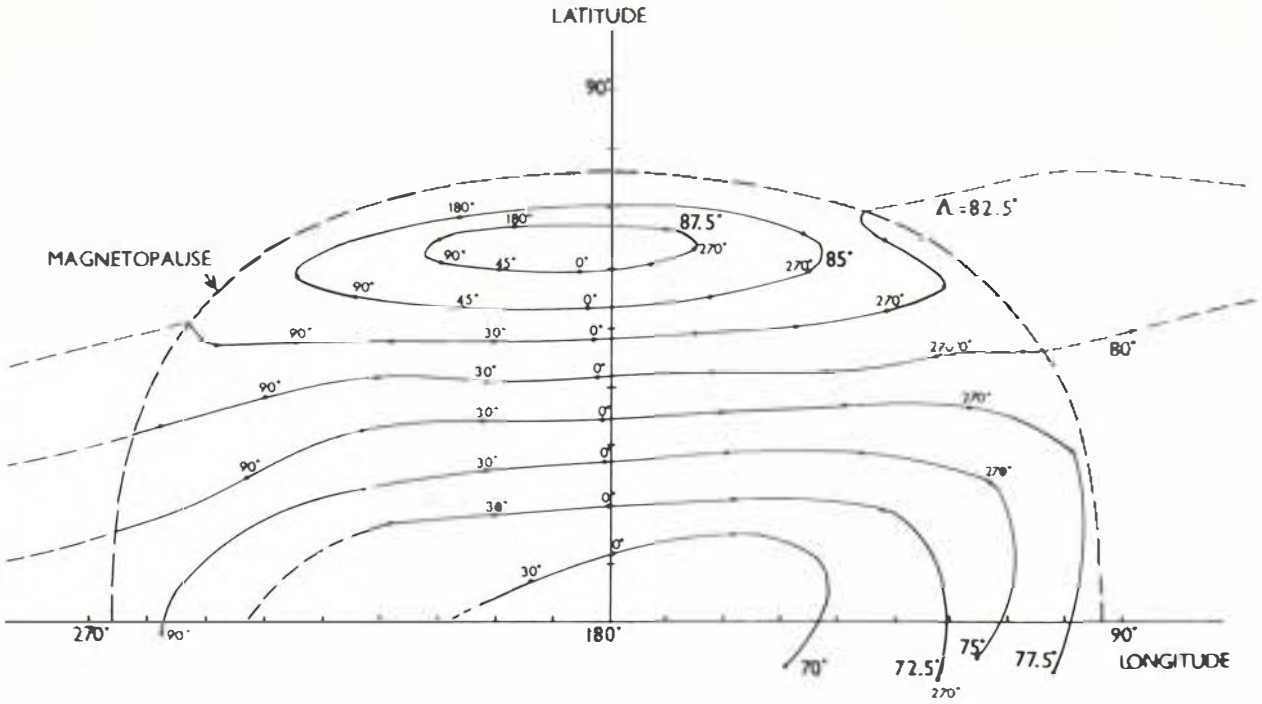

Figure 7. Projection of an invariant latitude vs. magnetic local time plot onto a cross-section of the tail, at a distance of 15 R_E. The tail field strength used in this case was 40 γ. Contours are labelled with the values of the invariant latitude Λ and each contour has marked on it values of the geomagnetic longitude. The vertical and horizontal axes represent latitude and longitude in solar magnetospheric co-ordinates.

observed over the polar cap region (Fig. 6). Alternatively by tracing these trajectories backwards from the polar cap region, an invariant latitude-MLT plot of the polar cap region can be projected onto a cross section of the tail, as in Figure 7 for example. These ideas were checked and found to produce sensible answers for a number of questions raised by polar spacecraft observations. Ultimately, the group deduced that, although the reconnection theory was correct in essence, the transfer of high-energy particles into the tail was by a nonadiabatic mechanism, and not by adiabatic motion along the field lines.

Other authors have disagreed with these theories and have suggested different entry mechanisms, for example, via the neutral sheet. Whatever mechanisms are proposed, ESRO-2 observations still provide some of the best tests for the theories.

A different line of analysis has been used by some of the particle instrument investigators, who have investigated the stable and pseudo-trapping boundaries. Figure 8 shows contours of flux versus time constructed by using Geiger counter results for passes over the southern polar cap on 9 June 1968. These contours demonstrated the time persistence of peaks in the flux. The peaks are divided into two types by superposition of the pseudo-trapping

Figure 8. Data from 22 passes over the southern polar cap are summarised by contours of constant flux of 2-17 MeV protons. Contours are labelled in units of 200 counts/15.9 s. Each satellite pass corresponds to a vertical line passing through an inverted T symbol which also marks the highest latitude reached by that pass. Solid dots mark the measured boundary of stably trapped electrons of energy greater than 1.2 MeV. Open circles mark the intersection of the orbits with the calculated pseudo-trapping boundary.

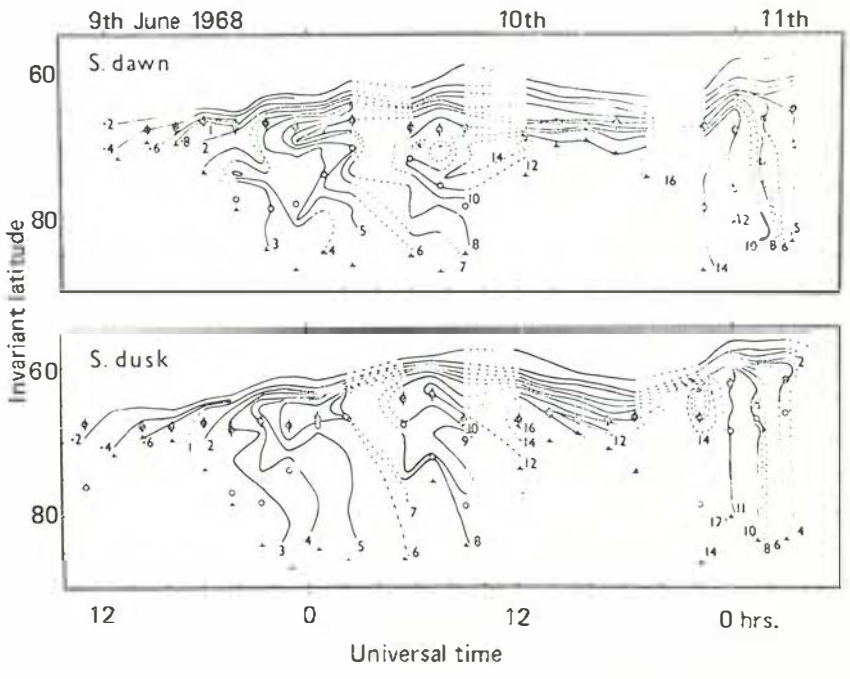

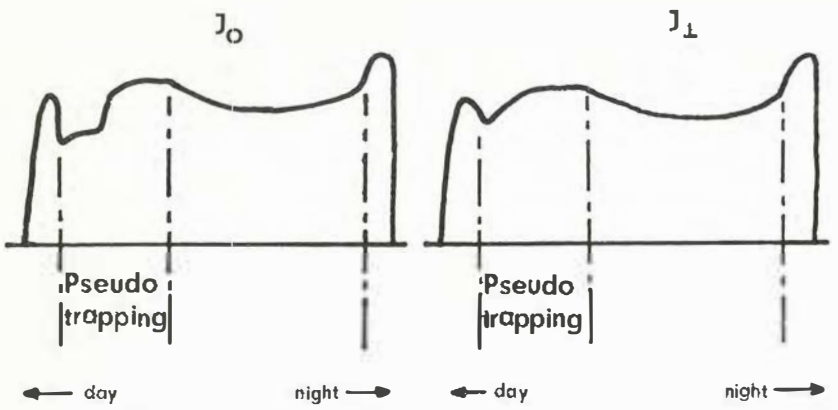

Figure 9. A schematic diagram showing the flux profiles expected on a noon midnight meridian low-altitude satellite pass. J_o represents the omnidirectional flux, and $J_\perp$ the flux at right angles to the field line. The vertical dashed lines mark the stable trapping and pseudo-trapping boundaries. Knowing the shape of the pseudo-trapping region, one can deduce the profile to be expected in any other orbit.

and stable trapping regions (from trajectory calculations). From this it was deduced that there was delayed access of solar protons into the tail; the pseudo-trapping region was filled with protons entering via the neutral sheet; isotropy at higher pseudo-trapping latitudes is maintained by a breakdown of the adiabatic invariant which is indistinguishable from strong pitch-angle scattering effects; there is weak scattering at lower pseudo-trapping latitudes, which releases particles into the atmosphere. These findings are summarised in Figure 9 which shows schematics of the flux-intensity profiles that would be expected in the pseudo-trapping region if these findings were correct.

Conclusions

ESRO-2 observations and the 'spin-offs' from the analyses have contributed significantly to our knowledge of the Earth's environment and the processes that occur in the magnetosphere. Most of the recent papers that quote ESRO-2 measurements have not been written by the experimenters, but by other workers in the field who use the measurements to test their own theories and/or want to discuss the work of the ESRO-2 investigators.

A continuing dialogue of this kind, so many years after the spacecraft has re-entered the atmosphere, is the hallmark of a scientifically successful mission.

ESRO-1A & B

Auroral & polar phenomena & ionosphere

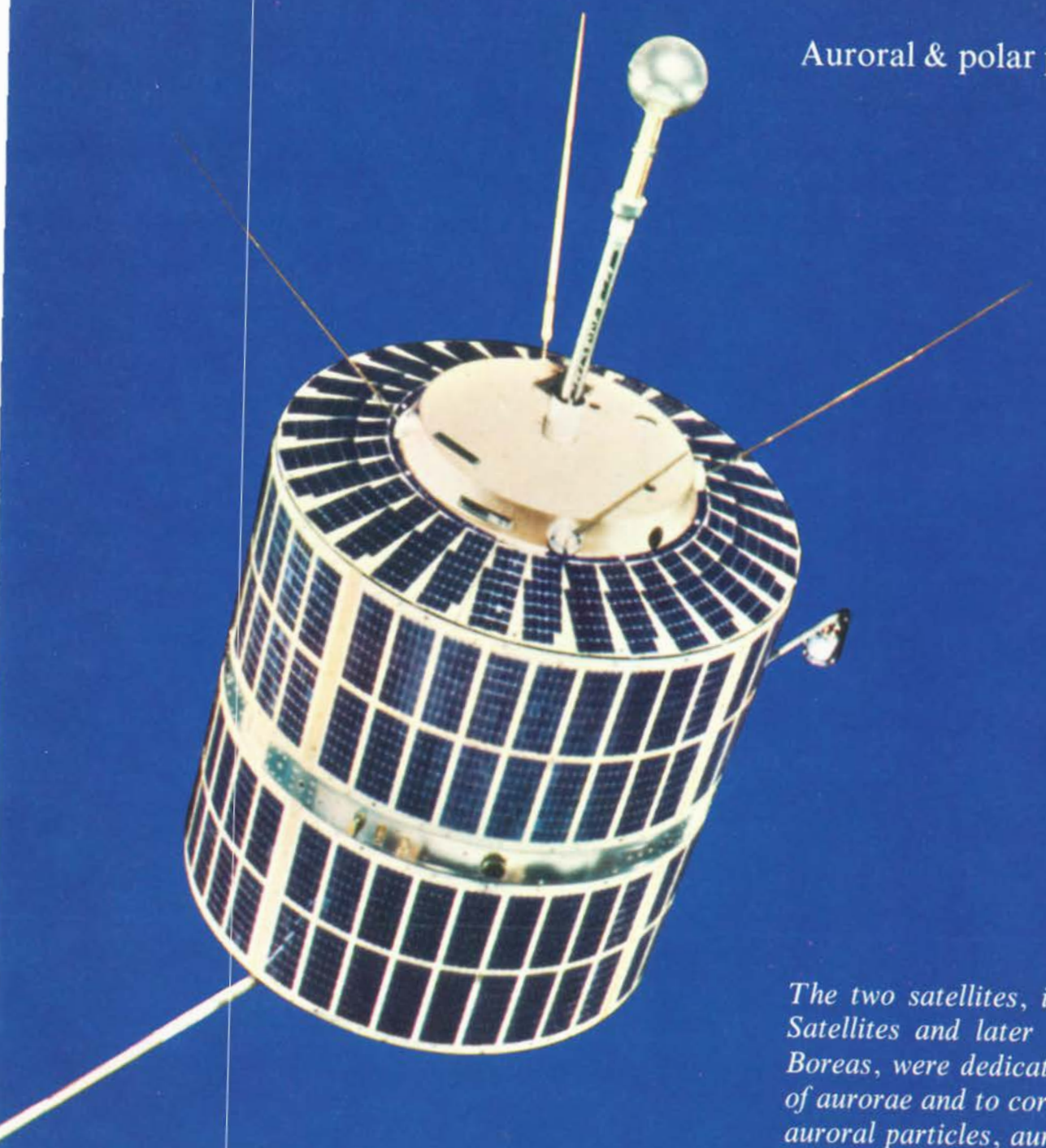

The two satellites, initially called Polar Ionosphere Satellites and later ESRO-1/Aurorae and ESRO-1/Boreas, were dedicated to studying the fine structure of aurorae and to correlating information on energetic auroral particles, auroral luminosity, and ionospheric composition and heating.

Scientific mission

Both satellites were near-polar orbiters and were magnetically stabilised in such a way that over the North Pole some of the particle experiments looked up along the magnetic field lines and some perpendicular to them, while two photometers looked down towards the Earth to map the occurrence of aurorae unhindered by meteorological conditions. Figure 1 shows the orientation of ESRO-1 and its experiment sensors above the northern polar region.

Spacecraft and experiments

The satellites' structure consists of a magnesium-alloy central cone, on which are secured four plates made of an aluminium honeycomb sandwiched between two magnesium plates, designed to carry the scientific payload. A brief description of the experiments incorporated in the payload and their aims is given in Table 1.

Table 1. ESRO-1 and 2 experiments

Experiment	*Scientific Group*	*Measurement*	*Technique*
S32	Norwegian Institute of Cosmic Physics, Oslo	Auroral luminosity at 4861 Å ($H\beta$) and at 4278 Å (N_2^+)	Two photometers with interference filters
S44	University College, London	Electron temperature and density in the ionosphere	Two boom-mounted, planar Langmuir probes
S45	University College, London	Ion composition and temperature in the ionosphere	Boom-mounted spherical Langmuir probe
S71A	Radio & Space Research Station, Slough	Trapped and precipitated electron flux and energy spectra (50-400 KeV)	Scintillator with pulse height analysis
S71B	Kiruna Geophysical Observatory	Trapped and precipitated electrons and protons (1-13 keV) with high time resolution	Electrostatic analysers followed by channeltrons
S71C	University of Bergen & Danish Space Research Inst., Lyngby	Trapped and precipitated protons (100 keV-6 MeV)	Three solid-state detectors
S71D	Norwegian Defence Research Establishment, Kjeller, and Danish Space Research Inst., Lyngby	Pitch angle distribution of electrons (>40 keV) and protons (>500 keV) with high time resolution	Four Geiger counters
Ratemeter	Space Science Dept. ESTEC	Trapped electrons (>40 KeV) and protons (>500 keV)	Analogue output from 90° Geiger counter
S71E	Radio & Space Research Station, Slough	Flux and energy spectra of solar protons (1-30 MeV)	Solid-state detector and scintillator telescope with half-angle of 30°

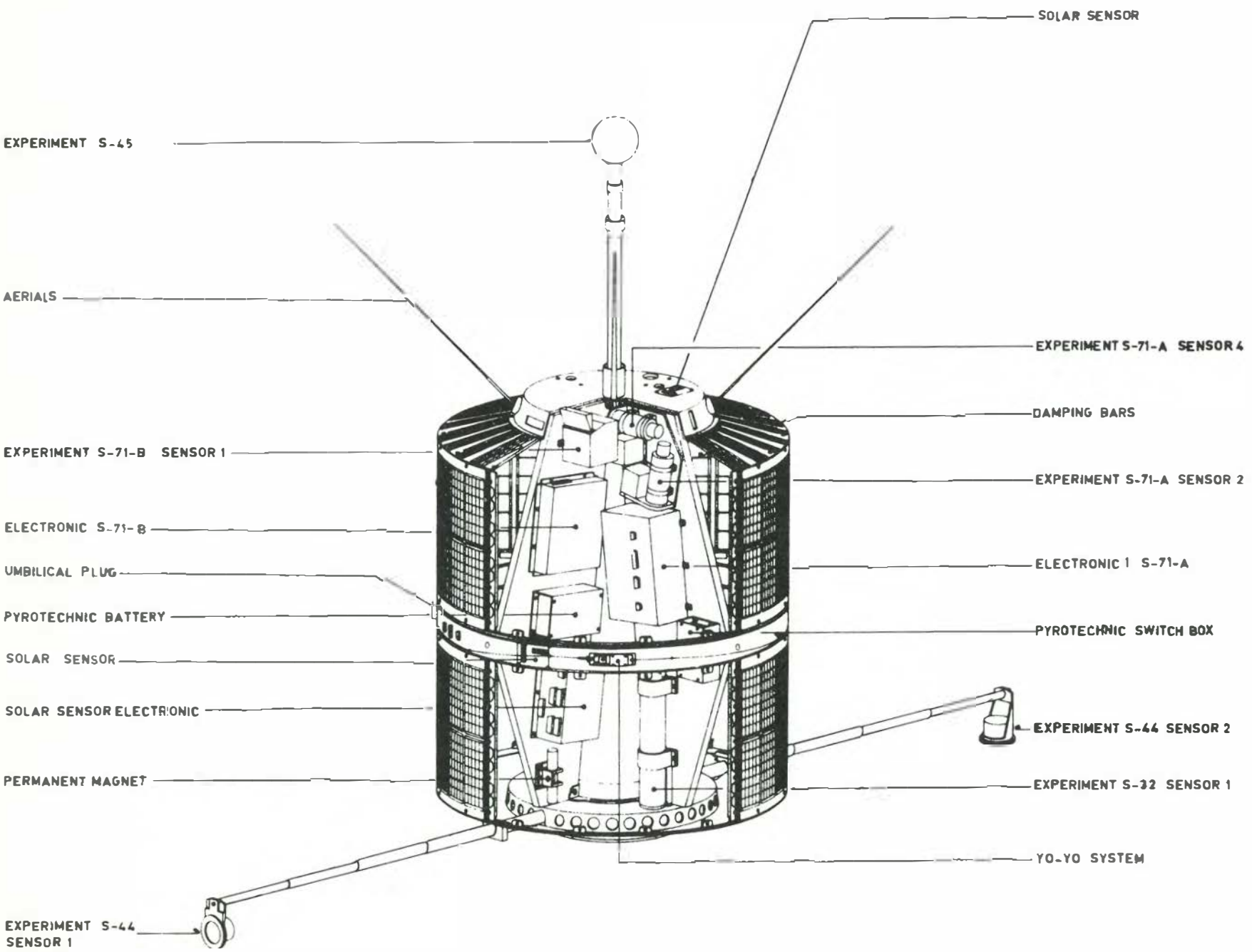
SOLAR SENSOR
EXPERIMENT S-45
AERIALS
EXPERIMENT S-71-A SENSOR 4
DAMPING BARS
EXPERIMENT S-71-B SENSOR 1
EXPERIMENT S-71-A SENSOR 2
ELECTRONIC S-71-B
ELECTRONIC 1 S-71-A
UMBILICAL PLUG
PYROTECHNIC BATTERY
PYROTECHNIC SWITCH BOX
SOLAR SENSOR
SOLAR SENSOR ELECTRONIC
EXPERIMENT S-44 SENSOR 2
PERMANENT MAGNET
EXPERIMENT S-32 SENSOR 1
YO-YO SYSTEM
EXPERIMENT S-44 SENSOR 1

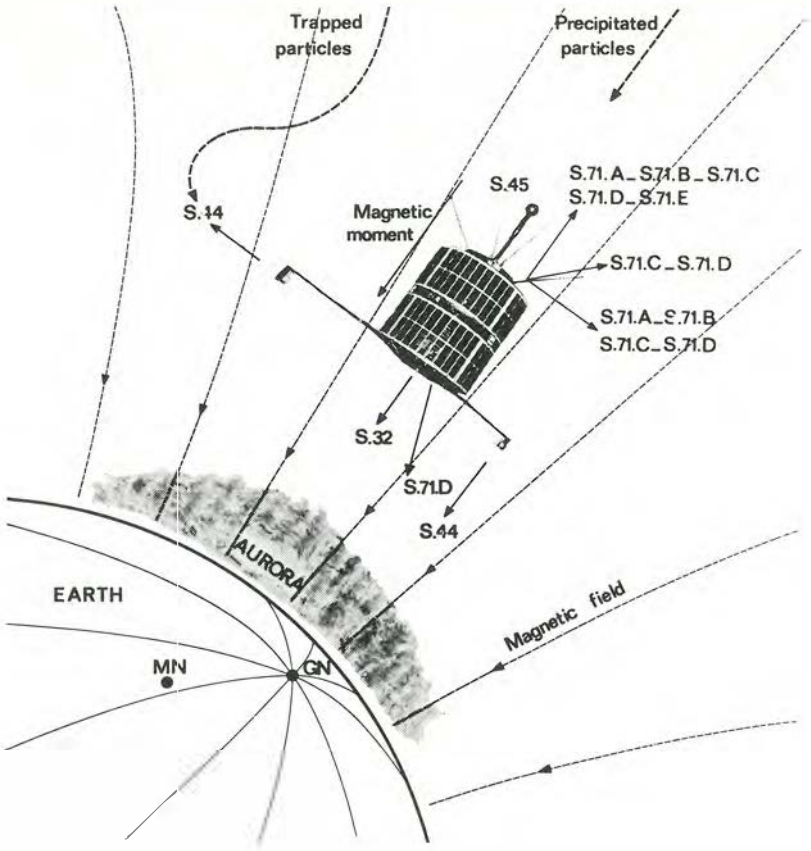

Figure 1. Orientation of ESRO-1 and its experiment sensors above the northern polar region.

Performance in orbit

ESRO-1A was launched on 3 October 1968 with an inclination of 90°, an initial apogee of 1500 km and a perigee of 275 km. It re-entered the atmosphere on 26 June 1970 after 20 months of highly successful operation despite the fact that it was designed for a nominal lifetime of only six months. ESRO-1B was launched on 1 October 1969 into a low orbit, which resulted in a lifetime of only 52 days.

Achievements

The auroral zone is one region of the Earth's environment which is most sensitive to changing solar conditions. The chain of events between a disturbance on the Sun and an auroral display was under intense investigation when ESRO-1A & B were in orbit, and the results they obtained not only confirmed the findings of NASA satellites, but improved on them since the energy ranges of the particles were more adequately covered than by previous satellites.

ESRO-1 also carried an experiment to measure energetic protons emitted during strong solar flares. These protons cause strong radio-wave absorption over the poles, resulting in the black-out of medium- and short-wave radio propagation.

The spatial resolution of the measurements of auroral features by onboard photometers was at the time superior to that from other satellites. Thus, the investigations performed concentrated on the accurate location of auroral structures and the determination of the causal particle precipitations. It was natural that those disturbances following large solar events had the highest priority, but the results of ESRO-1 were of paramount importance in defining conditions in the auroral zone during both quiet and disturbed periods.

Position of auroral zone and associated particle precipitation

Auroral hydrogen emission (H_β at 4861 Å) indicates the extent of proton precipitation because the excited hydrogen atoms are produced by the interaction of fast protons with atmospheric constituents. The nitrogen emission (N_2 at 4278 Å) indicates the total energy deposition and the total ionisation rate. One of the first results from ESRO-1A confirmed the rather meagre ground observations of the latitudinal shift of the auroral zone with variations in magnetic activity. As illustrated in Figure 2, the satellite intercepted the aurora equatorwards of 60° invariant latitude during orbit 225 and polewards of that latitude during the next two orbits. The planetary index of magnetic activity (K_p) was 4 during the first pass and fell to 2+ before the end of orbit 227. Thus the latitude of the peak intensity decreases as the magnetic index increases. A similar latitudinal variation was found in the precipitation of particles, and a cross-correlation analysis indicated that the particles responsible for the 4278 Å emission were electrons of energy in the region 5-15 keV.

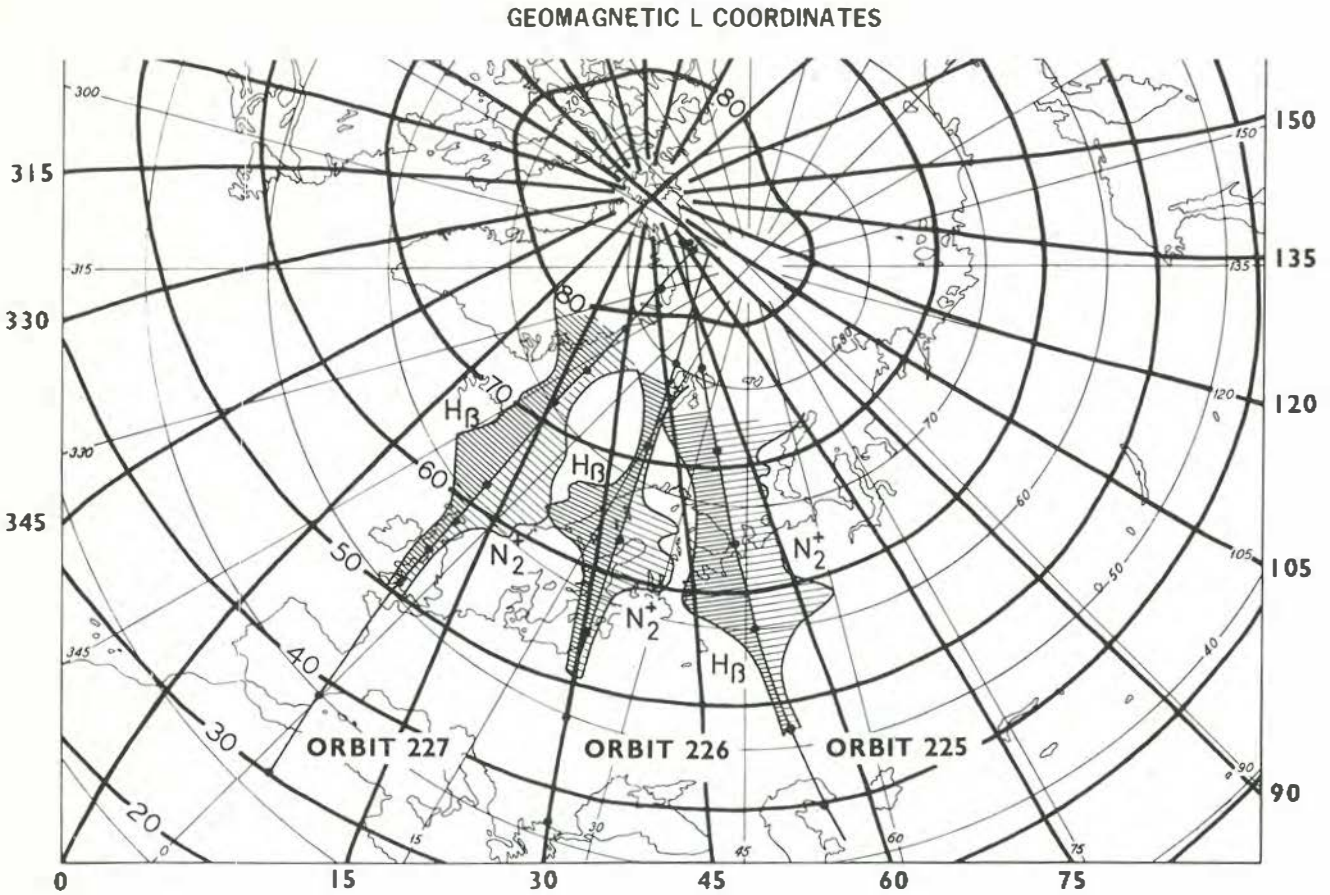

Figure 2. Experiment S32: Representative satellite passes over northern Europe showing the relative intensity of the H_β and N_2^+ emissions in geographic and invariant geomagnetic coordinates.

It is clear that the photometer measurements were only possible on the night side of the Earth. However it is of considerable interest to define the day-side auroral zone and this may be done by studying the particle data. The diurnal variation of the poleward boundary of trapped >40 keV electrons is shown in Figure 3 which is based on data from 3504 boundary crossings. In general, increased K_p raises the boundary latitude on the dawn side and lowers that on the dusk side. There are significant summer winter differences, the day-side boundary being highest at equinoxes.

Further details of the latitudinal characteristics of particle precipitation showed that the energy spectra for electrons and protons have discontinuities at the boundary of closed magnetic field lines; this is illustrated for electrons in Figure 4. The spectrum is seen to change rather smoothly with increasing latitude up to the boundary, while polewards of it the spectrum becomes distorted and consists mostly of low-energy particles. A similar change is observed for protons, and it can be concluded that on the midnight meridian the predominant morphological characteristics of the aurora on either side of the boundary of closed field lines are quite different.

The detailed morphological investigation of precipitating particles was not confined to the midnight meridian however, and a very extensive mapping for all local times and over a wide latitude range resulted in plots of the type shown in Figure 5, which is for protons in the 115-180 keV energy range, and for moderate magnetic activity. As is the case for electrons (Figure 3), the peak fluxes are positioned at higher latitudes on the day side than on the night side and it is found that as a result of increased magnetic activity, the precipitation zones become wider in latitudinal extent, the peak fluxes shift equatorwards and the proton precipitation extends gradually from the post-noon sector to the pre-noon sector.

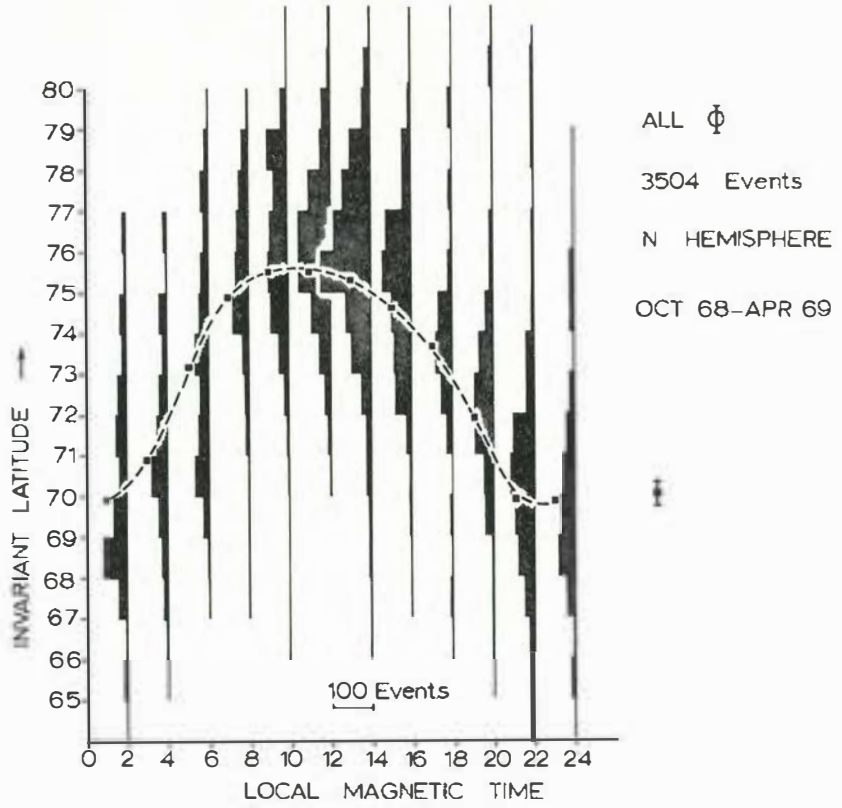

Figure 3. Diurnal variation of the poleward boundary of the radiation belt for 40 keV electrons.

Solar protons

Data obtained during solar proton events have been analysed by computing proton trajectories in a model magnetosphere. On the basis of these computations, the proton distribution at the magnetopause has been inferred from the proton distributions measured by ESRO-1 over the polar caps. This is important in determining the mode of entry of particles into the magnetosphere and a striking example is shown in Figure 6. The trajectory has a large eastward drift starting on the dawn side of the north polar cap, and undergoes two 'bounces' in each hemisphere before reaching the dawn sector of the magnetopause. A number of such events studied suggest that the protons reach the Earth by direct entry through the dawn-side magnetosphere and by entry through the magnetospheric tail.

Electron temperature and density

Besides providing temperature and density maps on a global scale, ESRO-1 enabled wave-like disturbances in these parameters to be

Figure 4. The observed electron intensity energy spectrum as a function of invariant latitude at one degree intervals for pass 266. Data marked '>40 keV' represent the integral intensity of all electrons above 40 keV.

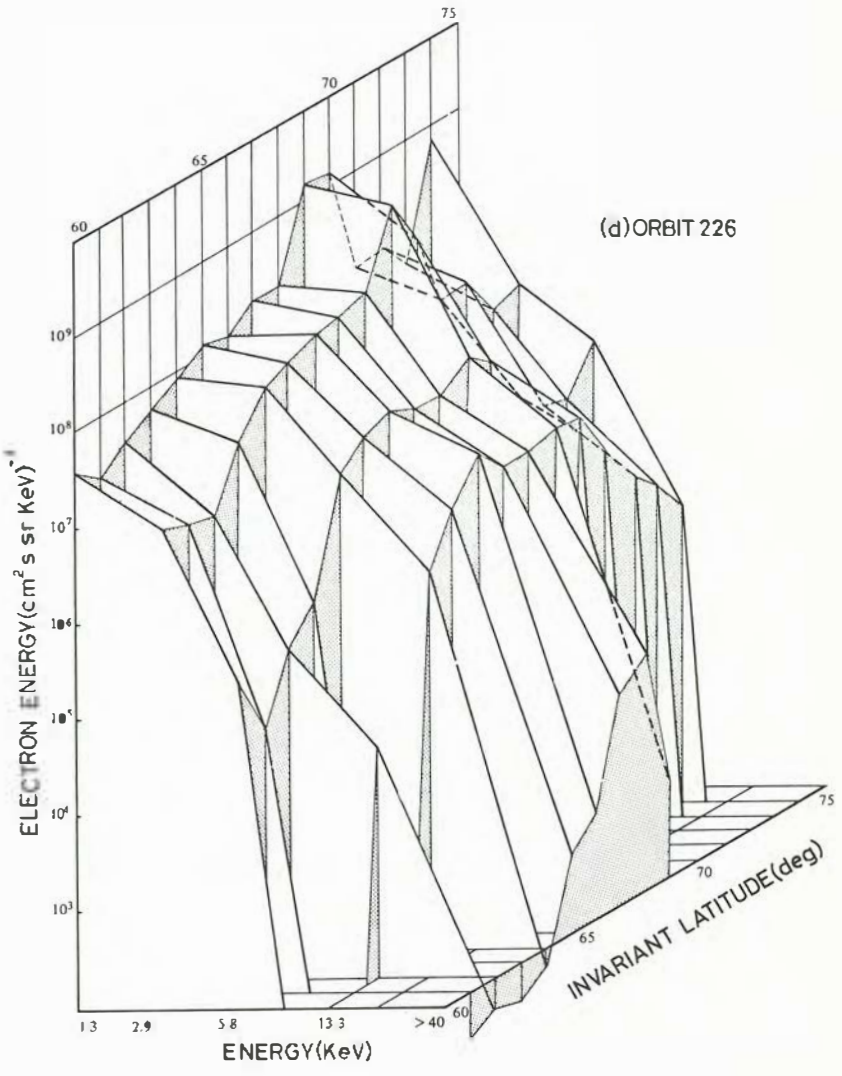

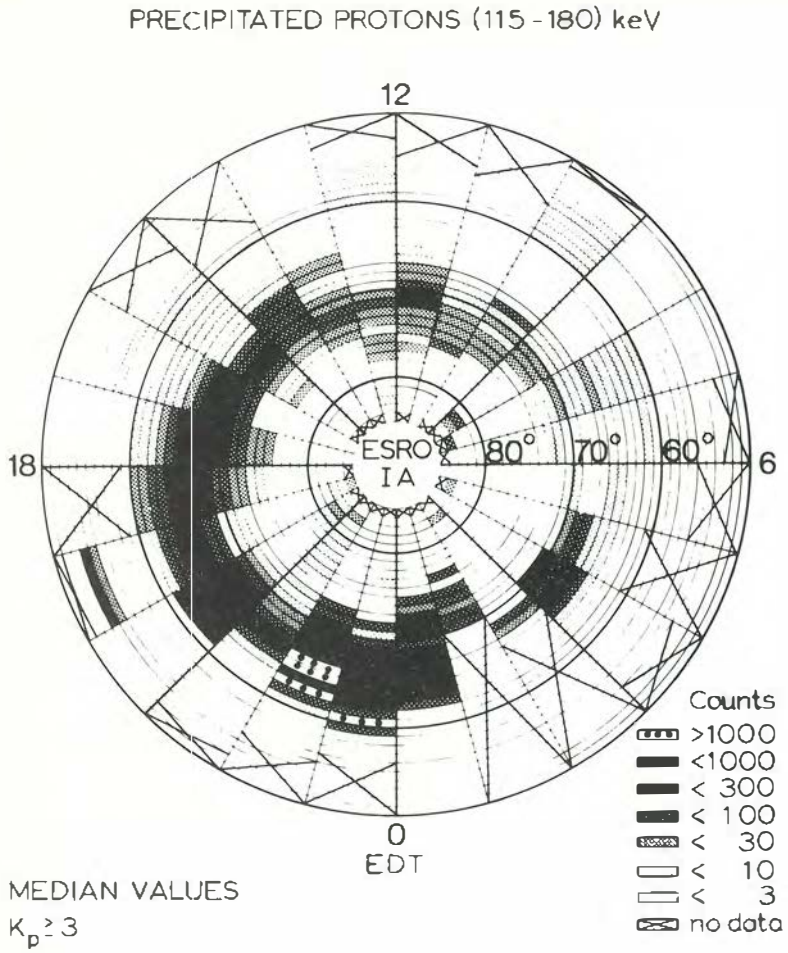

Figure 5. Meridian count values for 115-180 keV protons during disturbed conditions.

studied. It had earlier been suggested that atmospheric gravity waves could be expected to exist in the ionosphere as a result of the supersonic motion of the terminator at dawn or dusk. At the mesopause, the extent of the terminator's supersonic motion can extend to around 55° in latitude. Evidence for such disturbances was found in 120 orbits of ESRO-1 data, all of which occurred after the satellite entered the dawn sector. An example of the effect on the electron temperature is shown in Figure 7; the electron density showed a similar variation. Typical wavelengths for the data analysed were of the order of 1000 km and it is believed that they correspond to magnetohydrodynamic waves stimulated by gravity waves in the lower ionosphere. An additional feature in Figure 7 is the occurrence of sub-auroral temperature peaks, which are narrow bands of greatly enhanced temperature occurring at conjugate latitudes between 45° and 55° during times of magnetic disturbance.

Figure 6. Projections on the equatorial plane and the noon midnight meridian plane of a proton trajectory with appreciable longitudinal drift; the scales are in Earth radii. The initial invariant latitude and magnetic local time are 66.0° and 8.5 hr. respectively.

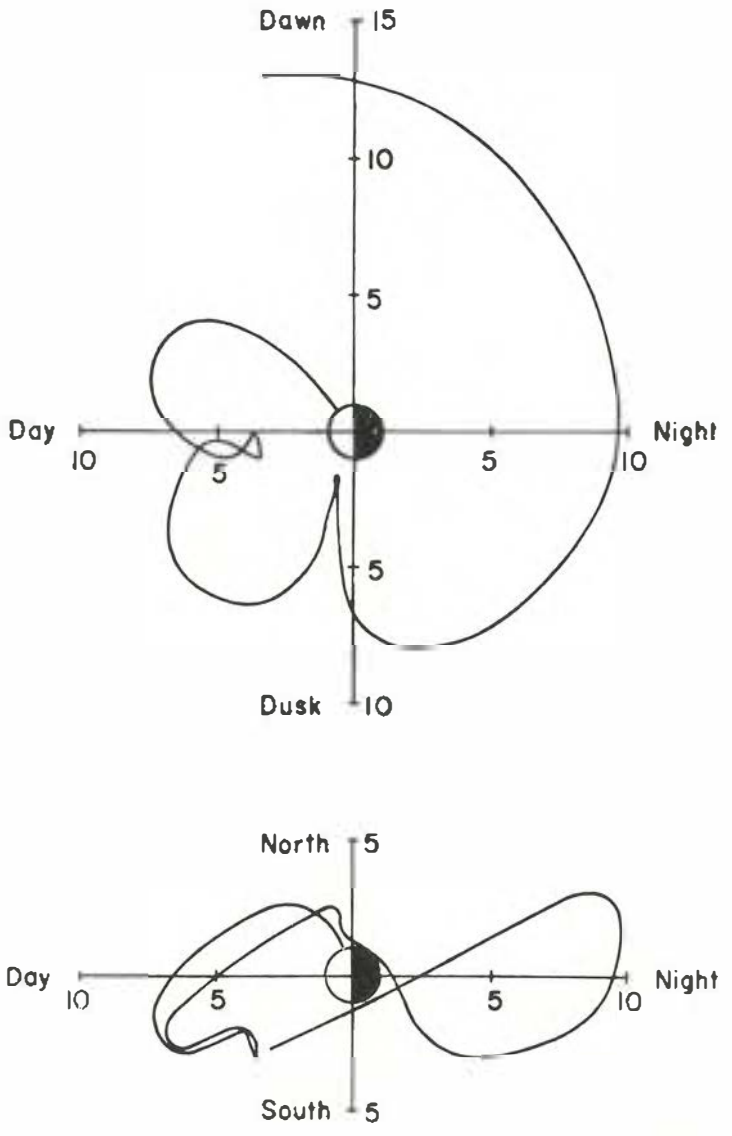

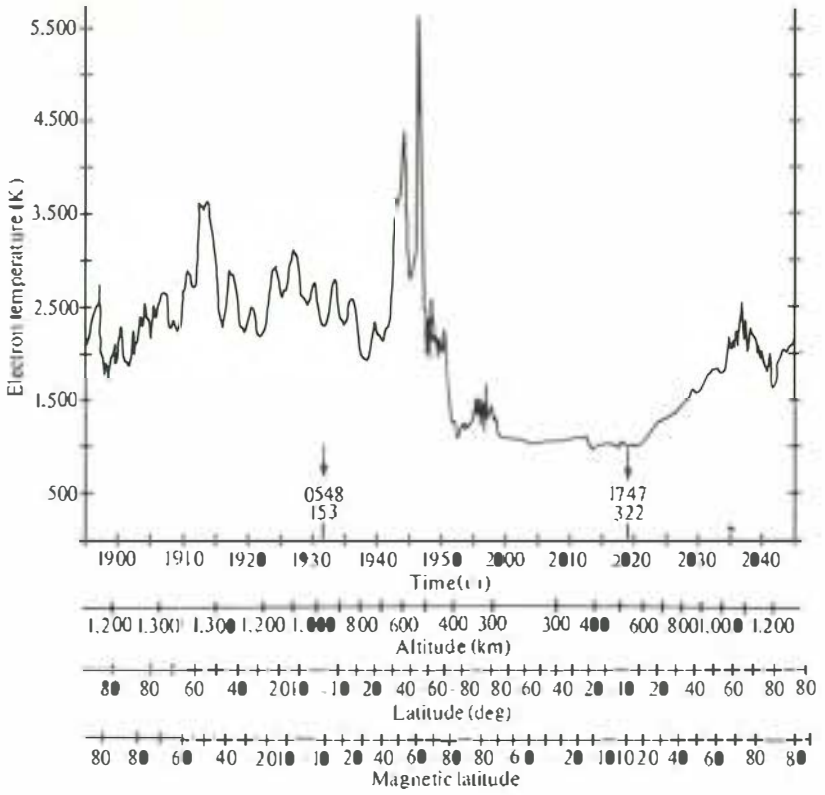

Figure 7. ESRO-1A electron temperature data. Orbit 2604. 5 April 1969. Arrows (→) mark LST of equator (top) and longitude of equator crossing (bottom).

Conclusion

It is clear from the few highlights selected how the results have added to the current knowledge of auroral and other processes. An extensive effort was made to correlate measurements from all the experiments on ESRO-1 for certain selected passes, and this led to considerable success in deciphering the complex signatures of auroral phenomena.

As one would expect, most results were derived from ESRO-1A, but considerable effort was also made to analyse data from ESRO-1B. Figure 8 shows an example of correlative measurements made simultaneously on the two satellites. Such measurements can be used to estimate the scale size of phenomena and to a certain extent, to separate space/time variations – a pioneering effort followed no less than ten years later by dual spacecraft missions into the solar wind.

Figure 8. Count rates of ESRO-1B and ESRO-1A over the northern polar cap on 3 November 1969. Note the in-phase changes although the spacecraft were separated by several hundred kilometers.

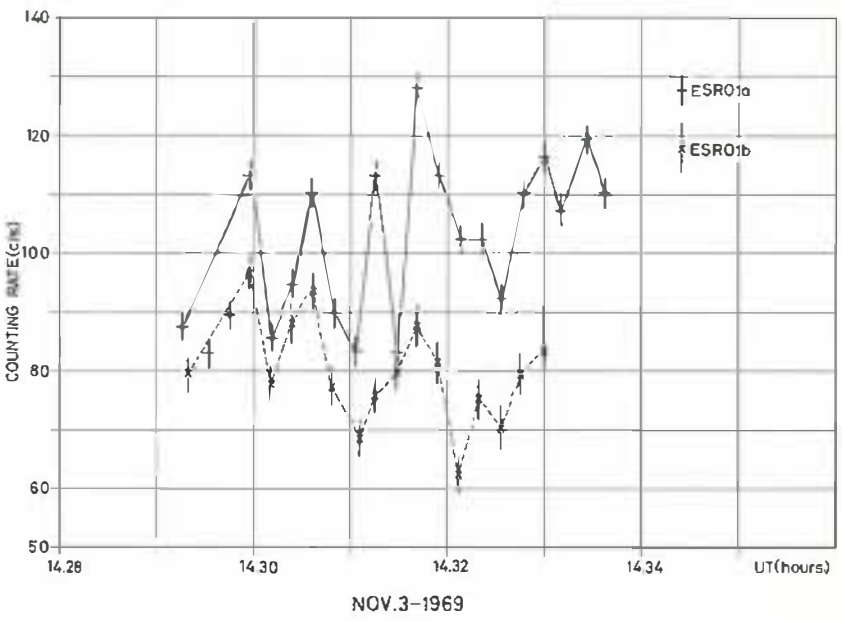

HEOS-1

Solar wind & magnetosphere

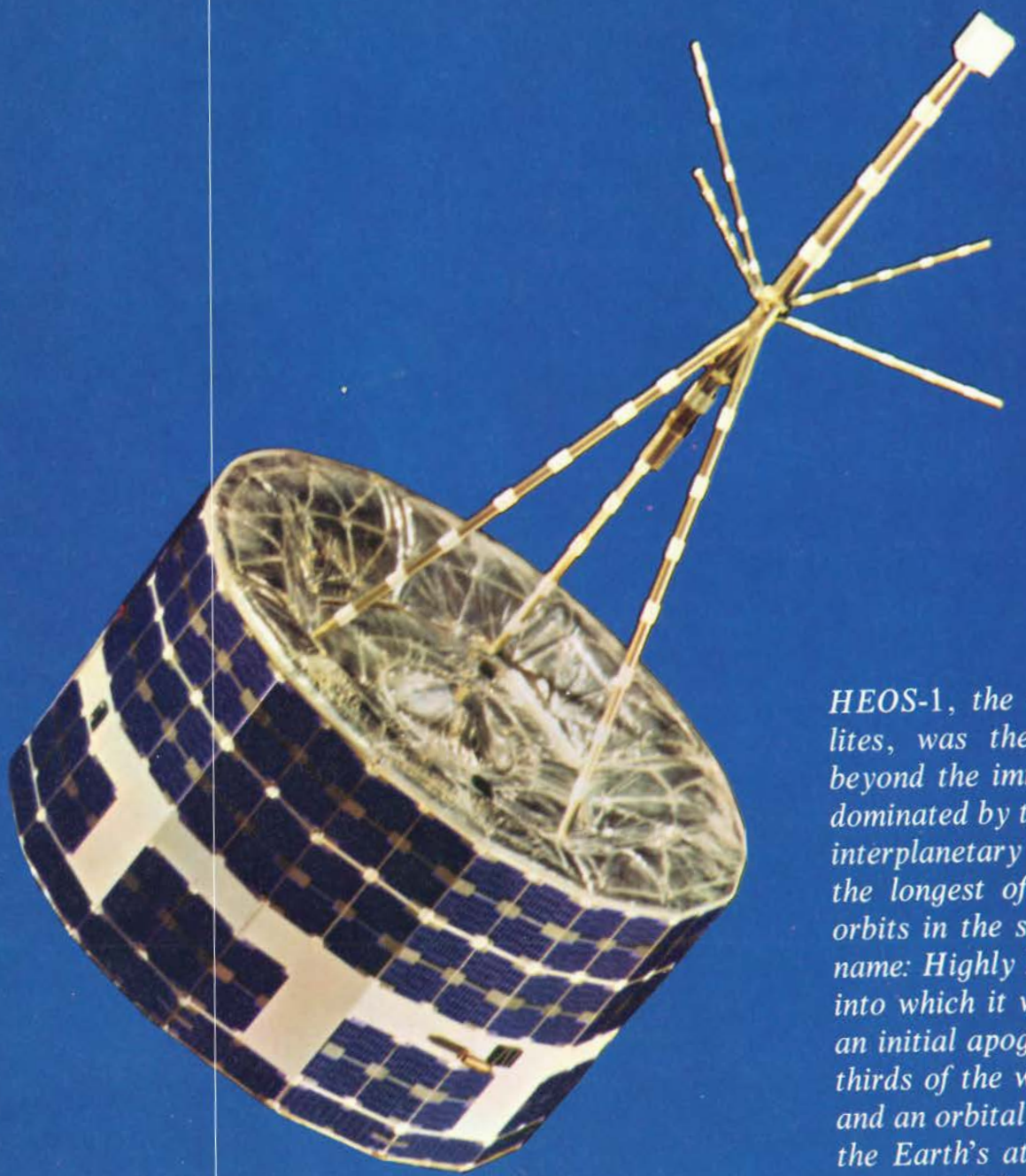

HEOS-1, the third of ESRO/ESA's scientific satellites, was the first European satellite to venture beyond the immediate vicinity of the Earth, which is dominated by the geomagnetic field, and to investigate interplanetary space. During its seven-year lifetime, the longest of any ESA satellite, it completed 542 orbits in the slender ellipse from which it derived its name: Highly Eccentric Orbiting Satellite. This orbit, into which it was launched on 5 December 1968, had an initial apogee of about 37 Earth radii (almost two-thirds of the way to the Moon), an inclination of 50° and an orbital period of four days. HEOS-1 re-entered the Earth's atmosphere on 18 October 1975 in operating condition.

Scientific mission

HEOS-1 made very significant contributions to our knowledge in two main areas. In the first place, it enabled us to gain a better understanding of the solar wind and the latter's variation during the course of the 11-year solar cycle. In the second, it shed much light on the solar wind's interaction with the Earth's magnetic field, particularly as regards the bow shock wave and its structure. The studies to which this information has contributed are of fundamental importance for our knowledge of the physics of collisionless shock waves.

Table 1. HEOS-1 experiments

Experiment	*Scientific Group*	*Objective*	*Measurement Technique*
S16	Max-Planck-Institute for Extraterrestrial Physics. Garching	To produce an artificial barium cloud in space and to observe how its expansion and motion are controlled by the physical environment at the release point	Release of barium cloud at 75000 km. Observe expansion and motion from a number of ground stations.
S24A	Imperial College. London	To measure interplanetary magnetic fields and investigate the fine structure at the shock front and magnetosphere boundary	Triaxial flux gate magnetometer. Range ±64 gammas. Accuracy better than 0.5 gamma.
S24B	Imperial College. London	To investigate the directional anisotropy of relativistic protons in relation to interplanetary magnetic fields	Two Cherenkov scintillator telescopes responding to protons >350 MeV. Geometric factors 5 cm^2 sr.
S24C	Imperial College. London	To measure the energy spectrum and arrival directions of solar protons and to correlate these with the magnetic field configuration	Two. four-element surface-barrier solid-state detector telescopes covering the proton energy range 1 to 13 MeV.
S58 73	Universities of Florence. Rome and Brussels	To measure the energy spectrum (S73) and angular distribution (S58) of the positive component of the solar wind	Hemispherical electrostatic deflector with Faraday cup collector. Measured protons from 0.15 to 15 keV.
S72	Centre d'Etudes Nucléaires. Saclay	To measure the flux and spectra of electrons. protons and alphas of solar and galactic origin	Four-element solid-state detector telescope. Measured protons from 3.8 MeV to relativistic energies.
S79	Centre d'Etudes Nucléaires Saclay and University of Milan	To measure the flux and energy spectrum of the primary electron component of cosmic radiation	Four-element telescope including gas Cherenkov counter and lead-glass Cherenkov absorber.

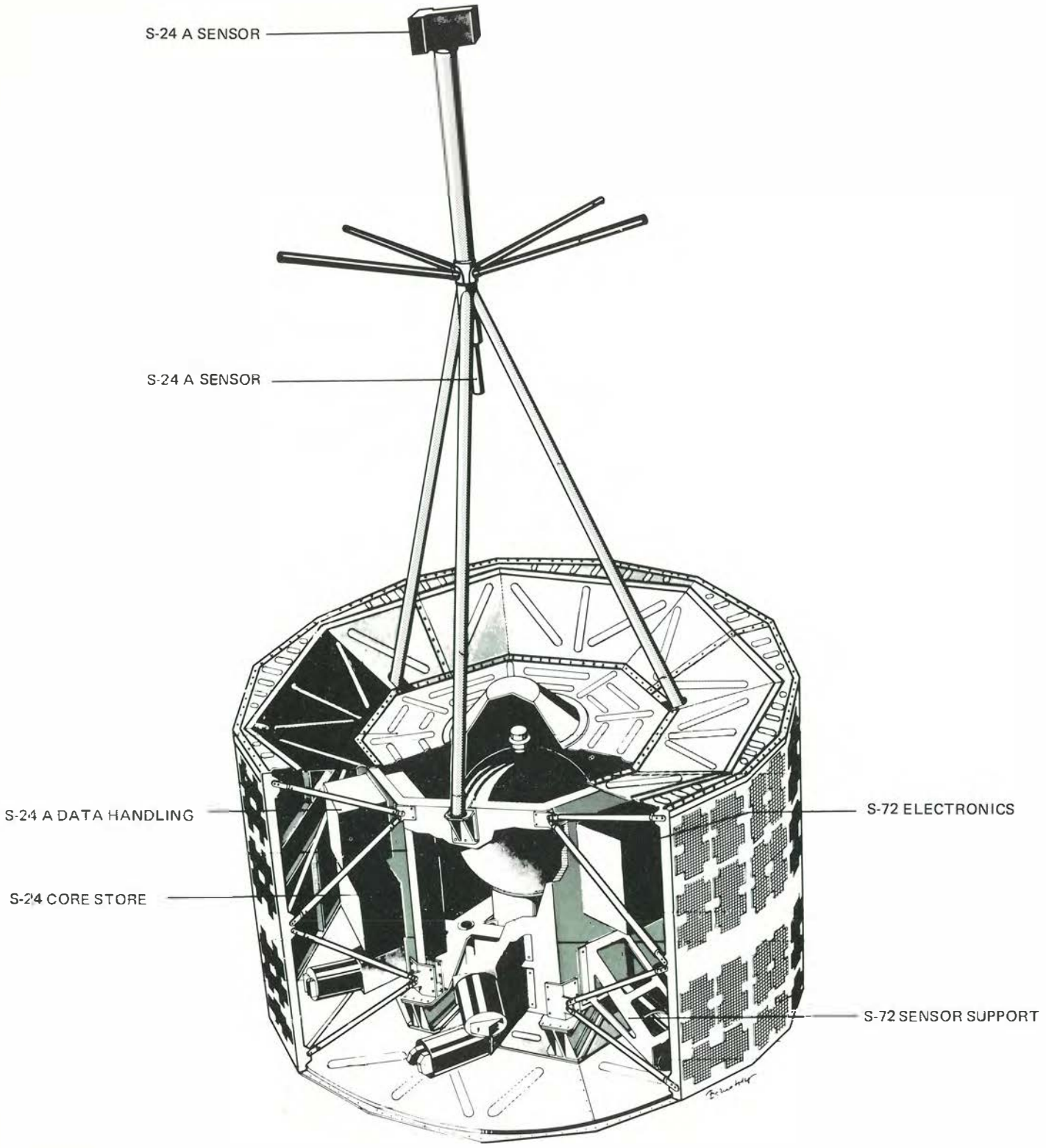
S-24 A SENSOR
S-24 A SENSOR
S-24 A DATA HANDLING
S-24 CORE STORE
S-72 ELECTRONICS
S-72 SENSOR SUPPORT

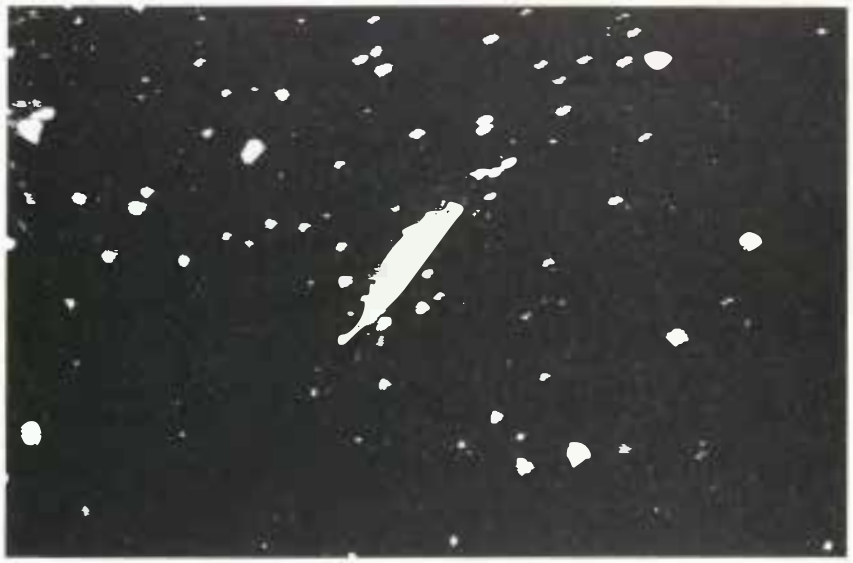

Figure 1. Artificial ion cloud experiment ejected from HEOS-1 in the outer magnetosphere on 18 March 1969. The length of the cloud is about 3000 km.

Spacecraft and payload

Designed for a field and particle mission, HEOS-1 was spin stabilised (10 rpm). A technological 'first' to which it could lay claim was the use of a cold-gas spin-axis re-orientation system that enabled instruments viewing out of the equatorial plane of the satellite to perform anisotropy measurements in which scanning took place either in a plane parallel to the ecliptic plane or in one perpendicular to it. Many re-orientation manoeuvres were successfully performed for the purpose of switching scanning planes or sensor intercalibration.

For more than 95% of the orbital period, the satellite was in sight of a tracking station. This made it possible to dispense with a tape recorder and to transmit all data in real time. A drawback, however, was the very low data rate of 12 bits per second.

The eight experiments (Table 1) chosen to fulfil the aims of the mission covered a wide range of interrelated physical parameters. This payload gave excellent scientific data for about 16 months, exceeding the design lifetime by four months. Subsequently, a gradual failure in the satellite's attitude measurement system seriously affected its operation. The magnetic-field experiment continued to work until re-entry, thus providing an unprecedented record of the interplanetary magnetic field for almost seven of the solar cycle's eleven years.

Two novel features of the payload deserve mention. One was equipment that made it possible to release an artificial barium cloud in the distant magnetosphere; the other was a reprogrammable event-detecting memory system in the magnetometer experiment used for the first time for recording fast transient events far from the Earth.

Achievements

Seven years of observations in orbit have (in spite of the low data rate) yielded a rich harvest, which bears comparison with that of American satellites. A particularly rewarding aspect of this output has been the large number (90) and high quality of the publications that have been produced mostly as a result of collaboration among the various groups of experimenters. Valuable results have also been obtained from the correlation of HEOS-1 data with those of other ESRO/ESA, European, American and Russian satellites. In general, the HEOS (1 and 2) programmes have demonstrated that co-operation both between scientists with experiments on the same satellite and between experimenters served by different satellites is the best way of making really effective use of the available data.

Magnetosphere and bow shock

One of the first and most spectacular results was the demonstration of the properties of the plasma in the outer magnetosphere by the

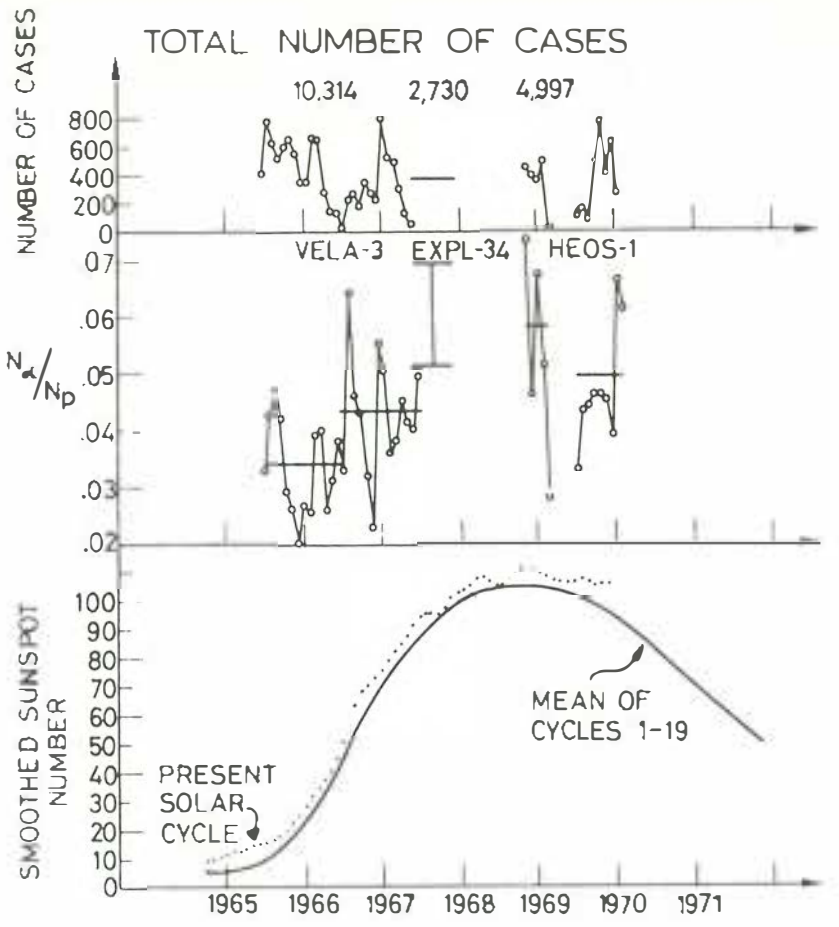

Figure 2. Time history of the helium-to proton density ratio in the solar wind over part of a solar cycle.

release of a barium cloud at a distance of 75 000 km from the Earth. (This can be considered as a forerunner of the so-called 'active' experiments performed with recent satellites and planned for Spacelab.)

Much of the progress in understanding observations of the structure of the terrestrial bow shock has come from the efforts of the HEOS-1 plasma experimenters. HEOS-1 observed, for the first time, the bow shock as much as 14 Earth radii outside its usual location. Such observations, and the excellent co-operation between the plasma and the magnetic-field experimenters, led to the first quantitative study of different shock structures in space, characterised by the downstream plasma state. Shock encounters were ordered by the Mach number, the beta of the solar wind (the ratio of plasma to magnetic pressure) and the angle between the magnetic field direction and the shock normal, identified as parameters being most important for the understanding of the observations. The results clarified greatly the previous confusion on the Earth's collisionless bow shock structure: the high variability of the important parameters explained why the detailed shock observations always looked different from one another. It has also become clear that the many different theories developed for different plasma regimes may be useful, since different dissipation mechanisms are present in different plasma regimes.

These results, a major step forward in the physics of collisionless shock waves, were the premise for a cooperative effort between HEOS-1 and OGO-5 experimenters who took advantage of the HEOS-1 solar-wind data to select periods with different values for the important upstream plasma parameters for which OGO-5 had detailed (high time resolution) observations of the bow-shock

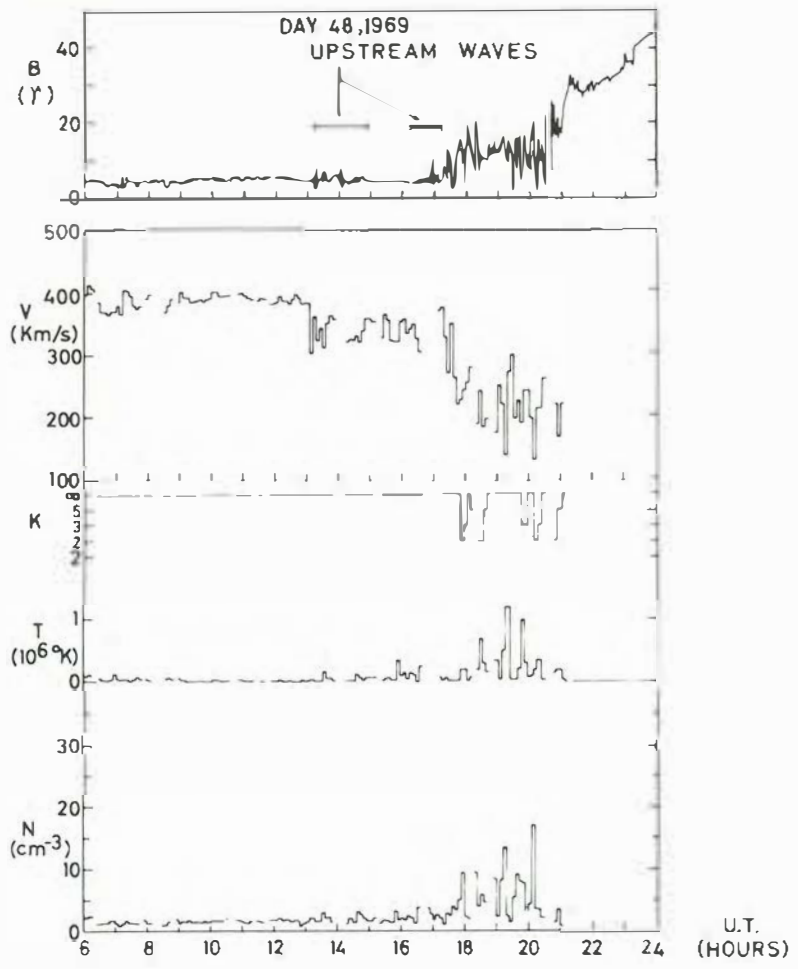

Figure 3. HEOS-1 inbound magnetosheath crossing with periods where upstream waves are observed in the interplanetary medium.

structure. In this way a 'catalogue' of shock structures was made, and each structure was then studied in detail.

The magnetospheric field data have also proved very valuable. The combined HEOS data taken inside the various regions of the magnetosphere have been used to refine and improve existing magnetospheric models.

The charged-particle detectors were able to make direct measurements in interplanetary space of the intensity and arrival directions of the particles produced by a solar flare. The HEOS-1 experimenters then joined forces with the ESRO-1 and ESRO-2 workers (whose satellites were in near-Earth orbits at the same time) in providing an explanation for the manner in which these solar particles enter the magnetosphere and make their way down to the polar-cap regions of the Earth.

Solar wind

The long life of HEOS-1 was ideally suited to a study of the long-term behaviour of various interplanetary parameters. The solar wind detector, in conjunction with previous American measurements, made it possible – for the first time – to establish long-term changes in the density of the solar-wind plasma over the solar cycle. It was found that the density ratio of alpha particles and protons increased with the sun-spot number and that this was due to a decrease in the proton density at solar maximum and a simultaneous increase in He-rich solar wind streams. No significant variation of the solar wind velocity was found, however. The magnetic field data obtained concurrently from HEOS-1 and HEOS-2, revealed a solar-cycle change in the level of low-frequency turbulence in the interplanetary medium. The mean interplanetary field strength, however, was found to be largely independent of the level of the solar cycle.

Important results have been obtained on the alpha-particle component of the solar wind. Previous studies had not paid attention to the fact that occasionally the bulk speeds of protons and alpha particles were substantially different. The energy resolution of the HEOS plasma detector made it possible to separate the alpha particles from the much more abundant protons. It was shown that, within the limits allowed by plasma instabilities (two-beam instability and generalised firehose instability), the two solar wind components behaved almost independently. It was also demonstrated that some coupling between protons and alpha particles should have been present because of the temperature increase observed when the two species had different bulk speeds. Later, American experimenters confirmed these results and found that larger differences between the two bulk speeds were found at the trailing edges of high-speed streams.

Cosmic-ray observations over the past three decades have shown that there is a marked variation in intensity near the Earth over the solar cycle. This variation had been interpreted in terms of changes in the interplanetary field structure and solar wind over the sunspot cycle. Nevertheless, the interplanetary observations to which HEOS-1 contributed so significantly are incapable of accounting for the observed change in cosmic-ray intensity. Cosmic-ray modulation therefore remains something of a puzzle. It is now seriously doubted whether the measurements of the interplanetary magnetic field and the solar wind, which have all been made near the plane of the ecliptic, are representative of interplanetary space in general. To solve the puzzle one needs to investigate how the interplanetary structure changes with heliographic latitude. The puzzle left unanswered by HEOS is a challenge for the International Solar Polar Mission under development as a joint ESA/NASA programme.

The HEOS-1 magnetic-field data, in combination with measurements made concurrently in HEOS-2, have provided a unique record of the structure of the near-Earth interplanetary magnetic field. These data have now been made available to a worldwide scientific community and are frequently used for correlation with data from the ground, balloons, rockets or other satellites. The measured sector structure (the interplanetary field is directed towards the Earth for some days, then reverses and is directed towards the Sun for another few days) confirmed the recently developed method of predicting this polarity on a day-to-day basis from ground-based data.

The main motivation for studies of solar proton events was to better understand the mechanism responsible for particle acceleration, the transport of the particles in the complicated magnetic field structure prevailing around active regions of the Sun and the propagation of these particles in the interplanetary medium. Several high-energy electron increases have been measured by HEOS-1 around solar maximum. The detailed analysis of these events demonstrated the great importance of coronal storage and coronal propagation, compared to the diffusion in interplanetary space.

HEOS-2

Polar magnetosphere & interplanetary medium

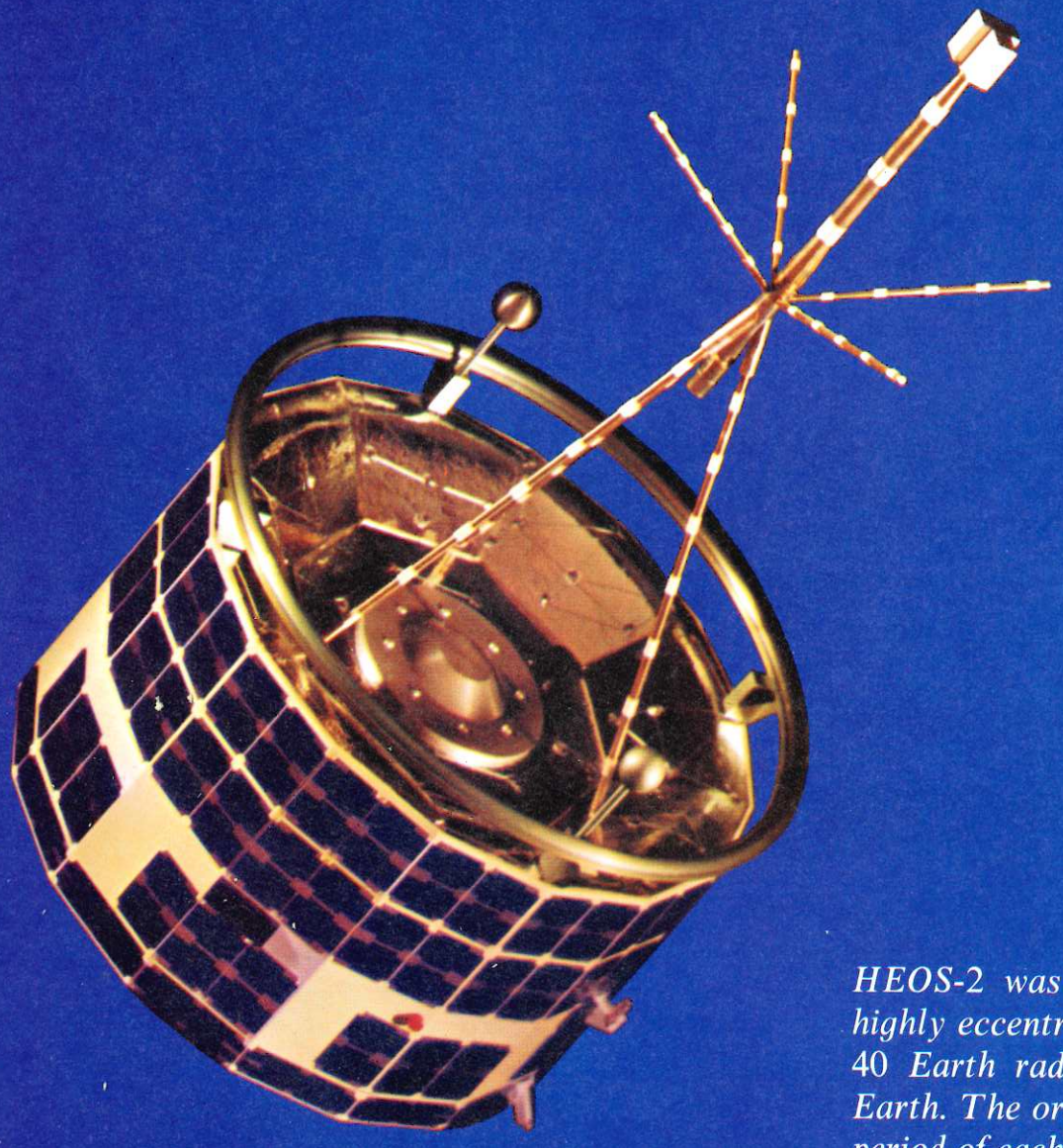

HEOS-2 was launched on 31 January 1972 into a highly eccentric polar orbit, with an apogee at about 40 Earth radii nearly above the north pole of the Earth. The orbital period was 5.2 days. Thus a major period of each orbit was spent in interplanetary space. HEOS-2 re-entered the Earth's atmosphere on 2 August 1974 after completing 176 orbits.

Scientific mission

The HEOS-2 mission combined two important scientific objectives. A unique orbit – the first truly polar highly-eccentric high-apogee orbit – enabled the spacecraft to venture into a region of the Earth's environment previously unexplored: the distant polar magnetosphere and its boundaries. It had often been suggested that this region might hold the key to many unanswered questions of magnetospheric research; e.g. how do solar wind particles enter the magnetosphere? It had also been the subject of theoretical speculation; in particular, it had been predicted that there was a 'neutral point' on the magnetopause (the boundary of the magnetosphere) in each hemisphere, where the field lines diverge and the field strength becomes very small.

The high apogee of the HEOS-2 orbit was selected to fulfil the second scientific objective, the study of the interplanetary medium. Here it was to observe the magnetic field, the solar-wind plasma, solar particles, cosmic rays and micrometeoroids.

Spacecraft and experiments

The HEOS-2 spacecraft was technically based on the concept of its predecessor, HEOS-1. Carrying essentially a field and particle payload, HEOS-2 was spin-stabilised at 10 rpm. The spin-axis re-orientation system allowed experiments to look in different directions or to search for anisotropies and flow directions when combining observations made with different spacecraft attitudes. The bit rate had been increased to 32 bps. The spacecraft and its subsystems performed almost faultlessly throughout its orbital life.

HEOS-2 carried seven experiments chosen to fulfil the aims of the mission (Table I). The payload consisted of a magnetometer, two plasma experiments, an energetic-particle experiment, a high-energy cosmic-ray electron detector, a ULF plasma-wave experiment and a cosmic-dust detector. All instruments were still operating at the end of the mission.

Table 1. *HE●S-2 experiments*

Experiment	*Scientific Group*	*Objective*	*Measurement range*
S201	Imperial College, London	Magnetic field measurement in magnetosphere and interplanetary space	0 - ± 144 gamma
S202	Laboratorio Plasma Spazio (LPS), CNR, Frascati	Measurement of electrons and protons inside and outside the magnetosphere	10 eV - 40 keV (per unit charge)
S203	Danish Space Research Institute, Copenhagen	Measurement of ELF radiation in solar wind and magnetosphere	20 - 236 Hz
S204	Space Science Dept., ESA, Noordwijk	Measurement of electrons, protons and alpha particles inside and outside magnetosphere	Electrons: 0.04-3 MeV Protons: 1-36 MeV Alphas: 36-142 MeV
S209	University of Milan, Centre d'Etudes Nucléaires, Saclay	Measurements of high-energy primary electrons	10 - 600 MeV
S210	Max-Planck-Institut, Garching	Measurement of solar wind	230 eV - 16 keV (per unit charge)
		Measurement of low-energy electrons and protons in magnetosphere	100 eV - 40 keV (per unit charge)
S215	Max-Planck-Institut, Heidelberg	Measurement of micrometeoroids	$10^{-17} - 10^{-9}$ g

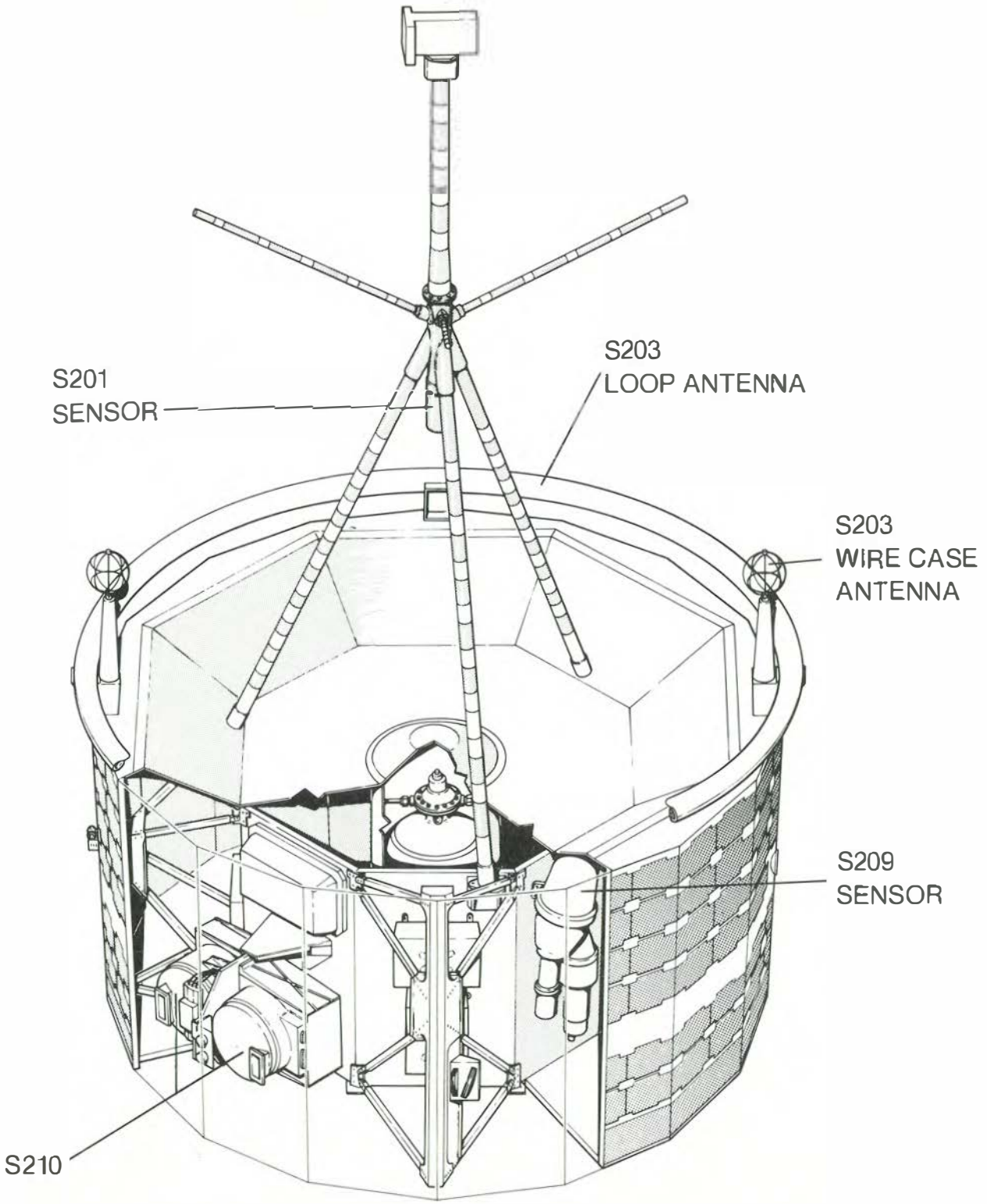
S201
SENSOR
S203
LOOP ANTENNA
S203
WIRE CASE
ANTENNA
S209
SENSOR
S210

Achievements

The list of HEOS-2's scientific achievements is long. This report highlights some of them; it does not present a complete summary of the complex and highly variable phenomena observed by the satellite in the polar magnetosphere and the interplanetary medium.

A particularly gratifying aspect of the HEOS programme has been the excellent cooperation between the experimenters. Many of the exciting new results could only be obtained by coordination of data obtained by various instruments. The willingness of most experimenters to make their data available when requested has been greatly appreciated. The HEOS magnetometer experimenter merits special mention in this context.

The polar magnetosphere

Where and by which process does the solar-wind plasma enter the magnetosphere? Does the magnetic field topology in the distant polar cusp – the region where the closed magnetic field lines on the dayside separate from the field lines of the polar magnetotail – resemble that of a closed or an open magnetosphere? These, and similar questions, have been of major interest to magnetospheric research for a long time. The HEOS-2 mission with its unique orbit was designed to provide answers to such questions – and it did. HEOS-2 provided the first systematic description of plasmas and of the magnetic-field topology in the distant polar magnetosphere. It discovered regions and phenomena previously unsuspected and not predicted by theories. Some of these HEOS-2 discoveries in the polar magnetosphere now form part of any basic description of the magnetosphere and are fundamental for our understanding of magnetospheric processes.

The plasma observations have revealed the presence of a nearly persistent layer of plasma inside and adjacent to the magnetopause with a distinct flow at velocities around 100 km/s in a direction down the magnetotail away from the Earth. This layer has been called the 'plasma mantle' because of the way it covers the outer regions of the magnetotail. It can extend into the tail for several Earth radii from the magnetopause, and its thickness varies with conditions in interplanetary space.

The source for most of the plasma in the plasma mantle lies on the sunlit side of the magnetosphere. Here HEOS-2 discovered a

Figure 1. HEOS-2 orbit in relation to near-Earth environment. Note the 'plasma mantle' along the magnetotail boundary and the 'entry layer' in the high-latitude dayside magnetosphere that were discovered by HEOS-2.

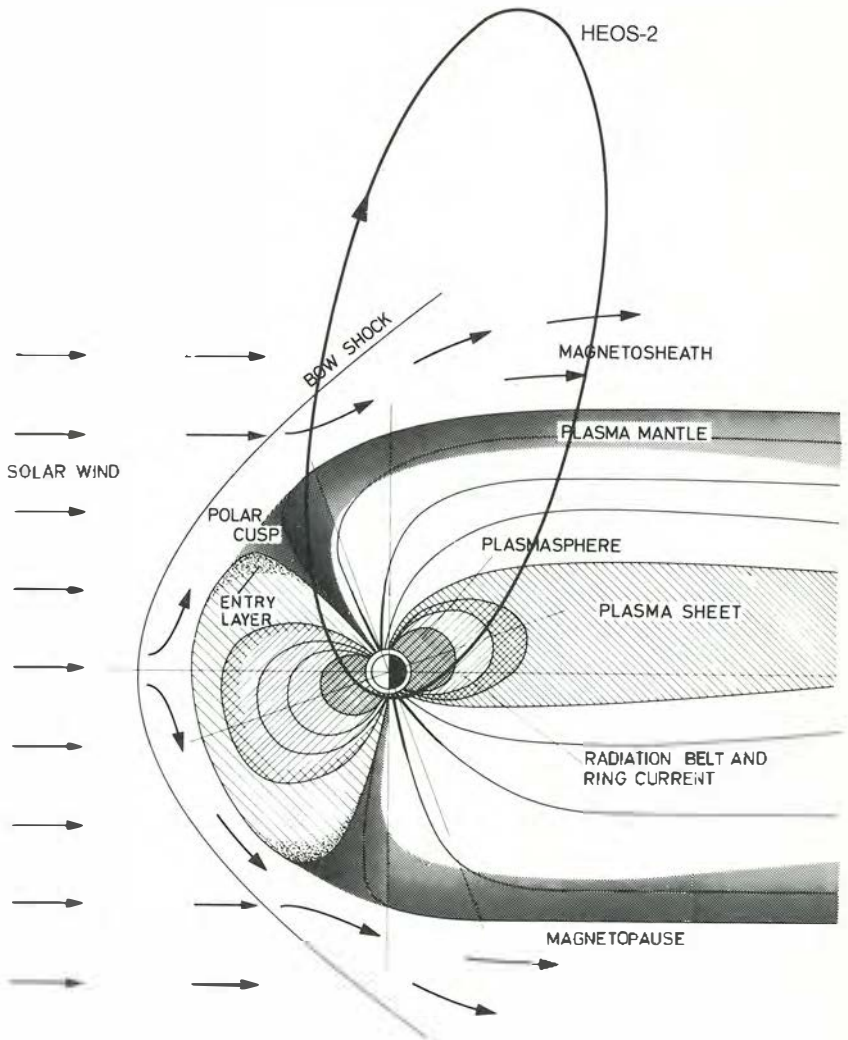

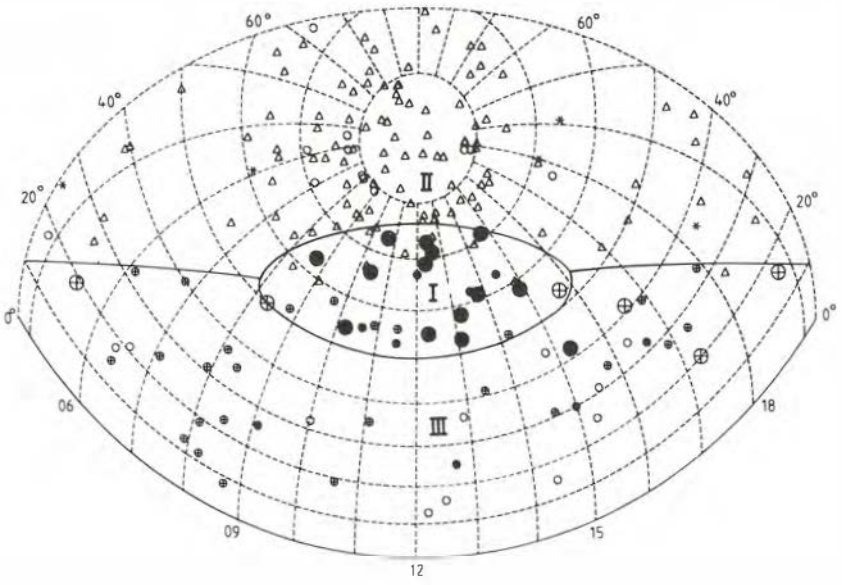

Figure 2. View of a section of a model magnetopause with the HEOS-2 locations of the plasma boundary layer inside the magnetopause in solar magnetic (SM) co-ordinates. For the various symbols refer to the text. The heavy solid lines delineate the 3 distinct plasma regions found: the entry layer proper (region I), the plasma mantle (region II) and the low-latitude boundary layer (region III) of small thickness and low density (S210).

boundary layer of magnetosheath-like plasma inside the dayside magnetopause which exists preferentially at high latitudes, around the distant polar cusp region. It does not show the regular flow of the plasma mantle, but highly variable velocities and directions. This region is seen to be the 'port of entry' of solar-wind plasma into the magnetosphere and has been termed the 'entry layer'. Particles which enter here and then flow down the cusp field lines towards the Earth are mirrored before reaching the ionosphere and flow back out again. In the presence of a polar-cap electric field, however, the magnetic field and the plasma are convected towards the polar caps, and the out-flowing plasma is then contained within the tail magnetopause. This theory implies that a stronger electric field convection will carry the plasma deeper into the polar cap and will produce a thicker plasma mantle.

The entry layer does not continue smoothly to lower latitudes. Here HEOS-2 has found only a very thin boundary layer, therefore strongly supporting the idea that entry of solar-wind plasma occurs mainly at high latitudes. Another important result is that – in contrast to the plasma mantle – the dayside magnetopause plasma layers seem to lack any simple correlation with the orientation of the external interplanetary magnetic field.

These results have a strong implication for the hitherto generally accepted concept of merging of geomagnetic and interplanetary fields. For if, as was generally assumed, the merging process was taking place mainly around the nose of the magnetosphere, one would expect to observe a fast directed flow along the magnetopause surface from low to high latitudes. Such a flow has not been seen in the HEOS data, however. It is concluded, therefore, that the merging process occurs predominantly in the polar cusp region as a consequence of the very turbulent plasma flow.

One of the interesting questions asked prior to the launch of HEOS-2 was: Is there a neutral point at the high-latitude magnetopause as predicted by models separating the closed field lines of the dayside magnetosphere from the open field lines of the magnetotail? Magnetic field and plasma data obtained from the potential neutral point region have been carefully analysed but no definite answer has been found. On several orbits, HEOS-2 encountered deep minima in the magnetic field intensity near the magnetopause, but their exact location did not coincide with the boundary, and the minima can easily be explained by other physical effects. One can therefore conclude that the experimenters have not found in their data the clear signature of a neutral point, i.e. a transit from a radial field orientation inside to a tangential

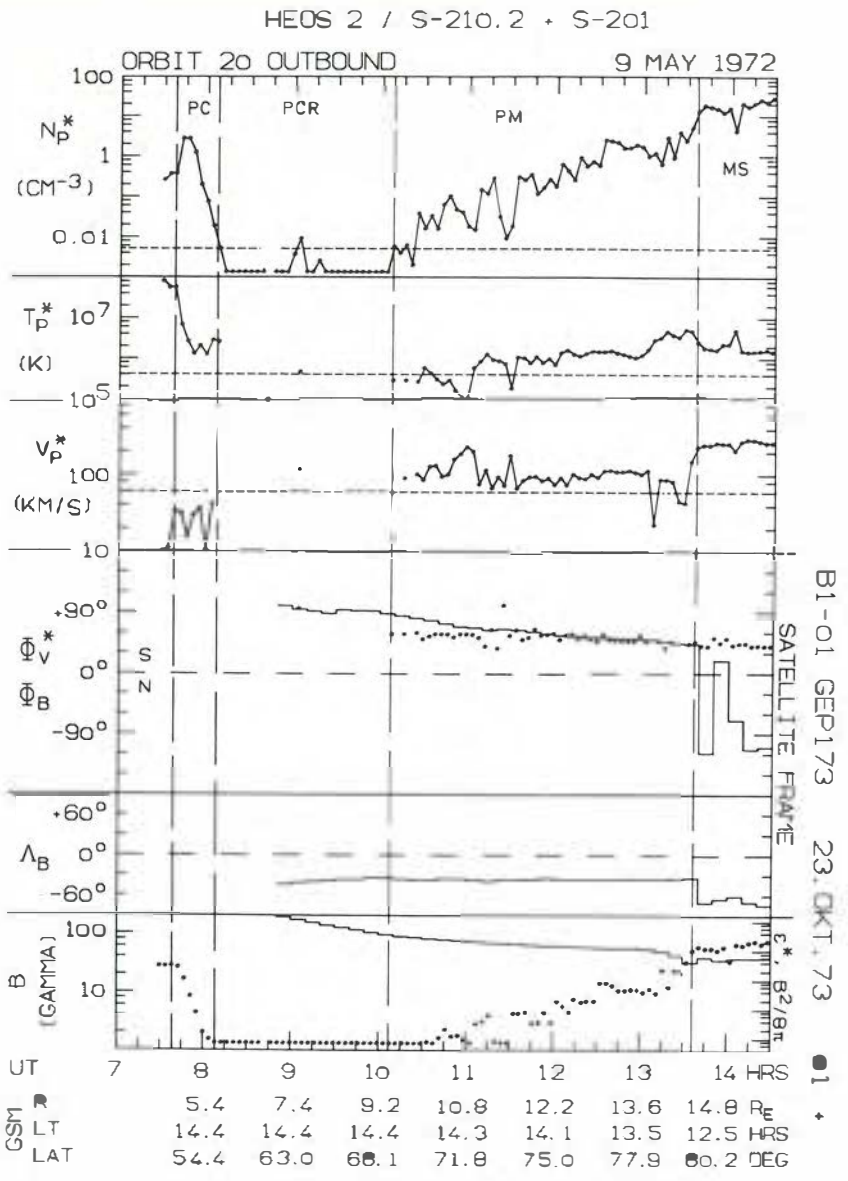

Figure 3. Plasma parameters and magnetic field as a function of time during polar magnetosphere traversal on outbound orbit 20. Satellite position in geocentric solar magnetospheric (GSM) co-ordinates is indicated at the bottom (S210 S201).

direction outside of the magnetosphere, accompanied by a strong depression of the field strength in the region where the neutral point had been expected. A marked difference of the shape of the magnetospheric boundary, attributed to the polar cusp region, has, however, been definitely found by HEOS-2. The magnetopause in this region shows a clear 'indentation', i.e. a deviation from a spheroidal magnetospheric surface, having the shape of a funnel and not that of a line.

Another unexpected HEOS-2 discovery is the existence of a layer of energetic electrons extending from the polar cusp region along the magnetosheath side of the tail magnetospheric boundary. This layer being a few Earth radii thick is always present and becomes very intense when geomagnetic activity is high. The problem of its origin is unsolved. So far, it has not been established whether the electrons have escaped from the Van Allen belts on the dayside or whether they are being accelerated somewhere near the magnetopause, possibly in the exterior polar-cusp region. The three-dimensional spatial distribution of these electrons in the outer magnetosphere and magnetosheath recently derived from HEOS observations strongly supports the latter hypothesis. Also, strong low-frequency plasma-wave activity observed in the exterior cusp region can be taken as an indication for processes taking place in this region that involve wave/particle interactions.

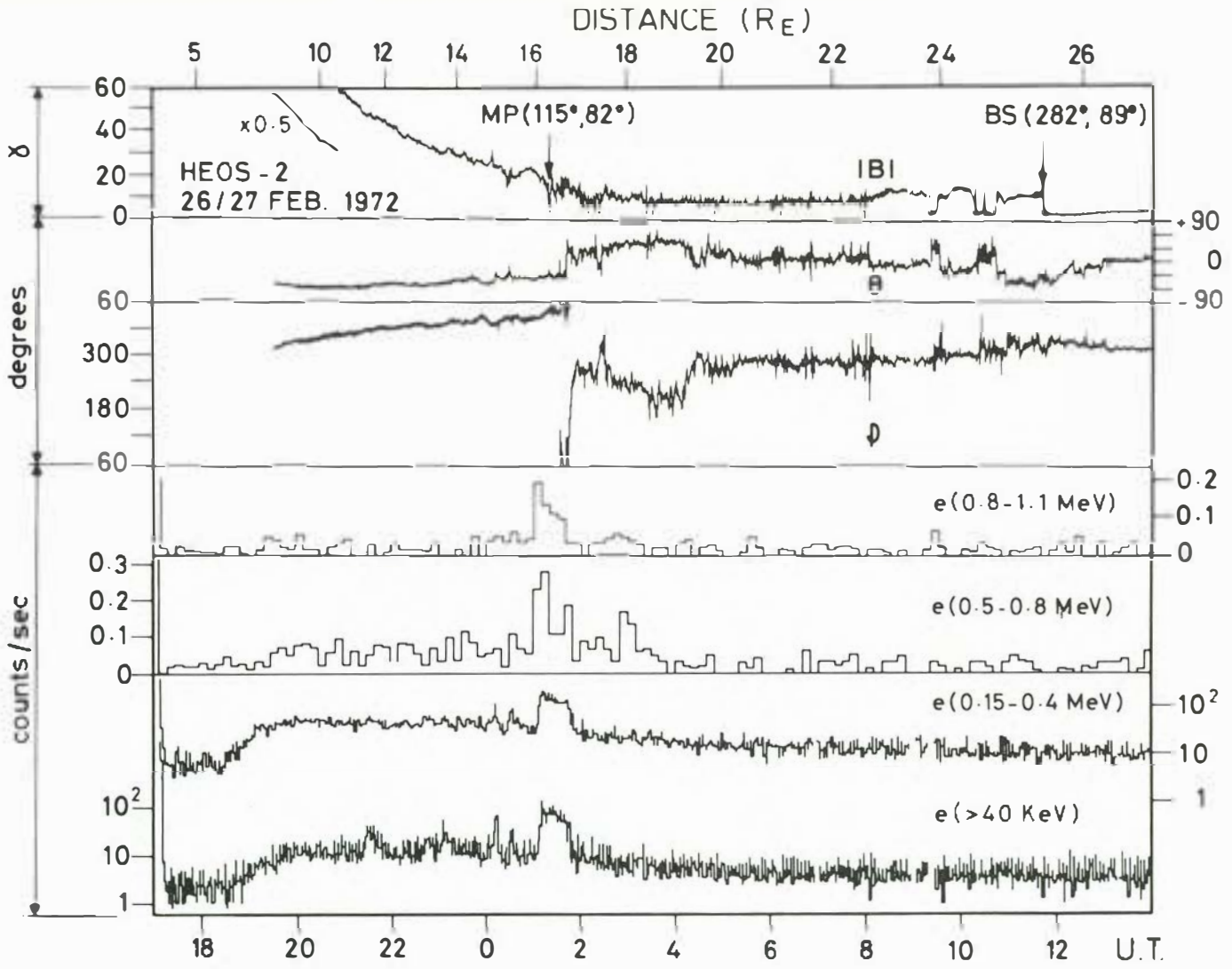

Figure 4. Magnetic field (S201) and energetic electrons (S204) ●bserved during ●utbound magnetosheath crossing.

Information on the structure of the magnetospheric boundary and its interaction with the interplanetary magnetic field can be inferred from the study of solar particles penetrating into the magnetospheric cavity. The HEOS-2 orbit offered a good opportunity to study, in situ, these particles entering into the high-latitude magnetotail lobes. The observations of several 'events' indicate that the particles entered the magnetosphere close to Earth, perhaps in the cusp region, and provide no evidence that particles crossed the tail magnetopause and then were guided earthwards along magnetic field lines. It has even been shown that the magnetic structure of the magnetosheath can influence the propagation of the particles on their way into the magnetosphere.

The interplanetary medium

The HEOS experiments have made possible major contributions to the study of the interplanetary medium – that region filled by the solar wind and the Sun's magnetic field carried along with it. The HEOS-2 magnetometer (provided by the same scientific group as the magnetometer on HEOS-1) produced excellent measurements of this interplanetary magnetic field (IMF), which were started by HEOS-1 in December 1968. Knowledge of the IMF (although its average is very low and amounts to only one ten-thousandth of the Earth's surface field) is important not only for a study of its long-term variations and as a means of relating it to other simultaneous interplanetary observations such as solar wind plasma and solar particles, but also for the interpretation of data from balloons, rockets and other satellites in different regions of space. The IMF measurements obtained by the HEOS satellites over seven years, therefore, are of benefit to a world-wide scientific community and have been deposited at an early stage with the World Data Center.

Typically, near the Earth, the IMF is seen to point outwards from the Sun (positive polarity) for several days, and then to reverse its direction and point to the Sun (negative polarity) for the next few days. By comparing the IMF data (obtained by HEOS near the Earth) with those from the Pioneer-10 deep-space probe which was at a slightly different heliographic latitude, strong evidence was found that the percentage of positive polarity increased as the heliographic latitude became more northerly. Extrapolation of these observations to higher latitudes suggests that the interplanetary field there may be unipolar. If this were so, it would solve the mystery of the 'sector structure' of the interplanetary medium observed near the ecliptic plane. The ESA/NASA International Solar Polar Mission should provide the final answer.

Another basic part of the interplanetary medium is the solar-wind plasma (mostly protons and electrons) continuously flowing outwards from the solar corona at speeds around 400 km/s. Its variations, together with those of the IMF, are believed to be responsible for many near-Earth phenomena such as auroral activities, telecommunication conditions etc. The HEOS-2 solar-wind instrument not only measured the basic solar-wind parameters, such as density and bulk velocity, but also provided an improved 'three-dimensional' resolution of the flow direction and of the speed of the particles. This way it became possible to study microinstabilities occurring in the plasma. A new empirical relationship between plasma speed and proton temperature was found which takes into account that fast solar wind plasma obviously is predominantly heated in the direction perpendicular to the local magnetic field. Due to the high resolution of the instrument and a new technique of data evaluation rare constituents of the plasma, such as the helium isotope He^3, could for the first time be determined to a high accuracy by in situ measurements. On 4 August 1972, during the highly dramatic series of solar events, HEOS-2 observed the highest plasma velocities reported in the solar wind so far ($\sim$ 2000 km/s).

Energetic charged particles accelerated on the Sun in a solar flare propagate through different media on their way from the acceleration site to their observation on a satellite. They travel azimuthally in the solar corona from which they escape into the interplanetary medium where they propagate outwards along the spiral magnetic field lines. Analysis of measured intensity/time profiles of the particles at different energies, of their anisotropies, of their composition and of similar parameters measured on one or several spacecraft makes it possible to draw conclusions about propagation and acceleration processes in the different media.

The statistical study of the relative abundances of protons and alpha particles in 42 solar particle events, identified during the HEOS-2 lifetime, shows a high variability of the proton/alpha-particle ratio from event to event. Low p/α ratios are found only for events whose flare sites are magnetically well connected with the observer. It has been shown that the absence of low p/α ratios in events in the eastern hemisphere and near the western limb of the Sun follows as a consequence from the observations that the p/α ratio is correlated with the size of the event, and that the number of observed events strongly decreases with azimuthal distance of the flare location from the well-connected region. It has been demonstrated by different methods that the apparent heliolongitude dependence of the p/α ratios does not result from rigidity-dependent processes in the solar corona as had been claimed earlier by other investigators. One of these methods correlates data for the same events from two spacecraft widely separated in heliolongitude (HEOS-2 and Pioneer 10/11). The observed large variations of the p/α ratio from event to event are found to be due to different acceleration or storage conditions at the flare site.

The emission into interplanetary space of low-energy protons from

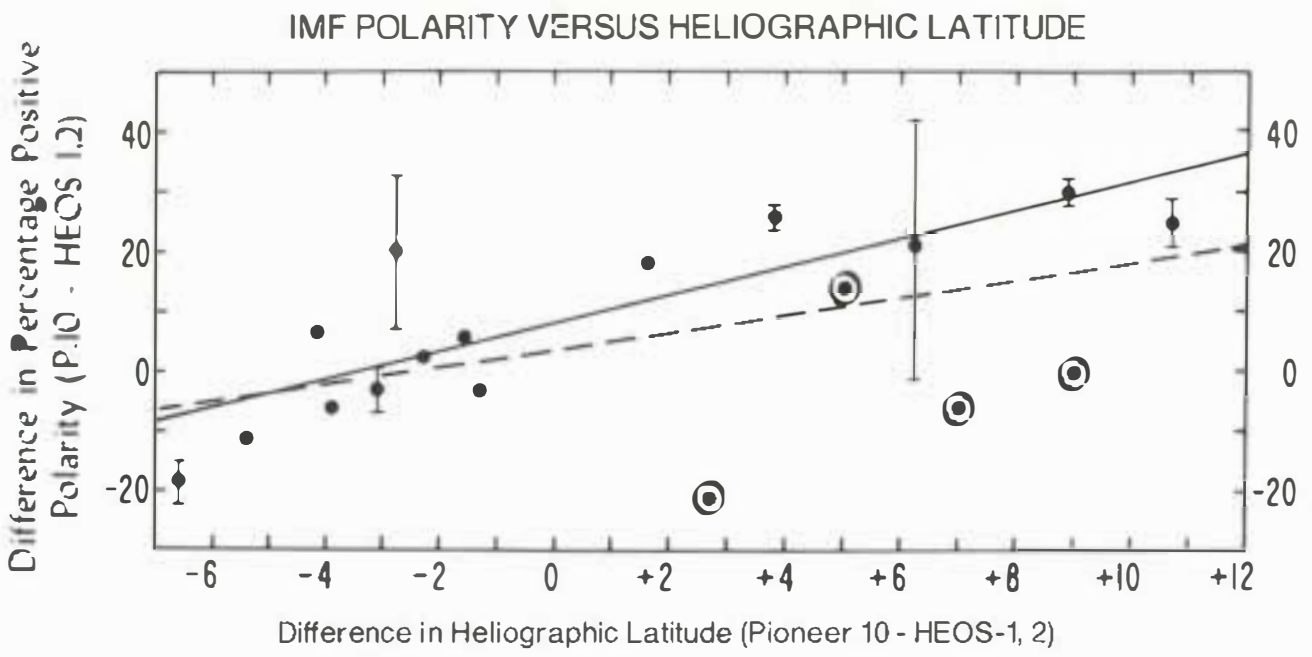

Figure 5. For Bartels solar rotations 1896-1913. the graph shows the percentage of positive polarity at Pioneer-10 minus that at HEOS-1 & 2 versus the heliographic latitude. in degrees. at Pioneer-10 minus that at HEOS-1 & 2. The error bars are the uncertainties due to gaps in the Pioneer-10 data. The dashed line is the least squares fit using all data points. The four solar rotations with the highest average solar-wind velocities are circled. The solid line is the least squares fit to data points other than these four high-velocity points (S 24A, S 201).

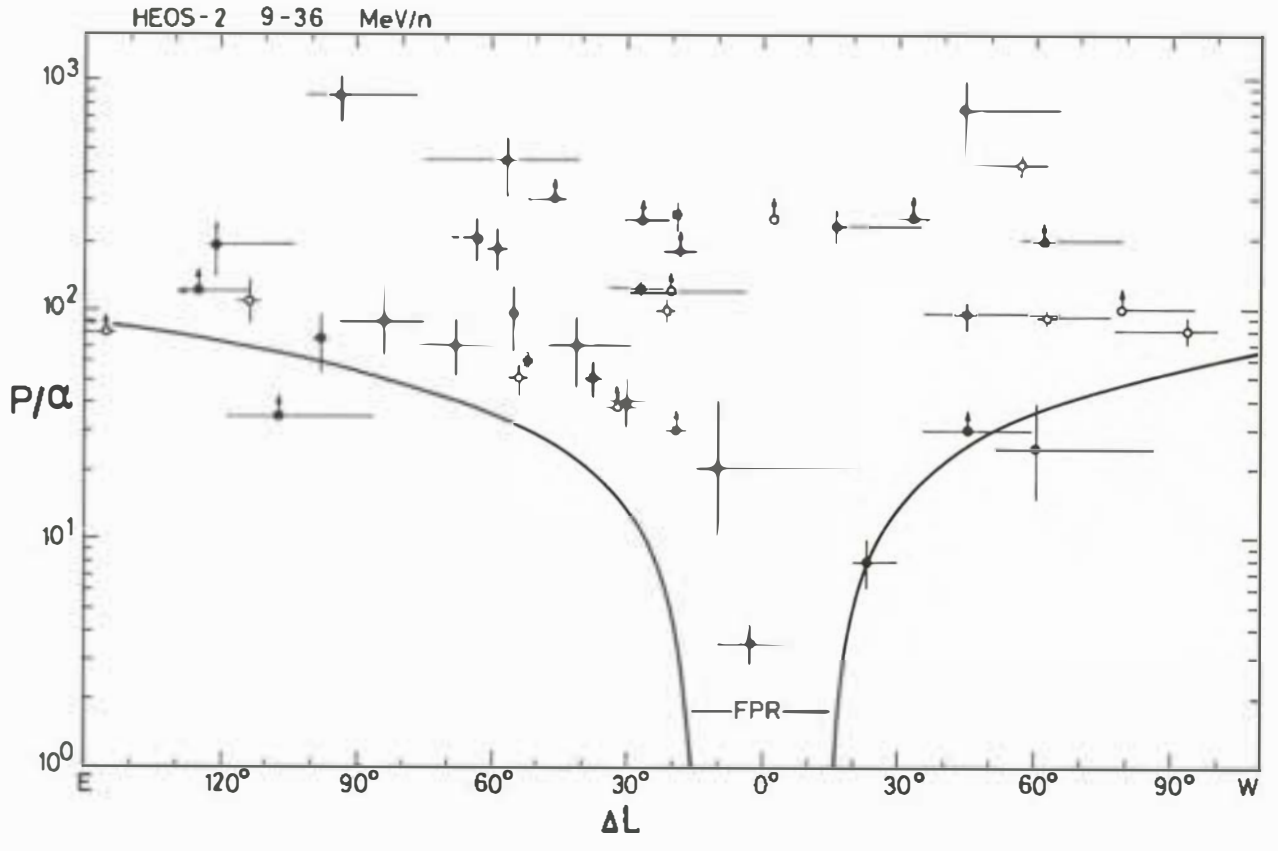

Figure 6. p/α ratios in solar events plotted versus the azimuthal separation ΔL between flare site and HEOS2 connection longitude. Full circles mark a clear flare association. open circles doubtful flare association. The observed increase of the p/α ratio with increasing distance is in good agreement with the theoretical curve. which separates the allowed upper from the forbidden lower region. Around $\Delta L = 0$ one finds the fast propagation region (FPR) (S204).

a solar flare is a function of the topology of magnetic fields in the corona. By the technique of 'mapping back' to the upper corona using simultaneously measured solar-wind data, it is possible to relate particle fluxes measured near the Earth to fluxes in the upper corona, and so investigate the gross scale of coronal control. Analysing the HEOS-2 observations of the 5 March 1972 event, it has been clearly demonstrated that the particles observed near the Earth did not come directly from the flare site but from a large chromospheric cell which had the same polarity as the acceleration region, but was $60° - 100°$ away from it. Step-like features in the near-Earth intensity/time profiles coincided with chromospheric neutral lines when mapped back, suggesting that coronal structures can strongly control the particles and that such structures can be preserved in interplanetary space out to at least 1 AU, for example along tangential discontinuities in the interplanetary medium.

Observations made simultaneously by the solar-particle, magnetometer and solar-wind-plasma experiments on HEOS-2 and other interplanetary spacecraft have been combined and studied, and as a result, understanding of the particle transport in the interplanetary medium has improved. It has been found that the particles obediently follow interplanetary magnetic flux tubes and show great reluctance to pass from one tube into its neighbours. The tubes may get entwined in such a way that the particles arrive near the Earth very late in the event or that they even appear to be streaming sunwards at times, but always along the local magnetic field.

In total 431 dust particles in the mass range between 10^{-15} g to 10^{-10} g ($1/10 - 10\,\mu$m diameter) have been registered by the dust experiment on the HEOS-2 satellite. In view of the time intervals Δt between consecutive events, the observed particles could be divided into three categories: random particles with $\Delta t > 6.5$ hr and bursts of particles with $\Delta t < 6.5$ hr, subdivided into groups with 10 mn $< \Delta t < 6.5$ hr and swarms with $\Delta t < 10$ mn.

Random particles and groups show constant fluxes between 60 000 km altitude and apogee. Below 60 000 km altitude the particle fluxes are enhanced by typically a factor of 3 in comparison with altitudes above 60 000 km. It could be shown that the groups are correlated with the position of the Moon. They are, therefore, interpreted as fine-grained ($\sim 10^{-14}$ g) lunar ejecta produced by meteoroid impacts on the lunar surface.

The most interesting discovery is the swarms of particles, observed exclusively within 10 Earth radii distance from the Earth's surface and not observed in deep space (except in meteor streams) which suggests a production by fragmentation of meteoroid parent bodies at ~ 10 Earth radii by a so far unknown mechanism. Charging of particles as they travel through the Earth's auroral zone has recently been proposed as a fragmentation mechanism. (Charging as high as -10 kV has been observed on satellites). Also, theoretical calculations show that a negative charge is to be expected.

Meteoroids show a wide variety of structure strength both from studies of meteor streams and from recent collection results. Normal iron and stone meteorites (ordinary chondrites) are generally of considerable strength with densities ranging between 3 to 8 g/cm^3. One third of the meteors, however, is of very low density (down to 0.1 g/cm^3) appearing to consist of so-called fluffy-type particles (loose conglomerates of 2 to 3 μm diameter size). Such meteors are of low strength, i.e. comparatively weak forces are able to separate them into the individual constituents. Thus both theory and observation suggest that it is meteoroids of this type that are fragmented by electrostatic break-up processes within a distance of < 1 Earth radius when travelling through the auroral zones.

Fifteen of these swarms were observed within the 2.5 years of observation. The parent bodies have been estimated to be between 10^2 and 10^6 g. By these processes the flux of submicron-sized particles within 10 Earth radii is enhanced by 2 to 3 orders of magnitude on average.

TD-1

UV, X & γ-ray astronomy

TD-1 was the first ESA satellite devoted to astrophysical studies. Launched in March 1972 into a Sun-synchronous orbit on a Thor-Delta rocket (hence its name), it transmitted scientific data until May 1974 when attitude control was lost on exhaustion of the on-board gas supply. The operational period achieved was some four times the originally planned six-month mission.

Scientific mission

The prime aim of TD-1's scientific mission was to conduct a systematic sky survey in the ultraviolet, X- and γ-ray regions of the electromagnetic spectrum. In addition, one experiment measured heavy cosmic-ray nucleii and two instruments sensitive to X- and γ-rays were maintained pointing at the Sun. The scientific groups involved and the complement of seven experiments flown are summarised in Table 1. The two ultraviolet telescopes provided complementary information. While S2/68 scanned the entire celestial sphere with a resolution of 35 Å in its spectrophotometric channels, the independent tracking system of S59 made it possible to achieve 1.8 Å resolution by observing selected stars for longer periods. In both sensitivity and sky coverage, the ultraviolet instruments on TD-1 represented a considerable advance over the pioneering observations in this field by the NASA OAO-2 spacecraft.

A Sun-synchronous orbit was selected for TD-1 to achieve the required complete sky coverage. The orbit was circular and inclined at 97.55° to the equator, with the satellite some 540 km above the Earth's surface. These parameters gave an orbital period of 95.5 mn and a precession rate of 360°/year or 4 arc min per orbit.

Table 1. TD-1 experiments

Experiment	*Scientific Group*	*Objective*	*Technique*
S2/68	Institut d'Astrophysique, Liège. Royal Observatory, Edinburgh; Astrophysics Research Unit, Culham	Multicolour celestial scanning in ultraviolet (1350-3000 Å)	Off-axis paraboloidal telescope and spectrometer with 4 photomultiplier detectors (1 photometric and 3 spectrophotometric channels).
S59	Space Research Laboratory, Utrecht	UV stellar spectrometry (2000-3000 Å)	Gimballed telescope-spectrometer with star tracking and spectrum scanning.
S67	Centre d'Etudes Nucléaires, Saclay	Spectrometry of primary charged particles	Two solid-state detectors coupled to a Cherenkov counter surrounded by plastic scintillator.
S77	Centre d'Etudes Nucléaires, Saclay	Spectrometry of celestial X-rays (2-30 keV)	Double proportional counter with beryllium plate window and collimator (parallel plates giving 1.45 × 11° field of view).
S88	University of Milan	Solar gamma rays (50-500 MeV)	Combination of tungsten-sheet converter, directional Cherenkov radiator, energy analyser and anticoincidence scintillator.
S100	Space Research Laboratory, Utrecht	Solar X-rays (2-4-900 keV)	Cesium iodide scintillation crystal with photomultiplier and solid-state background detector.
S133	Centre d'Etudes Nucléaires, Saclay. University of Milan. Max Planck Institut, Garching	Celestial gamma rays (30-300 MeV)	Optical spark chamber with stereoscopic view and vidicon camera in combination with two particle counters, Cherenkov counter and anticoincidence dome.

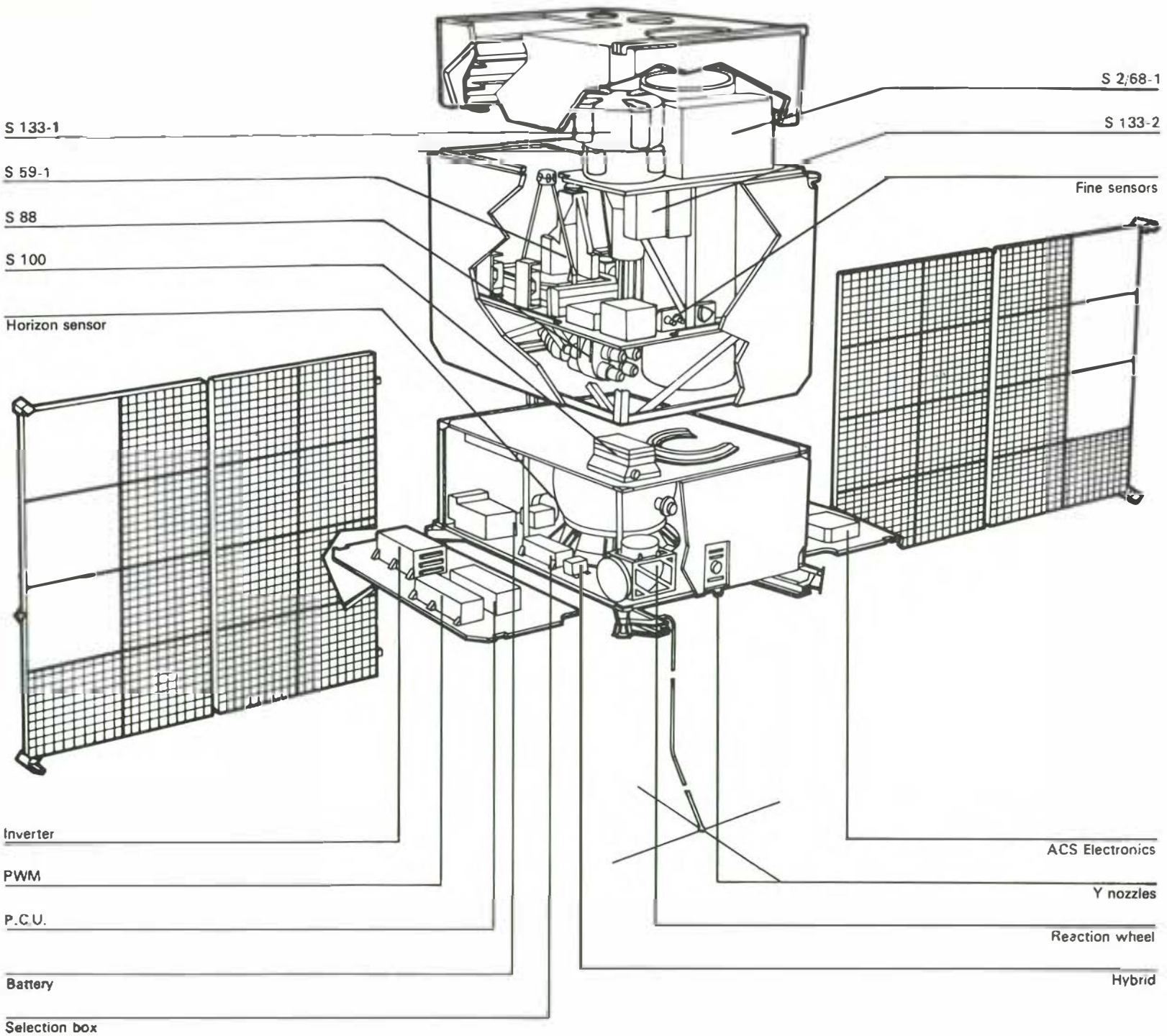

Figure 1. An exploded view of the TD-1 satellite, showing the positions of scientific experiments and spacecraft subsystems.

The triaxial attitude-control system was so designed that one spacecraft axis (the x axis) always pointed within 1 arc minute of the centre of the Sun while the satellite was rotated about this axis once per orbit. By mounting the sky-scanning experiments with their optical axes parallel to the main spacecraft axis (z axis), each was pointed constantly away from the Earth and covered a narrow strip of the sky during each orbit. Due to the orbital precession, this strip rotated about the ecliptic poles giving complete coverage of the celestial sphere in six months.

Spacecraft

An exploded view of the satellite is shown in Figure 1. The main structure was rectangular, comprising a bottom compartment containing functional subsystem equipment (power supply, electronics, stabilisation, attitude-control pneumatics, engineering systems etc.) and a top compartment containing the outward-viewing scientific instruments. These were constrained to view along either the x or z satellite axes, as described above, with the exception of the S59 ultraviolet telescope. In its stand-by mode this scanned along the ecliptic meridians together with the 27-cm aperture S2/68 telescope. Once a bright enough star entered its field of view, however, it had the additional capability of locking on and tracking the star with 1 arc sec accuracy for a period of 4 mn while spectral scans were obtained. The combined mass of the scientific instruments was about 120 kg out of a total mass of 473 kg for the spacecraft, whose dimensions were 2.2 m (height) $\times$ 1 m $\times$ 0.9 m. In addition, the satellite body also carried four solar paddles, which were hinged in pairs from the edges, and a 2.7 m long, deployable, boom-mounted antenna.

The telemetry system was designed to transmit data continuously to Earth at 1700 bps by a low-power transmitter (0.3 W). At the same time the data could be recorded on one of two on-board tape recorders and played back at high speed (30600 bps) for transmission by a high-power transmitter (3 W) during passage over a ground station. Each recorder was capable of storing the full data load of one orbit.

Performance in orbit

The TD-1 instruments performed extremely well during the mission and data are still being analysed and new results obtained more than 4 years after operations ceased in May 1974. Experiment S2/68 exceeded its design performance: the Sun baffle worked so well that stars down to magnitude 10.5 were measured (compared with a design aim of the 9th magnitude). S77, the celestial X-ray experiment, was suspected of interfering with the spacecraft encoder and had to be switched off early in the mission. This problem did not recur when the experiment was switched on again in July 1973, however, allowing the X-ray survey to be carried out during the second year of operation.

The frustrating aspect of TD-1 – with which those concerned were preoccupied throughout the mission – was the failure of both on-board tape-recorders. A seeming catastrophe in the beginning, the two courses of action taken by ESA prevented any serious loss of data. Firstly, using about 40 ground stations and with the help of many space agencies around the world, it proved possible to record about 70% of the data transmitted in real time. Secondly, by having its operational lifetime extended, TD-1 scanned the sky two and a half times, giving a final data coverage of more than 95% of the celestial sphere. This involved three periods of 'normal' operation separated by two periods of 4-5 months during which time the satellite was partially in eclipse on each orbit and could not be stabilised by means of the Sun sensors. In order to survive these two eclipse periods, the satellite was set spinning about its Sun-pointing axis to preserve approximate attitude until it was again in full sunlight. While in this mode, S2/68 was used in a novel way to study atmospheric and auroral emissions, and selection of a suitable spin rate during the second 'hibernation' period allowed S77 to scan the sky and fulfil its mission. Fortunately, during that period, one tape-recorder resumed operation. During the third period of normal operations it was used 60% of the time.

Although the tape-recorders were a source of irritation, and a considerable amount of extra work was involved in piecing together the data recorded by the various stations, their failure did not in the end detract from TD-1's undoubted scientific success.

Achievements

Ultraviolet studies

Both ultraviolet experiments, S2/68 and S59, provided a very large quantity of high-quality data of a significant value to the world's astronomical community.

The achievement of the mapping of about 95% of the sky by the S2/68 experiment enabled the first statistical studies of stellar and

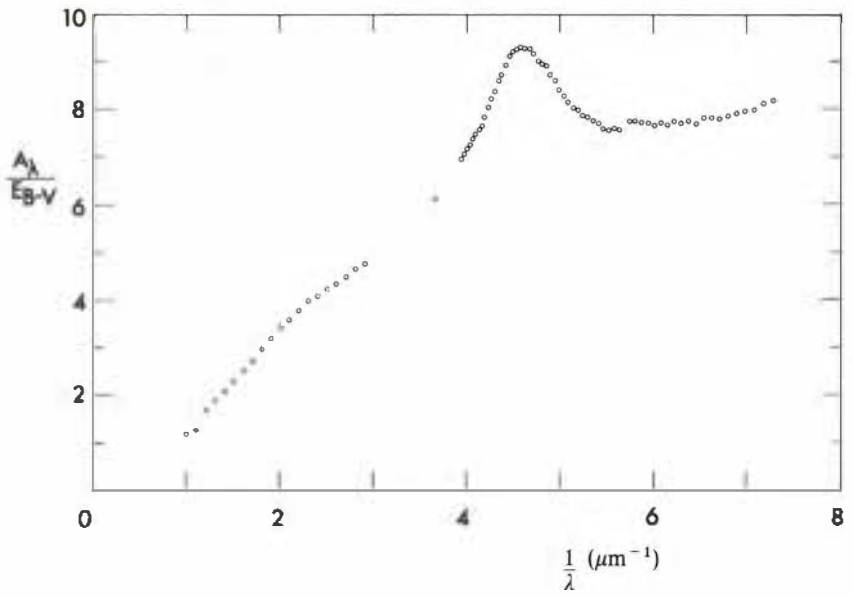

Figure 2. The mean interstellar extinction law.

interstellar ultraviolet characteristics to be performed. But first of all, it led to the publication of catalogues of absolute stellar fluxes. The *Ultraviolet Bright-Star Spectrophotometric Catalogue* was published by ESA in its Scientific Report Series (SR-27) at the end of 1977. It contains the absolute fluxes given at an interval of 20 Å between 1360 and 2540 Å (spectral range covered by the three spectrophotometric channels with a resolution of 35 Å), a broad-band photometric point at 2740 Å (310 Å effective passband) and a logarithmic spectrum of 1356 bright stars observed during the March-October 1972 period. About 65% of the stars fall into the visual magnitude range $4.5 \leqslant m_v < 6.5$. A supplement to this Catalogue, containing the spectra of bright stars observed in 1973 and in 1974 was published at the end of 1978 (ESA SR-28). A Faint-Star Catalogue, giving four broad-band photometric measurements (obtained by averaging the fluxes in each spectrophotometric channel) for about 30 000 stars has been published by the Science Research Council (UK).

The second major scientific aim of the S2/68 experiment was the study of the interstellar extinction law. Knowledge of this law is important both for studies of the interstellar grains believed to be responsible, and for the correction of the observed spectra of stars which are reddened as a result of the wavelength dependence of the extinction. The mean interstellar extinction law (Fig. 2) obtained by comparing spectra of several tens of reddened and unreddened stars of the same spectral type shows as striking feature an absorption band centred at 2180 Å. Because of its symmetrical nature, it could not have been produced by the same grains as those responsible for the general extinction (by scattering) throughout the ultraviolet and the visible. Strong candidates for the role of absorber are small particles of graphite.

The S2/68 experiment has proved to be particularly valuable for examining the galactic dependence of the ultraviolet extinction law. The extent to which the mean extinction curves derived for nine galactic regions deviate from the mean curve for the Galaxy cannot be regarded as significant. A few individual stars do, however, show a significant deviation, which could be circumstellar. The measurement of the strength of the 2180 Å absorption feature and an ultraviolet colour excess give similar galactic distributions of dust: as a result, the reddening per kpc is considerably less in the direction of Vela-Puppis than in other directions and the scale height of the dust off the galactic plane is (110 ± 10) pc.

One of the outstanding characteristics of S2/68 is the absolute calibration of the instrument, which was performed very carefully. The measurements made independently three months before the launch by two of the groups engaged in the project differed by less than 20%. The results show that the S2/68 observations have considerably improved the standard of absolute flux measurements performed by rocket and satellite experiments. It provides astronomers with material that is a valuable aid in calculating

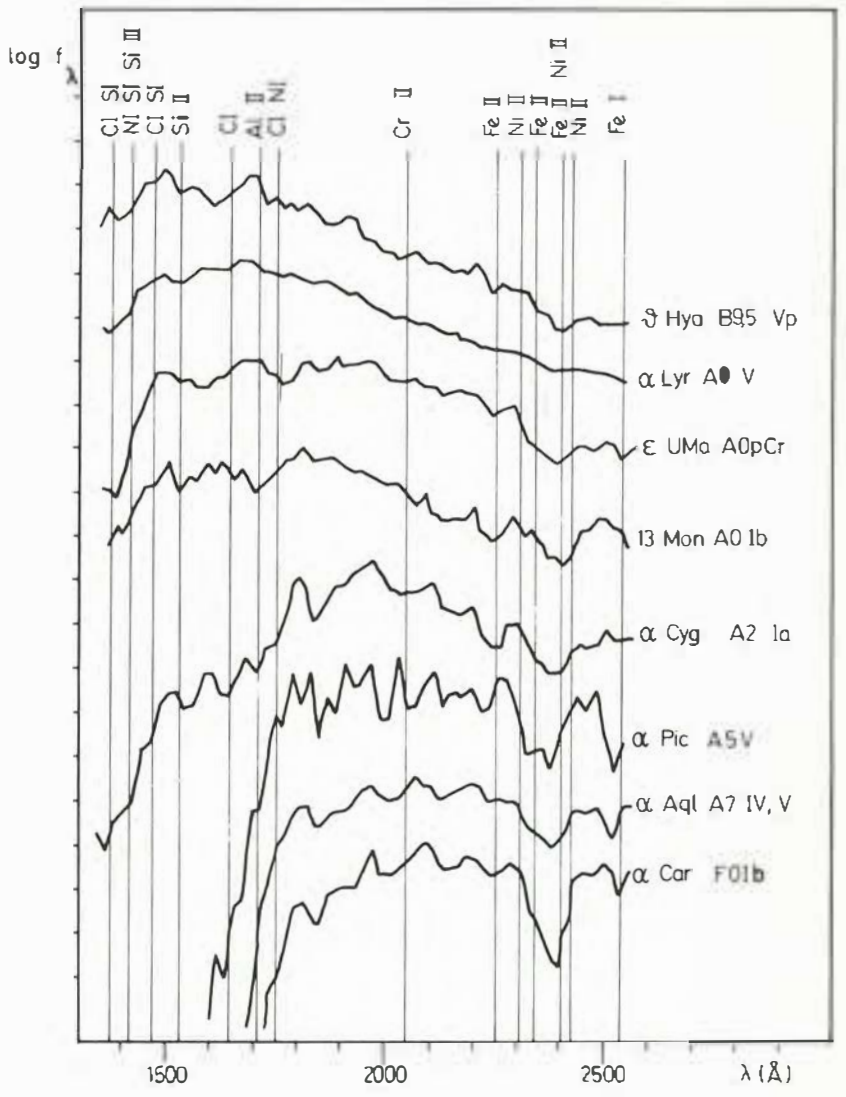

Figure 3. Flux received at the Earth on a logarithmic scale (units are: erg Å^{-1} cm^{-2} s) versus wavelength. One division in ordinate is 0.1. The spectra have been shifted arbitrarily relative to one another in ordinate.

bolometric corrections (difference between visual and bolometric magnitude) for early-type stars because the latter, being very hot, emit the bulk of their radiation in the ultraviolet. It also enabled the effective temperatures (basic parameter used in the models of stellar atmospheres) of these stars to be measured empirically.

Experiment S59, taking 1.8 Å resolution spectra of bright stars in three wavelength ranges of 100 Å each centred on 2110, 2540 and 2820 Å respectively, was complementary to S2/68. The success of S59 has been complete, since it has obtained around 3600 individual spectra of the 225 stars of the observation programme. When TD-1 was launched, very few high-resolution stellar spectra were available, so S59 has made a significant contribution to our knowledge of the ultraviolet stellar field. Although its success was somewhat overshadowed by the launch, six months later, of the Copernicus satellite, which has provided 0.05 and 0.1 Å resolution ultraviolet spectra, S59 remains an outstanding experiment in view of the accuracy of its relative photometric calibration.

The large number of stars observed with TD-1 has enabled several groups to investigate the validity of existing spectral classifications based on visible data and to propose additional criteria making use of the ultraviolet properties. Classification schemes based on both spectral features and on ultraviolet colours have been produced. As expected, the supergiant stars show considerably stronger lines than the main-sequence stars, owing to a larger microturbulent velocity. The spectrum of early B-types stars is dominated by lines of Fe III and Cr III, while those of B5 and later types show lines of Fe II and Cr II, and those of A and later type stars also contain lines of neutral species (Fig. 3). The prominent features, which are blends of many absorption lines at the S2/68 resolution, situated at 1410 Å (Si IV for the early B stars), 1550 Å (C IV and Fe III), 1620 Å, 1930 Å (Fe III), 2078 Å (Fe III) and 2400 Å (Fe II, Ni II) have been used for classification purposes. The 2800 Å (S59) channel spectra of all stars are dominated by the lines of the Mg II resonance doublet.

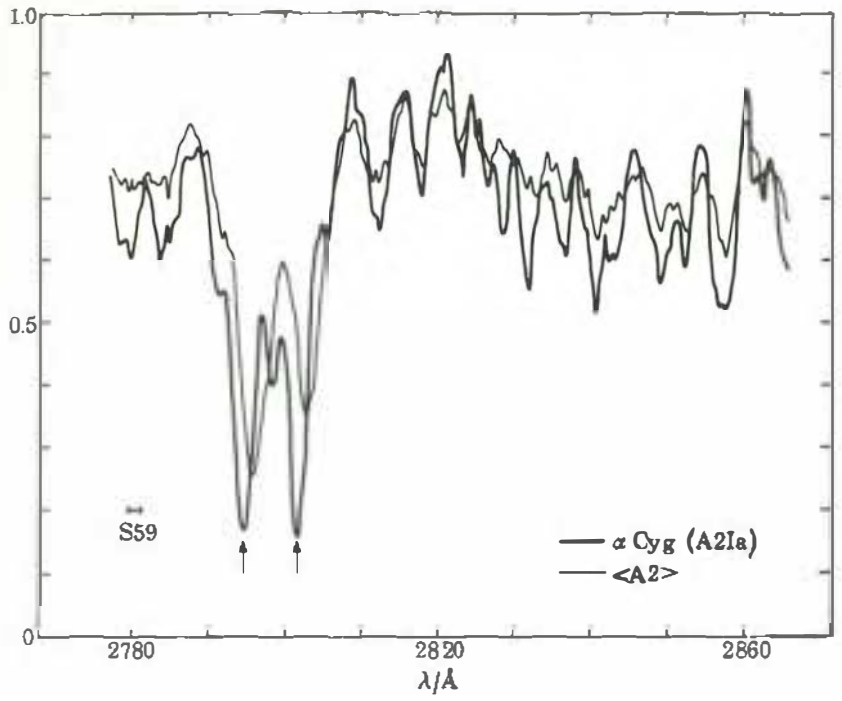

Figure 4. S59 spectrum of α Cygni from 2775 to 2865 Å compared with the corresponding spectrum of an average A-2 star.

While in the case of the hottest (O-type) stars these lines are partly of interstellar origin, they are for the other stars an important temperature criterion. Since the strength of these lines is very sensitive to non-LTE effects (departure from the hypothesis of local thermodynamic equilibrium), their study is of great importance for the determination of the detailed structure of the stellar atmosphere and its radiation field. The measured equivalent widths agree reasonably well with predictions based on model atmosphere calculations and the abundance of Mg derived from the observations agrees very well with the values obtained for the solar photosphere. An analysis of the detailed structure of the Mg II lines (blue shifted cores and extended blue wings) shows that the supergiant A2 Ia Cygni (Fig. 4) is losing mass at a very significant rate (3×10^{-10} solar masses per year).

For fainter stars, it is necessary to combine the spectral data into wider bands to give statistically useful results. Classification parameters can be obtained from a study of the spectral energy distribution, stars being grouped according to their intrinsic flux distributions. A scheme based on the 2740 Å, 2190 Å, and 1490 Å wavelengths chosen to avoid strong spectral features and to include the maximum interstellar extinction has been revealed to be very efficient.

The S2/68 and S59 observations have made it possible to test the validity of computed synthetic spectra which include the opacity of several thousands of atomic lines. The proposed theoretical spectra agree well with the observed spectra of main-sequence stars.

Several detailed studies have contributed to a better knowledge of classes of objects (Wolf-Rayet, Be, Ap, βCMa stars...) or individual stars. The strength of He, C and N lines analysed using a non-LTE treatment has provided the first reliable determination of the physical and chemical nature of a number of Wolf-Rayet stars. A large number of Ap stars with different chemical peculiarities (first large-scale study of this type of stars in the ultraviolet) and of Be stars have been studied for their spectral characteristics and for their variability. A striking feature situated at 1400 Å in the spectra of the Si Ap stars seems to be caused by a group of auto-ionisation lines of the abundant ion Si II. The photometric variability of the Be stars in the ultraviolet was observed for the first time with the S2/68 experiment.

The wide sky coverage and the sensitivity of the S2/68 experiment has made it possible to study the dust distribution in our Galaxy, as mentioned above, but also to give the first indication that there may be a substantial population of hot stars (comparable to that of main-sequence stars) lying a few magnitudes below the main

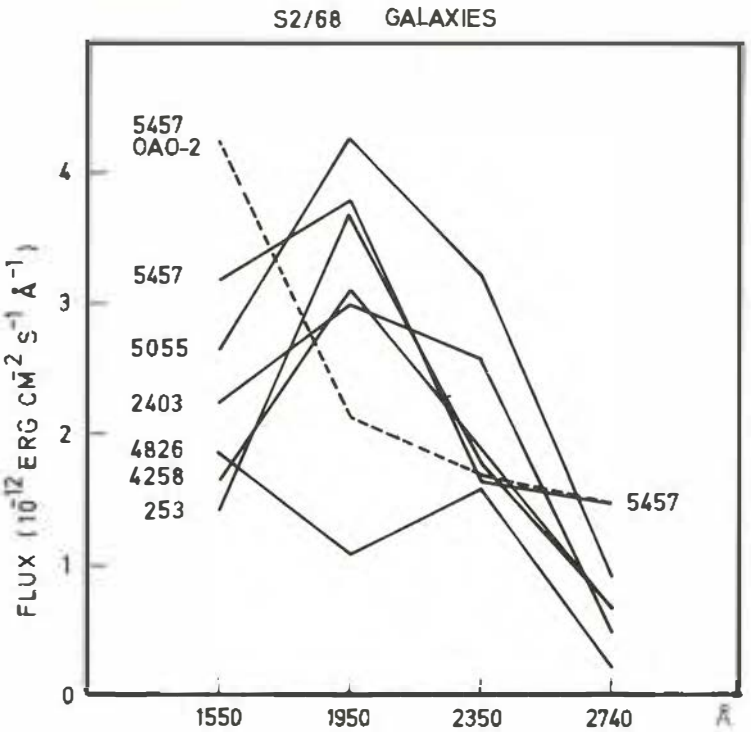

Figure 5. S2/68 fluxes in four wavebands for six nearby galaxies together with the OAO-2 data (dashed curve) for one of them. NGC 5457.

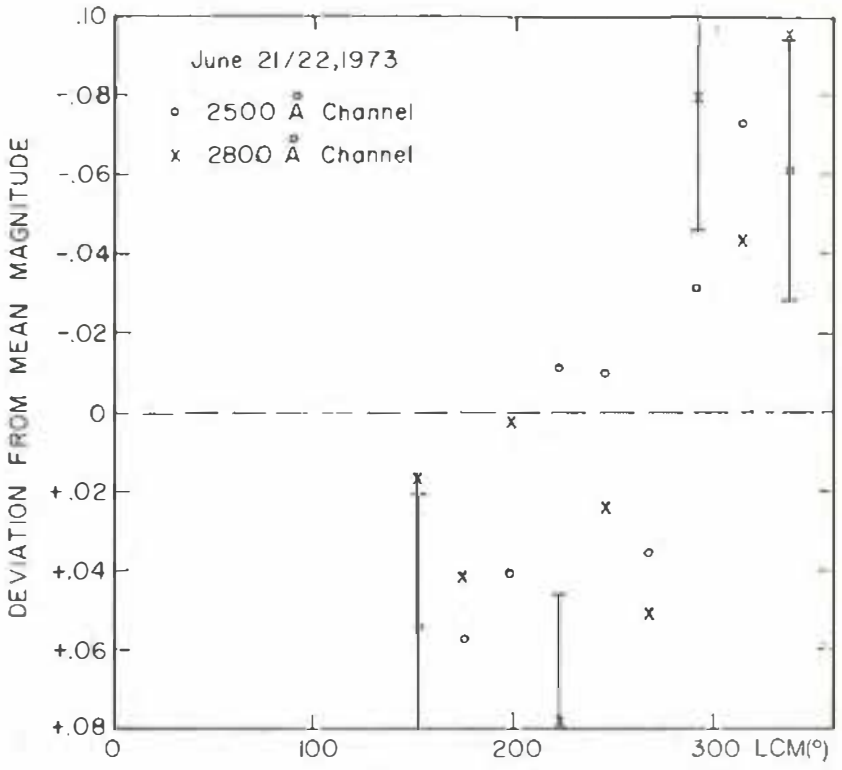

Figure 6. Variability of Mars on 21/22 June 1973, as observed by S59 during a non-storm period. During the period preceding the S59 data, there were no unusual clouds in blue and ultraviolet; the cause of the brightening is therefore unknown (LCM = longitude of the central meridian).

sequence. Their distribution on the sky suggests that they are mainly population-II objects. The search for blue objects led to the discovery of new very hot sub-dwarfs and of several new binary systems in which a hot secondary orbits a late-type primary which dominates at visible wavelengths.

Among the few nearby galaxies the flux of which has been measured with S2/68 (Fig. 5), the Magellanic Clouds which lie close to the south ecliptic pole have been scanned a very large number of times. The ultraviolet maps of the LMC show that the prominent ultraviolet features are easily identifiable with corresponding features in the visible.

A few bright outer planets have been observed with S59 and S2/68. Combination of the S2/68 data with the solar spectrum, degraded to the same spectral resolution, demonstrates that Jupiter and Saturn have very similar albedos between 1700 and 2500 Å, with an absorption at 1900 Å. On the basis of S59 and OAO-2 studies of Saturn, it is suggested that, in contrast to the first conclusions, NH_3 does not influence the ultraviolet spectrum of these planets, and that H_2S could be a candidate for the absorber. S59 high-resolution data on Mars reveal no definite absorption feature; the absence of NO absorption can be reconciled with the preliminary Viking measurements only if that gas is preferentially concentrated at high Martian altitudes. According to the same S59 data, Mars showed a diurnal brightness variation during a non-storm period (Fig. 6).

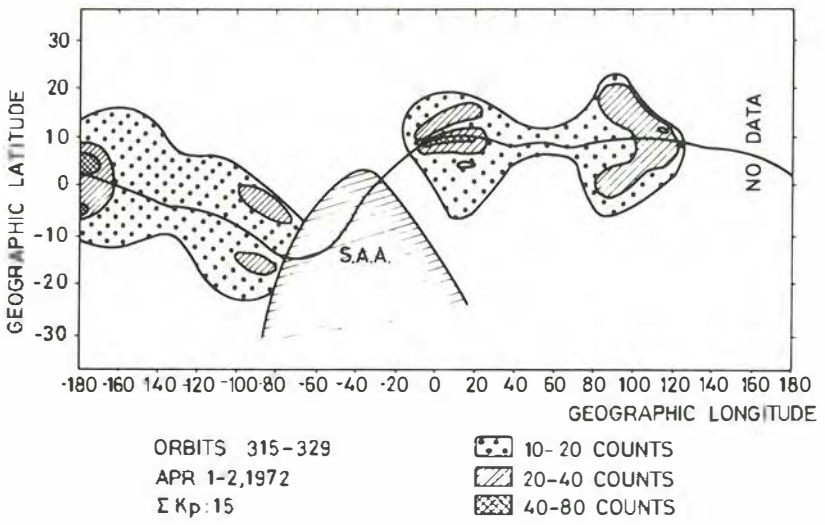

Figure 7. Isophote map of the ultraviolet Mg II dayglow measured by S2 68 and plotted in geodetic coordinates. The shaded area (SAA) is the South Atlantic Anomaly region where the particle noise prevents airglow measurements.

Figure 8. Time profiles of the solar X-ray flare of 2 August 1972 observed with the S100 experiment. The four recordings refer to the four energy channels 29-41 keV, 41-53 keV, 53-75 keV and 75-107 keV. The dashed lines only outline the positions of the seven elementary flare bursts into which this event can be decomposed.

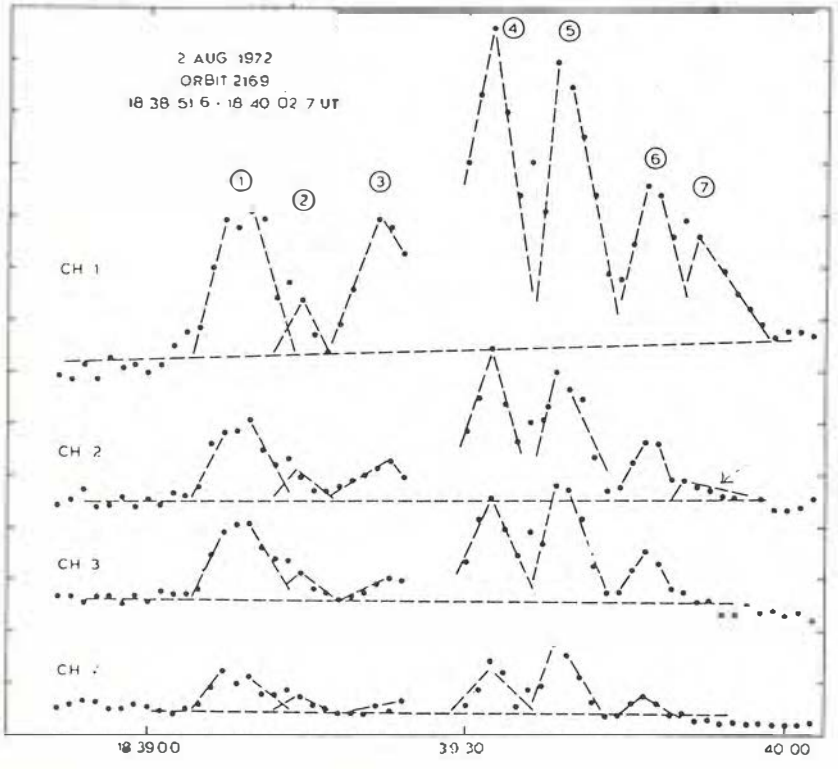

As shown above, the stellar ultraviolet experiments have provided very rich astronomical results. Quite accidently, S2/68 has also served as a useful tool for investigating geophysical phenomena. As early as the first orbit the long wavelength photometric channel detected a significant increase above the background, near the equator, restricted to the dusk part of the orbit. This effect has been explained as emission caused by the resonance scattering of sunlight above the satellite by Mg II at 2800 Å. These ions are lifted up from the meteoric ablation region by the so-called 'fountain effect' (Fig. 7). These observations give an exceptional opportunity of detecting longitude and time effects on the $\bar{E}$ field configuration. The end of the second scan period in October 1973 completed the scientific information (distribution of the Mg II ion with altitude) by scanning the atmosphere with the telescope turning around the Sun-pointing axis during the spinning mode of the satellite.

X-ray studies

Results obtained with the celestial X-ray experiment (S77) have been somewhat overshadowed by the wealth of more recent data from dedicated X-ray satellites. The instrument performed well during the second half of the mission, however, and several sources, including the Crab Nebula, Sco X-1 and Cygnus X-1, were detected as well as auroral X-ray emission from the Earth.

The solar X-ray experiment (S100) operated throughout the mission and provided important detailed insight into the nature of solar flares. Spectra above 25 keV were obtained for several flares

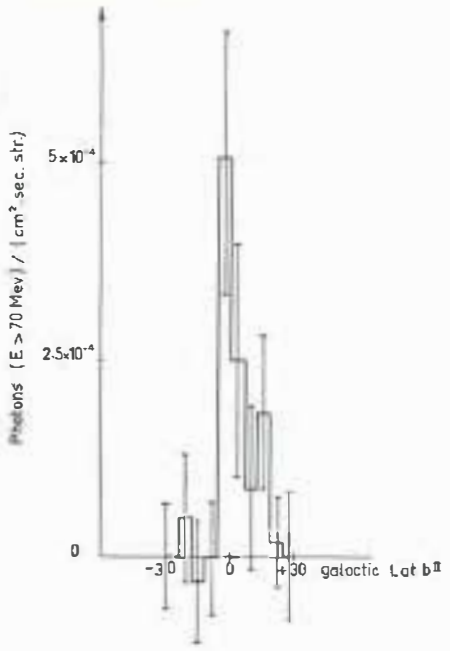

Figure 9. Distribution of gamma rays (E >70 MeV) measured by S133 summed from $l^{II}=330°$ to $l^{II}=30°$ as a function of b^{II}. The local background has been subtracted.

observed with a time resolution of 1.2 s. Figure 8 shows the time profiles at different energies for the intense flare of 2 August 1972. The observations suggest the existence of two phenomenologically different types of X-ray flares. One produces strong, long-lasting (~1000 s) X-ray emission while the most commonly observed are relatively short (~100 s) and extremely time variable. The X rays are produced as bremsstrahlung and the time profile reflects variations in the electron acceleration. An important conclusion from the detailed analysis is that each short-lived flare can be further decomposed into a number of 'elementary flare bursts' (EFB) in which all the radiation is concentrated. For one and the same flare, each EFB has roughly the same time profile but these differ markedly for different flares. In view of the enormous number ($\sim 10^{36}$ e/s) of electrons required to produce the observed hard X rays, it is argued that acceleration by a static electric field can be ruled out and that fluctuating electric fields due to plasma turbulence must prevail. These conclusions form the basis of rather detailed models developed by the Utrecht group.

γ-ray studies

The solar γ-ray experiment (S88) was unfortunately swamped by too much local background emission to yield a positive result. This background, caused by cosmic-ray bombardment of the spacecraft, was some two orders of magnitude higher than expected and also reduced the effectiveness of the celestial γ-ray instrument (S133). By applying stringent selection criteria to some 12 000 recorded events, however, it proved possible to substract the local background and reveal the prominent γ-ray excess in the galactic centre direction (Fig. 9). A full perspective of the success of the γ-ray experiments on TD-1 must take account of the invaluable experience gained in this field and applied so successfully to the γ-ray dedicated satellite (Cos-B) which followed.

Cosmic-ray studies

The origin and propagation of cosmic rays through space have long been subjects of speculation and limited progress. While not supplying the final answers to these fundamental questions, Experiment S67 has provided important information on the abundance of heavy ions in the primary cosmic rays. The great advantage of satellite data over that obtained previously with balloon-borne experiments is that no correction is necessary for the residual atmosphere above the detector. With S67 the group at Saclay were able to measure heavy nuclei with charges ranging from 2 (lithium) to 30 (zinc) as a function of charge and energy. One important conclusion from the data obtained is that the pathlength of material traversed by cosmic rays appears to decrease with increasing energy. This clearly is an important fact to be accounted for by any propagation theory.

Conclusion

TD-1 was an extremely ambitious and complex satellite with which to pioneer ESA's astrophysical programme. Although carrying seven experiments with widely different objectives, there were few disappointments with the results obtained. The ultraviolet experiments were an unqualified success – performing beyond realistic pre-launch expectations. Bearing in mind the restricted resources of mass and volume, the X- and γ-ray experiments also proved encouraging for further exploration at these energies, with larger dedicated satellites. This has already been achieved at γ-ray energies with the highly successful Cos-B mission and will be extended to the X-ray region with ESA's next scientific satellite (Exosat). The participation of ESA in the International Ultraviolet Explorer (IUE) and Space Telescope (ST) programmes has also ensured a continuing opportunity to expand the ultraviolet studies begun with TD-1.

ESRO-4

Near-Earth ions

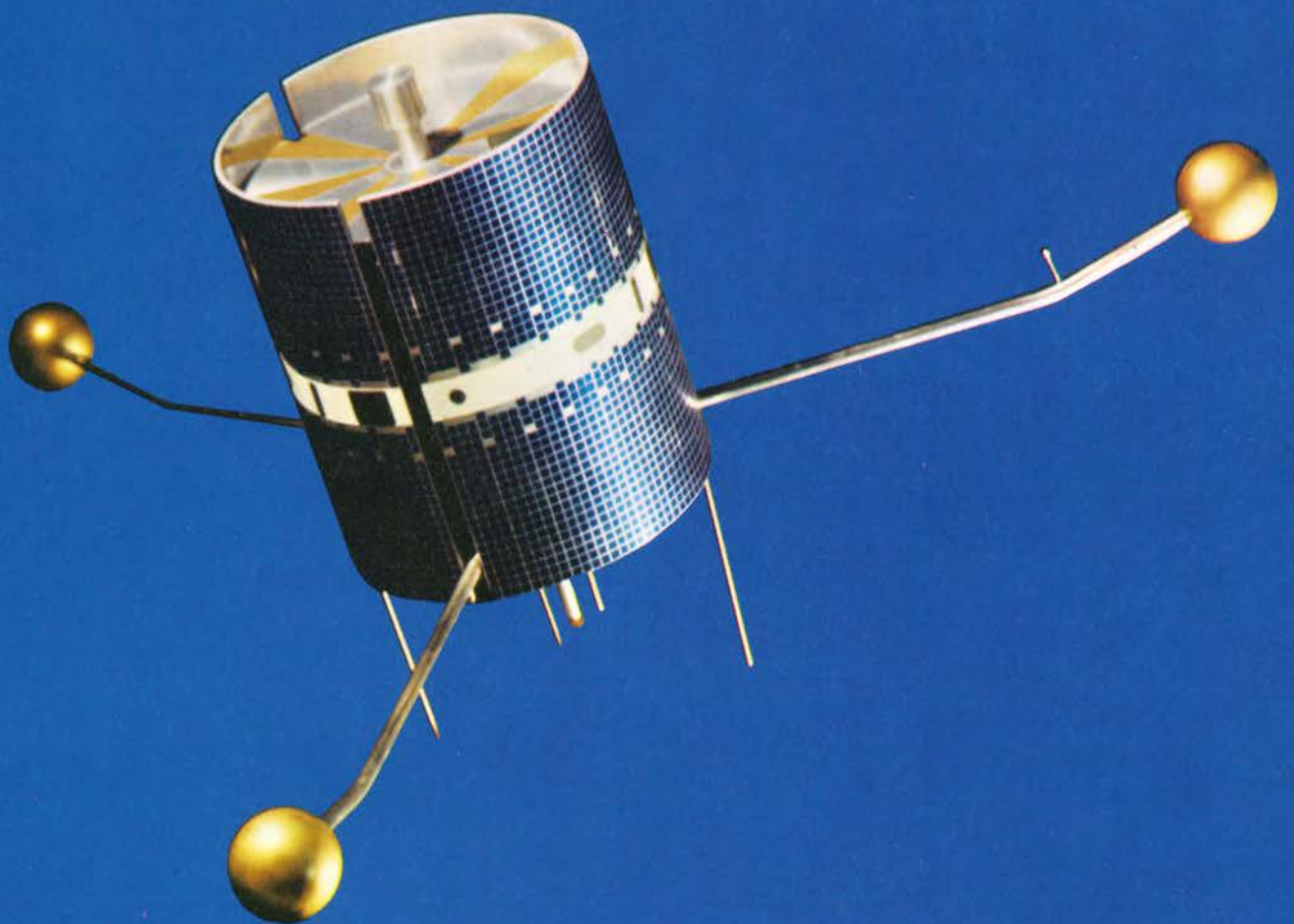

ESRO-4 was the first mission ever to measure the neutral atmospheric ions successfully. Launched on 22 November 1972 from Western Test Range, USA, into a low, elliptical, polar orbit, it re-entered the atmosphere on 15 April 1974, after having completed 7685 orbits.

Scientific mission

The scientific mission was divided into two distinct areas, each concerning a different part of the magnetosphere. Three experiments concentrated on an analysis of the atmosphere and ionosphere:

- a neutral gas analyser,
- an array of ion and electron probes,
- a battery of auroral particle spectrometers.

The remaining two were designed to investigate the radiation belts and the penetration of solar-flare protons and electrons into the magnetosphere. These were both high-energy-particle telescopes having similar energy ranges but using slightly different techniques.

The experiments were originally intended to be part of the payload of a large, sophisticated, accurately stabilised platform. This was judged to be too ambitious for so youthful an organisation as ESRO, and it was therefore cancelled. ESRO-4 was thus set up as a cheap, small, spin-stabilised 'lifeboat' to rescue those experiments which did not need the accurate stabilisation of a large platform.

Spacecraft & experiments

The spacecraft was basically a drum 90 cm long, 76 cm in diameter and weighing 130 kg. Three radial booms, each 130 cm long, were mounted on hinges at the lower edge of the solar array. One of these carried the ion mass-spectrometer probe in the shape of a 20-cm diameter ball. Similar balls, but dummies, were carried on the other two booms to balance the 'active' boom and help to make available an electrically clean area of approximately 5000 cm^2 to prevent the spacecraft becoming negatively charged. The 'active' boom also carried a tiny Langmuir probe to give information on electron temperature. A third spherical probe, intended to monitor the total ion density, was mounted on a fourth boom and deployed axially in the opposite direction to the spin vector.

The neutral gas analyser, mounted axially on the forward surface, was very sensitive to contaminative gases produced by the spacecraft itself. So great care was taken to use no materials on the upper surface or sides of the spacecraft that would give off or absorb gases. This top surface was carefully sealed so that no outgassing vapours from the inside of the spacecraft could reach

Table 1. ESRO-4 experiments

Experiments	*Investigating group*	*Measurement*	*Technique*
S45	University College, London	Density, temperature and composition of positive ions.	Three boom-mounted spherical probes.
S80	University of Bonn	Density and composition of neutral particles in the mass range 1 to 44	Monopole mass spectrometer with radiofrequency analysing field.
S94	Geophysical Observatory, Kiruna	Pitch angle and energy spectra of electrons and protons in the range 0.5 to 150 keV.	Electrostatic analysers followed by channel multipliers. Higher energies with Geiger counters and solid-state detectors.
S99	Space Research Lab., Utrecht	Solar protons (2-100 MeV) and alpha particles (4-240 MeV) over polar regions.	Two solid state detector telescopes for the ranges 2-15 MeV (4-60 MeV) and 15-100 MeV (60-240 MeV).
S103	Max-Planck-Inst., Garching	Solar protons (0.2-90 MeV) and alpha particles (2.5-360 MeV) mainly over polar regions.	Solid-state detector telescope for 0.2-1.3 MeV (2.5-8.0 MeV). Solid-state detector stack plus scintillator for 1.3-90 MeV (9.5-360 MeV)

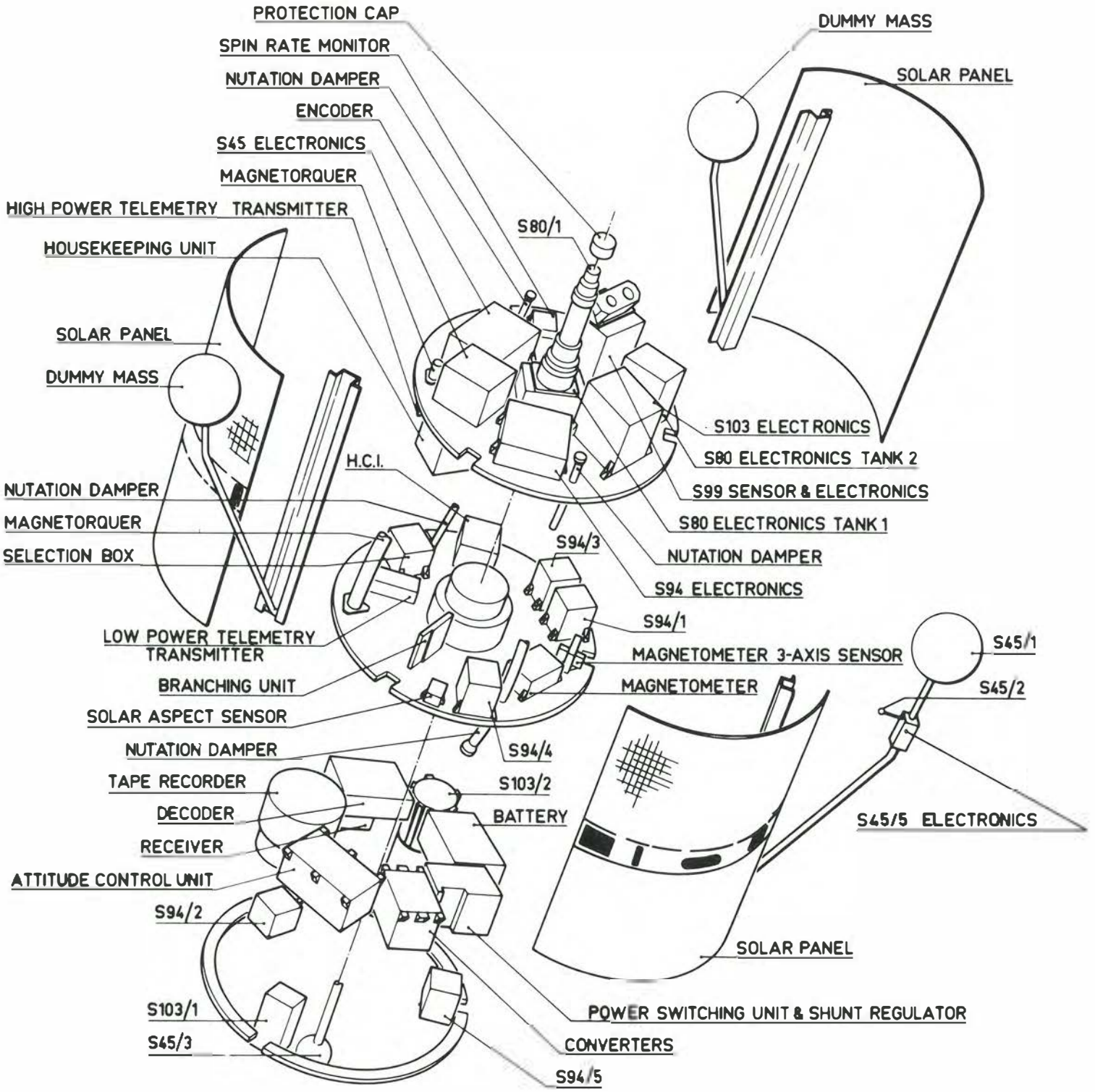
PROTECTION CAP
SPIN RATE MONITOR
NUTATION DAMPER
ENCODER
S45 ELECTRONICS
MAGNETORQUER
HIGH POWER TELEMETRY TRANSMITTER
HOUSEKEEPING UNIT
SOLAR PANEL
DUMMY MASS
NUTATION DAMPER
MAGNETORQUER
SELECTION BOX
LOW POWER TELEMETRY TRANSMITTER
BRANCHING UNIT
SOLAR ASPECT SENSOR
NUTATION DAMPER
TAPE RECORDER
DECODER
RECEIVER
ATTITUDE CONTROL UNIT
S94/2
S103/1
S45/3
S94/5
CONVERTERS
POWER SWITCHING UNIT & SHUNT REGULATOR
SOLAR PANEL
S45/5 ELECTRONICS
S45/2
S45/1
MAGNETOMETER
MAGNETOMETER 3-AXIS SENSOR
S94/1
S94/4
S103/2
BATTERY
H.C.I.
S94/3
S94 ELECTRONICS
NUTATION DAMPER
S80 ELECTRONICS TANK 1
S99 SENSOR & ELECTRONICS
S80 ELECTRONICS TANK 2
S103 ELECTRONICS
S80/1
DUMMY MASS
SOLAR PANEL

the analyser aperture. These measures were effective and the gas analyser suffered no contamination problems.

The tape recorder chosen for this spacecraft was a small, endless-loop type. Its proper operation was crucial for the global measurements that were necessary to meet the aims of the mission. At re-entry the tape recorder was still running without having increased its wow or flutter by a measurable amount since launch.

The five scientific experiments are summarised in Table 1. (A more detailed description of the mission and instruments by R. Jaeschke and J. Tunaley is to be found in ESRO SN-114, May 1972).

Performance in orbit

ESRO-4 was launched into a 91° retrograde orbit with an initial apogee and perigee of 1177 and 245 km respectively. This orbit was so designed that the nodal-scan rate and the perigee-precession rate were synchronised. This ensured that perigee positions and local times would be identical at six-monthly intervals, allowing comparison of summer and winter conditions on a world scale. The perigee precession rate was $-3.502°$ per day and the nodal-scan rate -3.5 mn per day.

The orbit was planned to have an apogee of 1080 km and a perigee of 280 km, but an injection error caused the perigee to be lower than expected. This increased the scientific value of the neutral analyser, but caused the apogee to drop to 700 km in one year, and re-entry occurred one month earlier than planned.

Achievements

Many spacecraft carry state-of-the-art developments of standard instruments into regions of space where the main characteristics are reasonably well-known, with the intent of discovering not what features exist, but why they exist. ESRO-4 was fortunate in that it carried a relatively new instrument into an area of space about which little was known and, just as important, neither the instrument nor the spacecraft developed faults which could have spoiled the mission. Thus, the ESRO-4 neutral-gas analyser was the first instrument to obtain global coverage for composition data at altitudes between 240 and 320 km. The significance of this can be assessed by the production of more than 70 papers from the measurements of this one instrument.

Neutral atmosphere studies

Scientifically, probably the most important outcome of the ESRO-4 measurements is a numerical model of global temperatures and densities of neutral gases in the upper atmosphere and how they change with the season. This will have many practical applications as well as high scientific value. This model was based on examination of 1.5 million spectra and, not surprisingly, took four years to complete. Extensive measurements of the composition of the upper thermosphere had previously been made by the neutral spectrometer on OGO-6 for the altitude range between 400 and 600 km. A mathematical approach to the data had been developed by the OGO-6 investigators and the ESRO-4 experimenters followed this, so that direct comparisons could be made between the OGO-6 and ESRO-4 models. Evaluation of the results show the two models to have significant differences. For instance, ESRO-4 figures for the global mean exospheric temperatures are 7% lower than for OGO-6 for conditions in which both models should apply, and ESRO-4 figures are supported by some recent papers in this field. Similarly, the temperature difference between summer and winter poles derived from ESRO-4 data is 315 K compared with 415 K from OGO-6. It is interesting to notice that ESRO-4 measurements were made when the solar activity was at a minimum, 2-3 years later than OGO-6, so it could be inferred that solar conditions have a dramatic effect on the upper atmosphere temperatures.

Figure 1 shows typical iso-density contours for the four gases which are found in the ESRO-4 region. The upper panels illustrate how the densities vary with the season and the lower how they vary with local time. There is a close similarity in the seasonal variations of nitrogen and argon, suggesting that these gases are strongly influenced by the thermal structure of the upper atmosphere. For oxygen the size of both seasonal and daily variations are remarkably small. The helium variations are dominated by the annual migration of the helium 'bulge'. The ratio of maximum to minimum densities exceeds 40 and even at the equator is considerable, making it difficult to separate out the weaker daily variations.

Superimposed upon the 'average' picture of the model are a large number of density and temperature fluctuations caused by a variety of mechanisms. Perhaps the most spectacular of these is the helium 'bulge' which is due to much higher helium densities over the

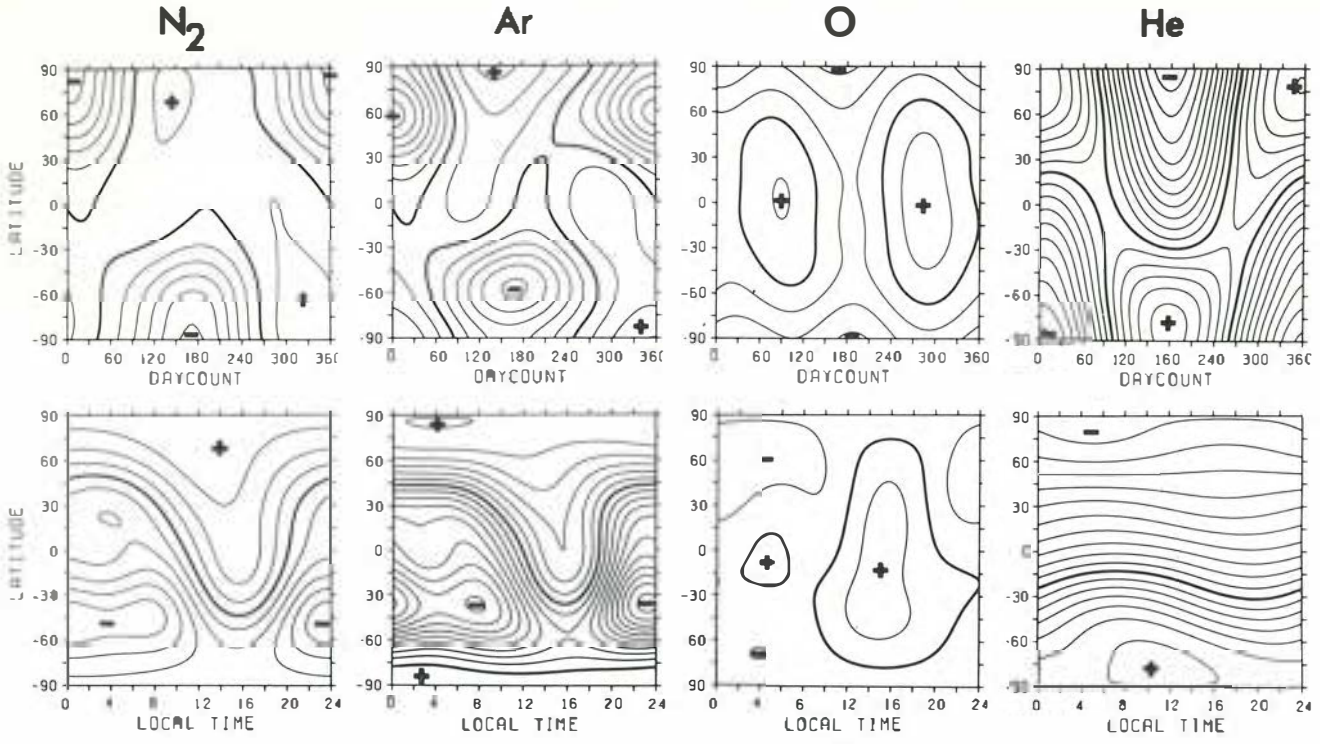

Figure 1. Isodensity contours of atmospheric constituents at 270 km altitude for $A_p = 4$ and $F_{10.7} = 92$. Global mean values are shown as thick lines. departure from the mean in steps of $\Delta^{10} \log n = 0.1$. For the upper panels the local time is 15.00 hr. For the lower panels the day of the year is 172.

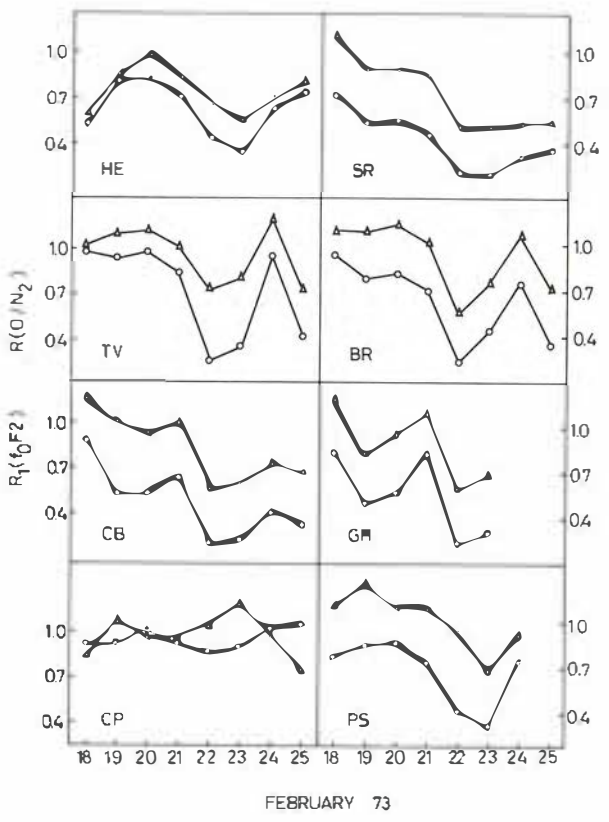

Figure 2. Comparison between the time variations in the critical frequency of the F_2 layer and in the O/N_2 ratio as observed at eight representative ionosonde stations during the time interval 18-25 February 1973. The changes in the critical frequency of the F_2 layer and O/N_2 are described in terms of the ratios $R_1(f_0F_2)$ (triangles) and $R(O/N_2)$ (circles) respectively.

winter pole of the Earth than over the summer pole. Since its discovery, it has caused a great deal of interest because it could be used as an indicator of particle migration into or out of the upper atmosphere. However, before the bulge can be used as a tracer it has to be thoroughly understood. The ESRO-4 measurements showed that the structure and movements of the bulge are more complicated than had originally been thought; for instance, over the pole the bulge sometimes has a peak, while at other times it has a 'crater'. The conclusion at present is that much more analysis has to be done before this bulge can be considered as useful.

Because helium is much lighter than the average gas in the upper atmosphere and argon is much heavier, these gases must react in opposite ways to the many dynamical processes in this region, such as vertical winds, changes in turbopause altitudes and so on, some of which presumably cause the helium bulge. Thus, when the ESRO-4 gas analyser made the first routine argon measurements at satellite heights, it was no great surprise that a *summer* argon bulge was immediately found. Nevertheless, the relationship between the helium and argon bulges is not so close as it appears to be at first, since analysis has shown that the helium bulge is caused mainly by dynamical processes, whilst the argon bulge is chiefly a temperature effect. Thus the way in which these bulges are formed is not entirely understood, although the key may well lie somewhere in the ESRO-4 data.

The influence of various types of geophysical disturbances on the neutral particles was investigated. The number densities were examined in an attempt to find global patterns during times of geomagnetic disturbance. The chief effect seems to be on the homopause. This is a surface at an altitude of about 85 km, below which the composition of the atmosphere is constant and does not change with height. The reaction of the homopause to geomagnetic activity is slow, being highest during sustained periods of disturbance and appearing to reach a steady height only after 2 or 3 days. Examination of shorter disturbances shows a correlation of density increase with K_p in a way which indicates a density wave which starts at high latitudes and moves equatorwards. The link of the upper atmosphere gases with geomagnetic disturbances seems rather tenuous. On the other hand, there appears to be a close association with ionospheric storms.

A noticeable feature of ionospheric storms is that during them ionosondes often find a decrease of the critical frequency of the F_2 layer, and in severe storms the critical frequency can fall so low that the F_2 layer is completely obscured by the F_1 layer. The most popular theory to explain this before the arrival of ESRO-4 was that changes in the neutral upper atmosphere composition caused drastic increases in the ionosphere loss coefficient, leading to decreases in ionisation and hence in the critical frequency. However, since practically no direct measurements of the neutral atmosphere compositions during ionospheric storms had hitherto been made, this concept could not be tested empirically. ESRO-4 measurements for the time of an extensive ionospheric storm in the southern hemisphere were inspected. During heat inputs into the neutral atmosphere, wide fluctuations of the nitrogen densities are seen, whilst oxygen densities vary little. So the O/N_2 ratio is a good indicator of the heating effect and accordingly this was the quantity examined. Figure 2 shows how the time variation of this ratio correlates with the critical frequency observation over eight ionosonde stations. A further demonstration of the correlation is to be found in Figure 3, where the normalised critical ratios are plotted against O/N_2 for all the data available during the storm. The upper plot uses the critical frequency from quiet days to normalise the disturbed F_2 frequencies and the lower uses the mean monthly value from February. Although there is considerable scatter, the strong connection between the critical frequency and the O/N_2 ratio is obvious, the correlation coefficients in both cases being about 0.8. This correlation leads to a number of highly interesting conclusions. The first is that the popular theory is correct, which leads to the idea of using data from ionosondes and from the spacecraft instrument to support each other. For instance, the critical frequency measurements could be used to find the onset of atmospheric disturbances, while the neutral composition measurement could be used to determine the extent of ionospheric storms (the latter is hard to determine from ground-based observations). The neutral atmosphere information may help to solve some puzzling aspects of ionospheric storms; for example, their unexplained global distributions may simply reflect the complexity of the neutral atmospheric disturbance. The time variations may be a function of the development of the atmospheric storm. These aspects of the measurements have to be investigated more thoroughly. Another point of interest is that the close association between atmospheric disturbances and ionospheric storms partially explains the hitherto perplexing lack of correlation between ionospheric and geomagnetic storms and suggests that the

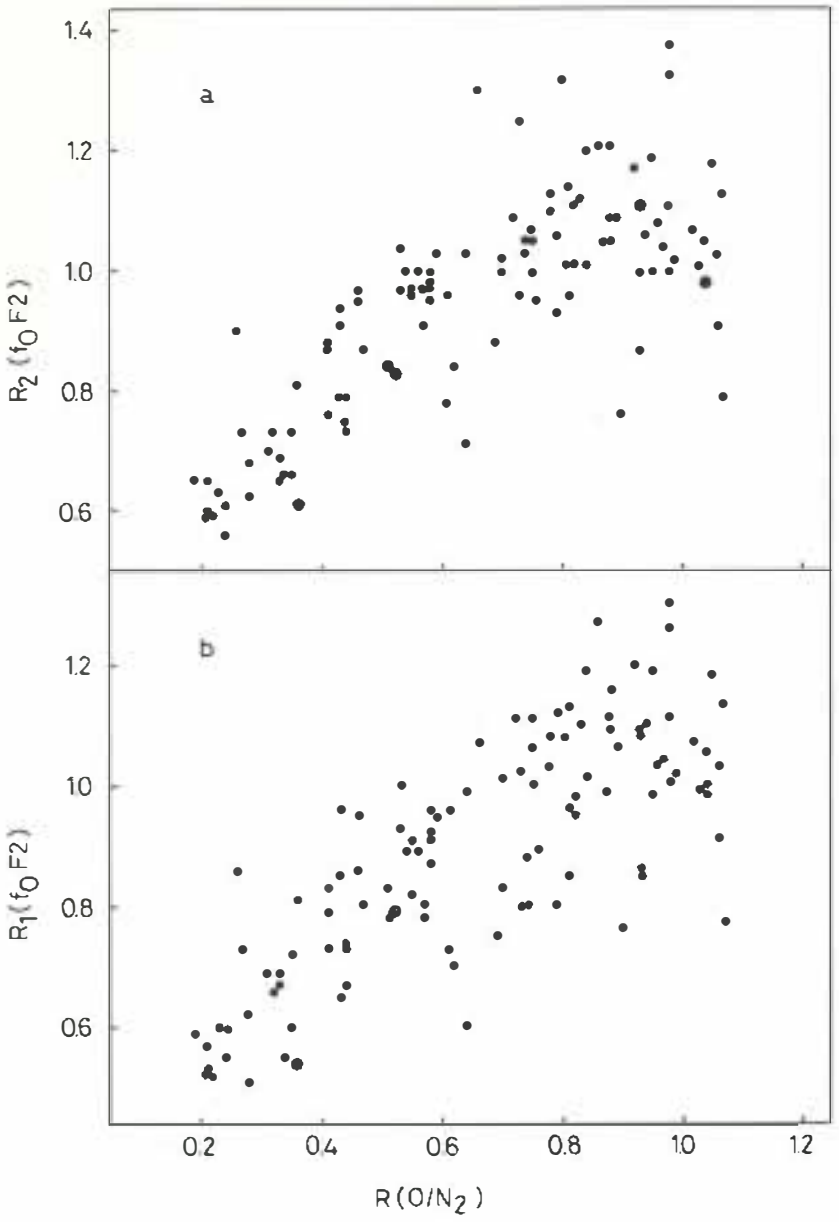

Figure 3. Correlation between changes in the critical frequency of the F_2 layer (f_0F_2) and in the O N_2 ratio:
(a) $R_2(f_0F_2)$ versus R(O N_2) and
(b) $R_1(f_0F_2)$ versus R(● N_2).

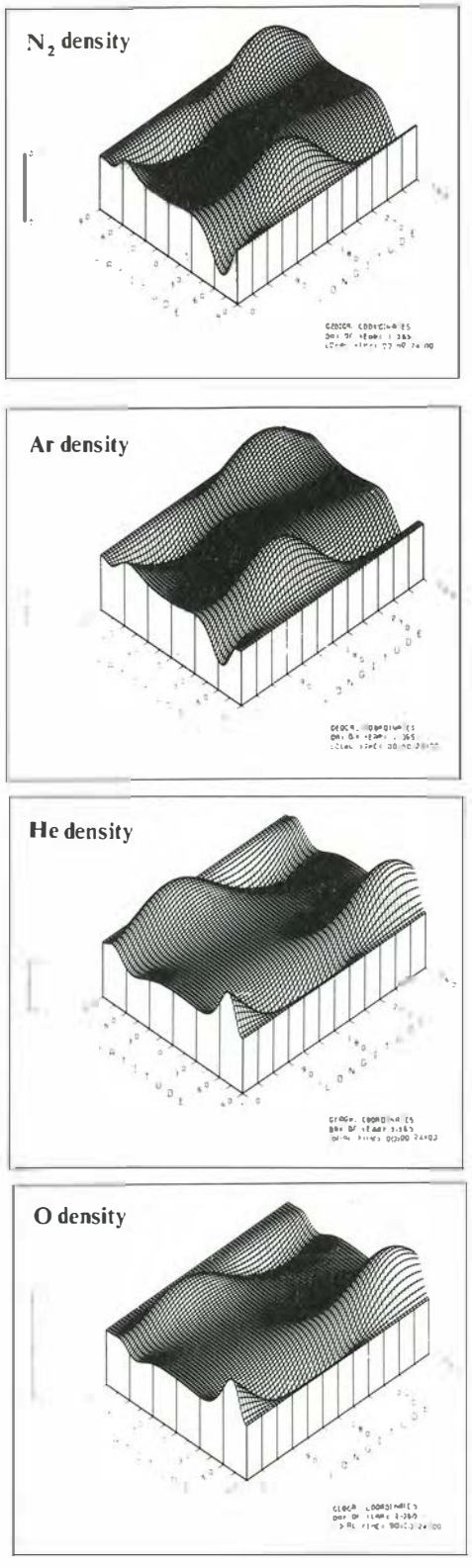

Figure 4. A perspective summary of the longitudinally-dependent neutral gas density model for the four separate components. This is averaged in local time and day of the year. Note the strong anisotropies in polar regions and the anticorrelation between N_2 and Ar and He and O.

link between these two is an indirect one. These observations also highlight the inadequacies of the present magnetic indices, which have neither the spatial nor the temporal resolution needed for ordering ionospheric data.

A second demonstration of the close link between the high-altitude neutral atmosphere and the ionosphere was accidentally discovered during another investigation. It was noticed that there were very few observations of variations of the neutral composition with longitude. Under quiet magnetic conditions they appear to be very stable. Therefore, 228 geomagnetically quiet days were selected covering the whole of the mission and the longitudinal densities were compared with the average longitudinal densities calculated from the empirical model mentioned above. The results are shown in the perspective diagrams in Figure 4. The enhancements of N_2 and Ar densities on the same areas where there is a decrease in He and O are difficult to explain by an increase of exospheric temperature alone, because this would increase all densities. The close correlation between the configuration of the geomagnetic field and the location of extreme N_2, Ar, O and He densities again points to a close connection between the ionosphere and the neutral atmosphere.

Atmospheric ion studies

The ion-mass-spectrometer and Langmuir-probe experiments on ESRO-4 contributed interesting information. The global coverage of ESRO-4 enabled the investigators to make high-quality worldwide measurements over a complete seasonal cycle. Figure 5 shows the global distribution of H^+ ion density at about 750 km altitude for the period between March and September 1973. The rapid fall-off in density above about 50° magnetic latitude is thought to be caused by a continual outflow of ions at the boundaries of the plasmapause and beyond, while the diurnal variations at mid-latitudes can be interpreted in terms of an inflow of H^+ ions at night and an outflow during the day time.

Data from the spherical Langmuir probe were used to derive a model of the electron temperature incorporating the variations due to altitude, latitude and local time. Figure 6 shows electron temperature variations with height and local time extracted from the model. The dawn enhancement is a striking feature of the data, where temperatures greater than at mid-day are reached. This enhancement is concentrated at mid-latitudes and, together with the symmetry of the observations, supports the theory that the pre-dawn start of this rise is due to conjugate photo-electrons arriving

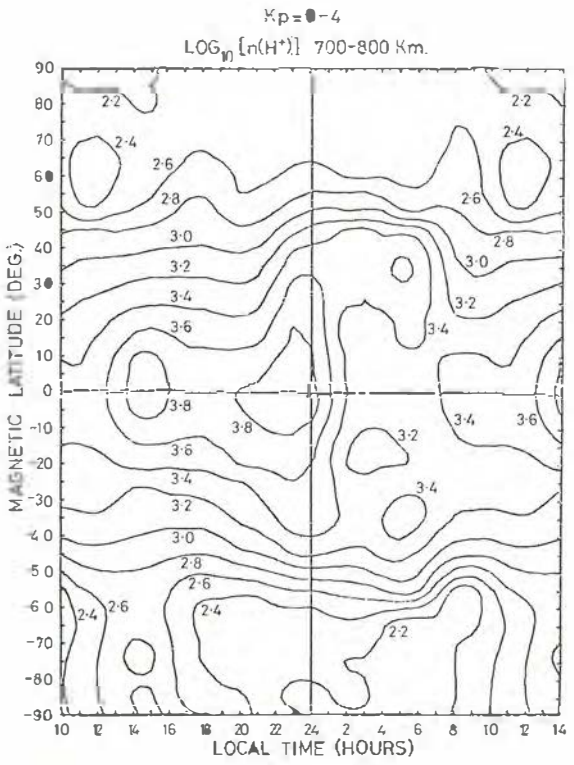

Figure 5. The global distribution of H^+ ion densities at altitudes between 700 and 800 km obtained by averaging data for the period March-September 1973.

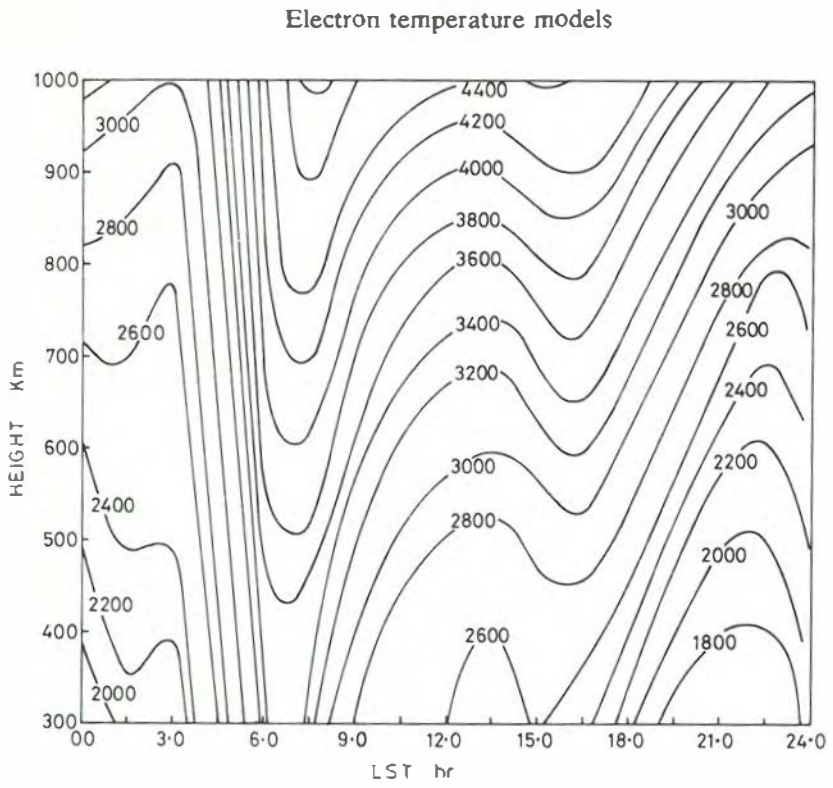

Figure 6. Model electron temperature variations with height and local time at 40°N magnetic latitude. The model used is based on ESRO-4 measurements. Notice the large dawn enhancement.

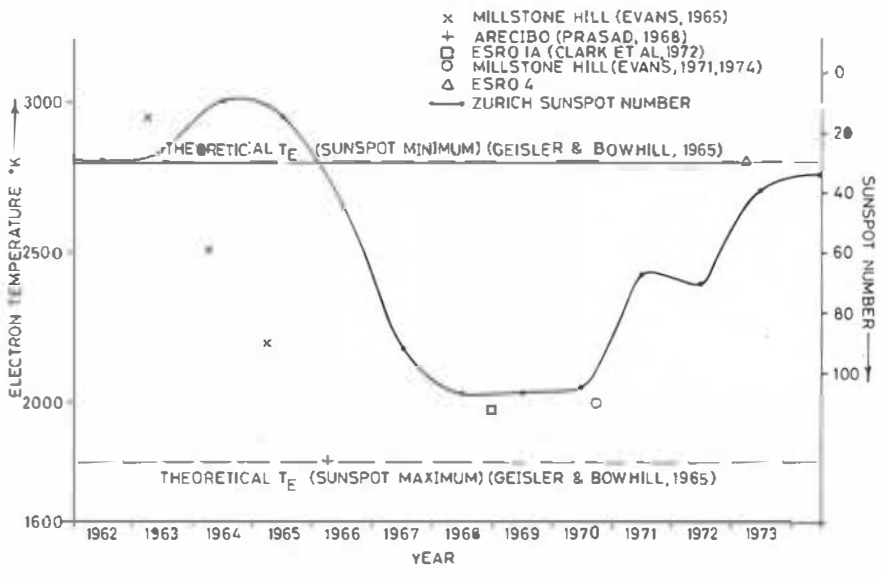

Figure 7. The mean daytime electron temperature at 500 km altitude and 40°N magnetic latitude over the solar cycle 1962-1973 as measured at or near the Spring equinox by a number of experimenters, compared with theoretical predictions of the sun-spot maximum and minimum values. The variation of the Zurich sun-spot number is shown for comparison with an inverted scale.

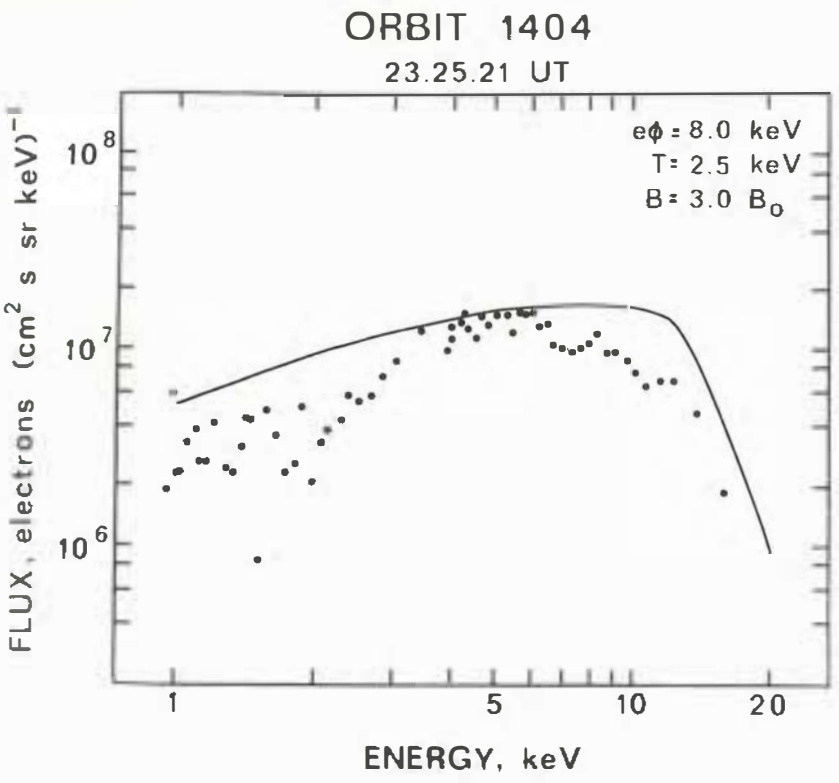

Figure 8. Comparison between the energy spectrum for the locally trapped electrons and the theoretical curve for the inverted-V event. Again there is qualitative agreement.

before local dawn. Other features shown by the model are that the electron temperatures increase with altitude at all latitudes within the region of measurement and with latitude at all altitudes.

The ESRO-4 results complete a solar cycle of electron temperature measurements and fit well with the previous ones, as can be seen in Figure 7. The variations show good inverse correlation with the sun-spot cycle.

Energetic particle studies

One of the more significant results of the particle pitch-angle and energy spectrometer on ESRO-4 is an interesting analysis of a phenomenon called an 'inverted-V' event, which owes its name to its appearance on energy time spectrograms. In these events, strong fluxes of electrons coming down the field line start to increase in energy, reach a peak, then decay again. Because of their association with aurora, these events have aroused considerable interest in the past, and a partial explanation is that the particles are accelerated by electric fields; several of these events were seen by the ESRO-4 instruments. An intriguing feature is the number of low-energy particles coming up the field lines with pitch angles near 90° whilst the acceleration is occurring. These events are normally modelled by starting with an electric field and injecting particles to see what happens. The ESRO-4 investigators, however, began with a flux of particles and applied an electric field. Their calculations showed that immediately the field is applied, the particles with pitch angles near 90° moving up the field line after mirroring do not have enough momentum to get past the electric field and become trapped, and at the same time the increasing electric field accelerates particles coming down the field line and reduces their pitch angle. Hence we get a maximum at a pitch angle of 90°, caused by the trapped particles, with empty pitch angles around it caused by the acceleration. In Figure 8 the energy spectrum predicted for the locally trapped particles is compared with the actual observations to show the good agreement. This is a neat way of explaining how the soft particles mirroring below the field arise and supports the electric field acceleration theories.

For historical reasons, the launch of ESRO-4 was made at solar minimum and there were no solar events during its lifetime. This

removed the main source of measurements from the two solar particle spectrometers which were designed for a more active part of the solar cycle, and the unfortunate death of Leen de Feiter has slowed data analysis from the solid-state telescope. Nevertheless, the two groups have been able to add to information on the trapped radiation. There is, for example, the theory that short-lived energetic protons seen underneath the radiation belt at geomagnetically quiet times are the result of charge exchange between radiation belt protons and exospheric hydrogen. The resultant fast neutral hydrogen particles can cross the field lines and may be stripped at low altitude, reverting to fast protons once more, so forming the source of these anomalous particles. The neutral hydrogen can go up as well as down, and the theory has been tested by looking at interplanetary spacecraft measurements to see whether particles with a similar flux and energy spectra are detected coming apparently from the Earth. Reports presented by Gloeckler and Krimigis at the 14th International Conference of Cosmic Rays contained measurements that seem to confirm the predictions.

Conclusion

This is a quick skim through some of the highlights of the ESRO-4 measurements. Some of the investigations are incomplete; in particular there are loose ends in some of the neutral-particle experiment analyses, as is to be expected from an experiment producing a large amount of new and in some cases unexpected information. The investigators of this experiment are still working hard on the data, now in collaboration with groups from other spacecraft. As the neutral upper atmosphere is the link between the ionosphere and the lower atmosphere, the impact of the ESRO-4 neutral mass spectrometer results on ionospheric physics and perhaps climatology will be considerable.

Cos-B

Cosmic γ-ray astronomy

The aim of the Cos-B mission is to study in detail the sources of extraterrestrial gamma radiation of energy above about 30 MeV. Gamma-ray astronomy is one of several branches of astronomy which can only be conducted from outside the Earth's atmosphere because the latter is transparent only in limited wavelength ranges. In this case an additional difficulty arises from the intense background of high-energy gamma rays which are generated in the atmosphere itself by interactions of incident cosmic rays. Even at the altitudes reached by scientific balloons this background is strong enough to mask all but the brightest sources of extraterrestrial gamma rays.

Scientific mission

High-energy gamma rays are produced in processes characteristic of cosmic-ray interactions and their study has always been promoted as a useful tool for the investigation of the origin of cosmic radiation. This is because gamma rays, being uncharged, travel in straight lines from their points of origin and are not deflected by the interstellar and interplanetary magnetic fields which contort the trajectories of the charged radiation. More recently, the discovery that a large part of the gamma radiation reaching the Earth has its origin within our own galaxy and the recognition of the existence of numerous localised sources have triggered a new interest in the field among astronomers working at other wavelengths, such as radio, infrared and X-ray wavelengths. Correlative studies at the different wavelengths have become a standard approach to investigating the gamma-ray production mechanisms and identifying the source objects.

The orbit

The initial elements of the Cos-B orbit and their values after about three years are given in Table 1. The eccentric orbit was chosen to ensure that for most of the time the satellite would be outside the Earth's radiation belts. (Inside these belts the experiment high-voltage must be switched off to prevent damage to the photo-multipliers due to the incidence of the high charged-particle flux on the counters). The orbital plane is inclined at 90° to the Earth's equator and the argument of perigee placed in the fourth quadrant to ensure that for most of the operational part of the orbit the satellite is in sight of one of the ESTRACK ground stations. This provides for a high data recovery without the use of an on-board tape recorder. Regions of the celestial sphere which are close to the direction of the line of apsides are difficult or impossible to observe due to the entry of the Earth into the field of view or because the Earth-aspect angle is outside the range of operation of the albedo sensors for most of the orbit. The right ascension of the ascending node was so chosen that these regions do not contain any target direction of high scientific interest.

Table 1. Cos-B orbital elements

Epoch		1975 08-09	1978-08-09
Height of perigee	(km)	346	10532
Height of apogee	(km)	99102	88853
Inclination	(deg.)	90.1	96.6
Argument of perigee	(deg.)	334.7	302.2
R.A. of ascending node	(deg.)	43.7	40.3
Period	(day)	1.531	1.529

The experiment

Cos-B carries a single large experiment, the design and provision of which have been the responsibility of a group of research laboratories known as the Caravane Collaboration, whose members are listed in Table 2.

A sectional view of the central detector is shown in Figure 1. It features a 16-gap wire-matrix spark chamber (SC) with magnetic-core readout. Interleaved between the gaps are 12 tungsten plates giving a total thickness of 0.5 radiation length for the conversion of incident photons to electron pairs. The chamber is triggered by a coincidence pulse from a three-element telescope consisting of two plastic scintillation counters (B1, B2) and a directional Cherenkov counter (C). For gamma-ray selection a plastic-scintillator guard counter (A) is placed in anticoincidence to reject triggers due to incident charged particles, but this requirement can be relaxed for calibration measurements using cosmic-ray protons. The triggering telescope defines the field of view of the experiment and elements B2 and C are each divided into four quadrants so that the aperture may be varied by telecommands controlling the event-selection logic. Beneath the telescope is an energy calorimeter, which

Table 2. The Caravane Collaboration

Max-Planck-Institut für Physik und Astrophysik, Institut für Extraterrestrische Physik, Garching-bei-München

Service d'Electronique Physique Centre d'Etudes Nucléaires de Saclay

Cosmic Ray Working Group, Huygens Laboratory, Leiden

Laboratorio di Fisica Cosmica e Tecnologie Relative, Istituto di Scienze Fisiche dell'Università di Milano

Laboratorio di Fisica Cosmica e Tecnologie Relative, Istituto Fisica, Università di Palermo

Space Science Department of ESA, ESTEC, Noordwijk

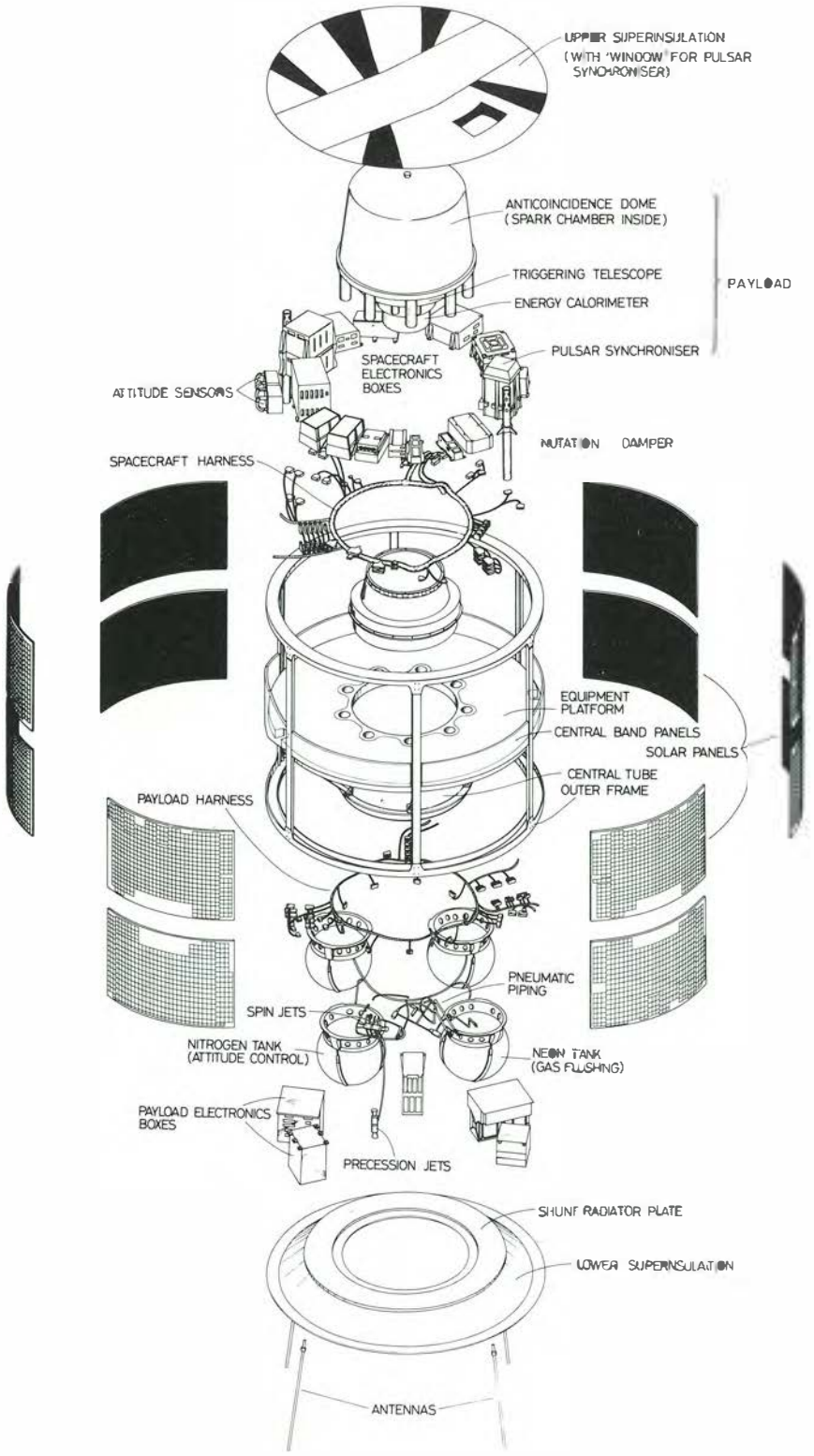
UPPER SUPERINSULATION
(WITH 'WINDOW' FOR PULSAR SYNCHRONISER)
ANTICOINCIDENCE DOME
(SPARK CHAMBER INSIDE)
TRIGGERING TELESCOPE
ENERGY CALORIMETER
PULSAR SYNCHRONISER
PAYLOAD
SPACECRAFT ELECTRONICS BOXES
ATTITUDE SENSORS
NUTATION DAMPER
SPACECRAFT HARNESS
EQUIPMENT PLATFORM
CENTRAL BAND PANELS
SOLAR PANELS
CENTRAL TUBE OUTER FRAME
PAYLOAD HARNESS
PNEUMATIC PIPING
SPIN JETS
NITROGEN TANK (ATTITUDE CONTROL)
NEON TANK (GAS FLUSHING)
PAYLOAD ELECTRONICS BOXES
PRECESSION JETS
SHUNT RADIATOR PLATE
LOWER SUPERINSULATION
ANTENNAS

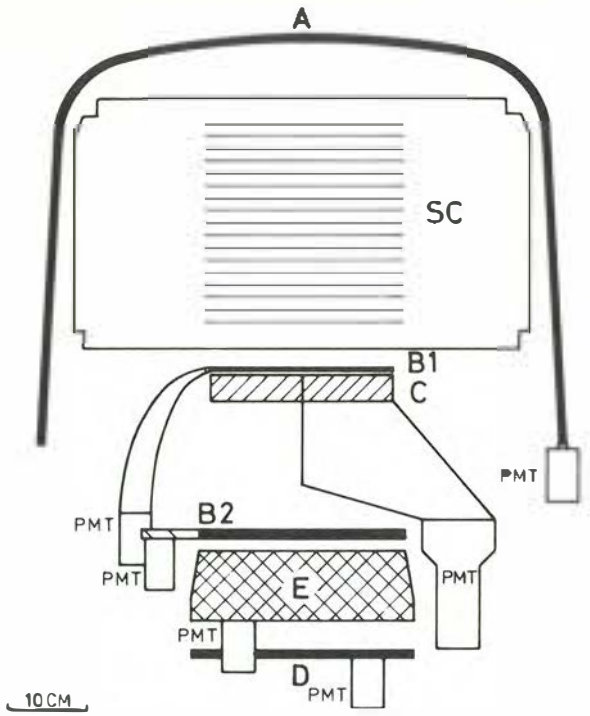

Figure 1. Sectional view of Cos-B experiment.

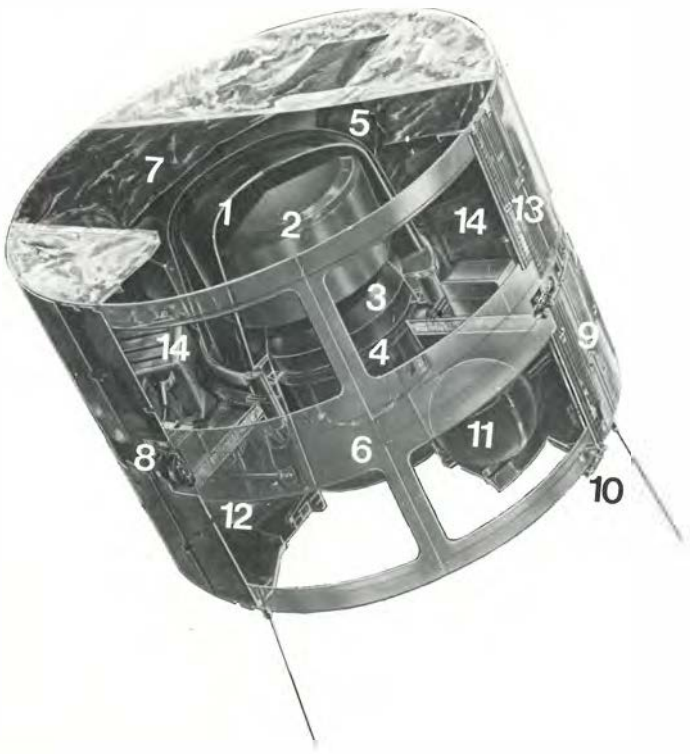

consists of a caesium-iodide scintillator (E) to absorb the secondary particles produced by the incident photons and a plastic scintillator (D) to provide information on high-energy events for which this absorption is incomplete.

Alongside this instrument is mounted a proportional counter, sensitive to X rays in the energy range 2-12 keV, to provide synchronisation for possible short-period pulsations of gamma-ray emission from sources known to pulsate at X-ray wavelengths. The inclusion of an in-flight calibration system for this counter and a modification to increase the uniformity of its directional response have also enabled it to be used for monitoring the intensity of radiation from X-ray sources.

The measurement characteristics of the gamma-ray detector were determined before launch by exposing the instrument to gamma-ray and charged-particle beams at particle accelerators. Both the engineering model and the flight model were calibrated in tagged photon beams with energies between 20 MeV and 6 GeV at DESY, Hamburg. The effect of background generation by the charged-particle environment in orbit was investigated with the aid of proton beams at CERN, Geneva, and electron beams at DESY. The conclusion drawn from these measurements was that Cos-B could measure the arrival directions and energies of cosmic gamma-rays ranging in energy from 30 MeV to at least 4 GeV more accurately than was possible with any previously flown experiment. The results of in-flight measurements have confirmed this conclusion.

The spacecraft

Cos-B is configured as a cylinder 1400 mm in diameter and 1130 mm long, the main experiment package occupying the central region (Fig. 2). The pulsar synchroniser is mounted on the

Figure 2. Cutaway view of Cos-B.

1. Anticoincidence counter
2. Spark chamber
3. Triggering telescope
4. Energy calorimeter
5. Pulsar synchroniser
6. Structure
7. Superinsulation
8. Sun and Earth-albedo sensors (attitude measurement)
9. Spin thruster
10. Precession thruster (attitude control)
11. Nitrogen tank (attitude control)
12. Neon tank (spark chamber gas flushing)
13. Solar-cell array
14. Electronics

Table 3. Cos-B Observation Programme

Period	Orbit	Date	Target	Equatorial co-ordinates (1950.0) RA hr	RA mn	Dec. deg.	Galactic co-ordinates l^{II} deg.	b^{II} deg.
A	6	1975-08-17	PSR 0531+21	5	29	+22.3	184.0	− 6.1
B	26	09-17	GX5-1	17	54	−24.5	5.2	− 0.0
C_1	48	10-20	PSR 0833−45	8	31	−45.3	263.5	− 3.3
C_2	60	11-08	3U0900−40	8	57	−40.4	262.7	+ 3.5
D	73	11-28	Cygnus	20	15	+35.7	73.9	+ 0.3
E	90	12-24	Cen X-3	11	15	−60.3	291.6	+ 0.2
F	110	1976-01-23	Cen A	13	16	−43.6	308.2	+18.8
G	130	02-23	Cir X-1	15	12	−57.1	321.5	+ 0.3
H	150	03-24	3U1832−05	18	30	− 5.8	25.7	+ 1.5
I	170	04-24		19	19	+ 9.7	44.9	− 2.1
J	190	05-24	Virgo	12	21	+ 7.1	283.9	+68.7
K	210	06-24	3U0115+63	1	14	+63.6	125.8	+ 1.1
L	230	07-24	3U0900−40	8	56	−40.5	262.5	+ 3.2
M	250	08-21	Ophiucus	16	50	−30.5	352.1	+ 8.5
N	274	09-30	CG 195+4	6	31	+17.7	195.3	+ 4.3
O	295	11-02	SMC X-1	1	10	−73.6	301.0	−43.7
P	320	12-10	3U2208+54	22	8	+54.7	101.0	− 0.9
Q	345	1977-01-17	3C129	4	25	+48.6	155.4	+ 0.0
R	370	02-24	GX5-1	17	58	−25.0	5.2	− 1.0
S	377	03-07		7	1	− 5.8	219.5	− 0.0
T	402	04-14	3U0946−30	9	40	−28.1	260.1	+18.4
U	414	05-02	PSR 0740−28	7	40	−27.8	243.3	− 2.4
V	438	06-08	Cyg X-3	20	46	+44.0	84.1	+ 0.5
W	462	07-15	Corvus	12	40	−17.7	299.9	+44.9
X	484	08-18	PSR 1747−46	17	22	−43.7	345.3	− 4.5
Y	508	09-23	Aquila	18	52	+ 2.2	35.3	+ 0.3
Z	533	11-01		19	42	+23.8	60.0	+ 0.1
27	557	12-07	NGC4151 Coma	12	31	+33.5	154.0	+82.8
28	581	197801-13		3	10	+57.8	140.9	+ 0.1
29	607	02-22	MCG 8-11-11	5	26	+44.4	165.2	+ 5.6
30	631	03-30		19	58	−41.7	359.2	−30.1
31	653	05-03	PSR 0950+08	9	51	+ 8.8	229.1	+44.0
32	677	06-09	3C273	12	26	+ 2.4	289.5	+64.4
33	702	07-17		13	49	−61.4	310.2	+ 0.4
34	726	08-23	Orion	5	32	− 5.8	209.2	−19.8
35	750	09-29	3C390.3	18	42	+79.9	111.6	+27.2
36	773	11-03	Pelican	20	48	+44.5	84.7	+ 0.5
37	798	12-11	M31	0	24	+42.3	118.1	−20.1

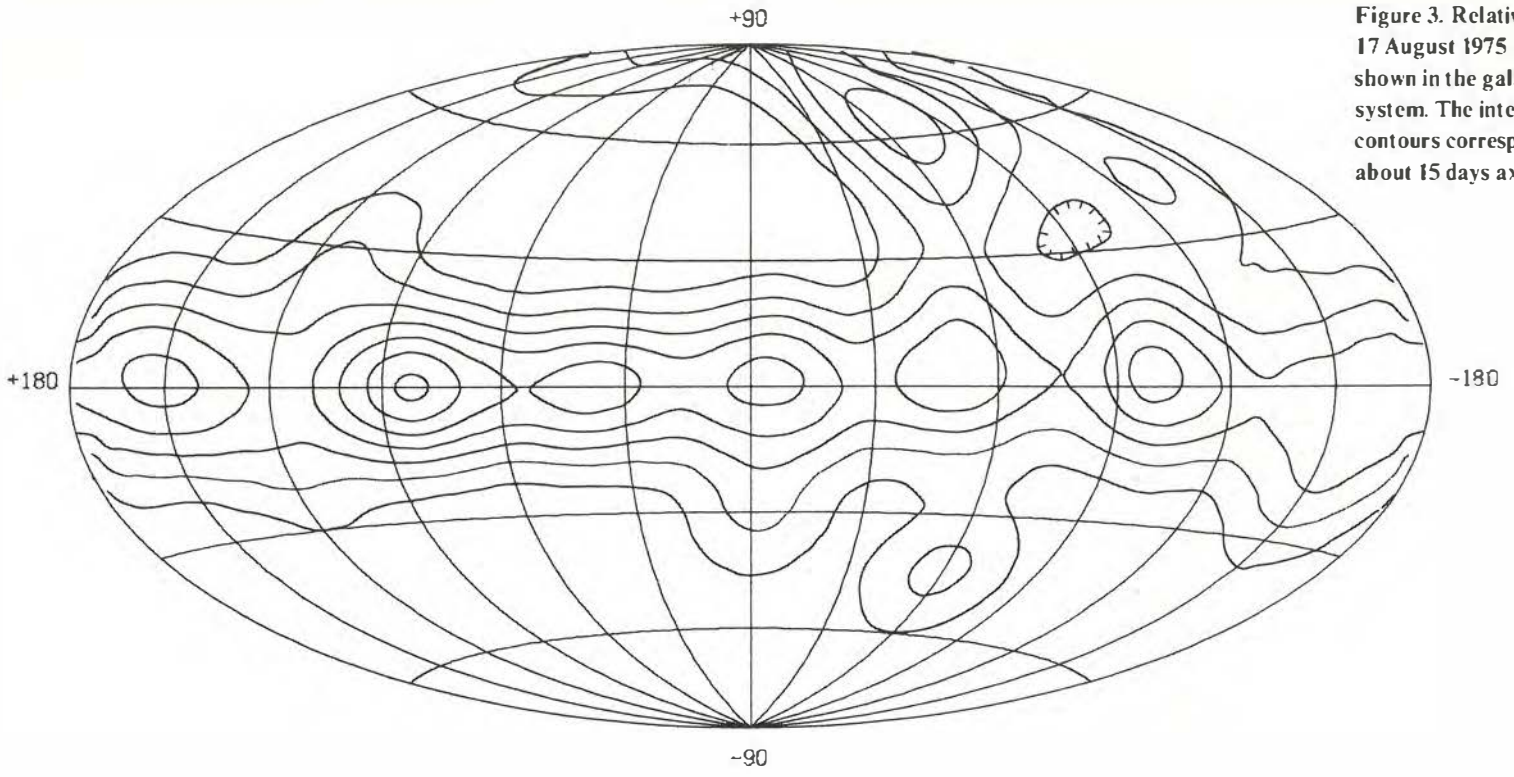

Figure 3. Relative sky coverage between 17 August 1975 and 31 December 1978, shown in the galactic co-ordinate system. The intervals between the contours correspond to the equivalent of about 15 days axial exposure.

equatorial equipment platform with its optical axis parallel to that of the main experiment. All experiment electronics units and spacecraft subsystems are mounted on the upper or lower surface of this platform in order to minimise the amount of material in the field of view and to reduce the probability of the experiment's being triggered by background-induced charged-particle interactions in these units. The total mass at launch was 278 kg of which 118 kg was contributed by the experiment units.

The satellite is spin-stabilised at ca. 10 rpm about its axis of symmetry, which coincides with the optical axis of the gamma-ray detector. A simple nitrogen-gas attitude-control system is used to point the experiment in the desired direction. Sun and Earth sensors are used for attitude measurements from which the pointing direction can be reconstituted with a precision of 0.5°.

Performance in orbit

Observation programme

Cos-B was launched from Western Test Range by a Thor-Delta vehicle on 9 August 1975. After a short period devoted to checking out the systems, routine operations began on 17 August when the satellite was directed towards its first target. Since then Cos-B has made a comprehensive scan of the part of the sky along the plane of the Milky Way. This was done in a series of one-month observations, each covering a circular field of about 25° radius. In some regions of particular interest observations have been repeated or overlapped. In addition, about a quarter of the time has been devoted to observations at higher galactic latitudes, especially in regions containing specific objects of general interest, such as radio pulsars, quasars and Seyfert galaxies. The programme executed up to the end of 1978 is summarised in Table 3 and the sky coverage achieved is shown in Figure 3. Scheduling of observations is constrained by limitations on solar-aspect angle, attitude-sensor coverage and entry of the Earth into the field of view, but takes account of scientific priorities and, where possible, the known plans of other satellite, balloon or ground-based astronomy experiments.

Experiment operations

Initially, the experiment high voltage was switched on for about 30 hours in each 37-hour orbit. (This had to be reduced to 25 hours after the closure of the Fairbanks tracking station – see Data

acquisition and processing). During alternate orbits about 45 minutes is devoted to calibration of the detectors. For this purpose, use is made either of cosmic-ray protons by relaxing the anti-coincidence requirement in the event-selection logic or of an In-Flight-Test system with electronic stimulation and light-emitting diodes. Every fourth orbit a calibration of the pulsar synchroniser is made using an ^{241}Am-Sr target source. The frequencies of all these calibrations are reduced by a factor of two relative to their initial values in the light of the demonstrated stability of the gamma-ray and X-ray detectors performance.

For gamma-ray measurements the experiment event-selection logic is operated in the 'narrow-angle' mode, i.e. triggers are accepted only if a coincidence is registered between one quarter of the C counter and the corresponding quarter of the B2 counter. This mode was found during the pre-launch investigations to provide a reduced probability of triggering on locally-induced background without seriously restricting the efficiency for recording good gamma rays. Although many background triggers are still registered, their rate is not so high that the time taken to transmit them will significantly reduce the observation time. Genuine gamma-ray events are separated from the background during the analysis of the data.

The mission was originally foreseen to last 2 years, but was extended because of the great importance of the scientific results being achieved. Continued satisfactory operation of the spark chamber over this long period was made possible by equipping the satellite with a gas-flushing system for emptying and refilling the spark chamber. This has been used to forestall progressive deterioration of performance due to poisoning of the gas. As the rate of deterioration has decreased with time, it has proved possible to increase the interval between flushings from its initial value of 6 weeks to about 14 weeks. At the end of 1978 only about 70% of the original supply of gas had been used.

Data acquisition and processing

Experience has shown that the satellite telemetry system can be operated at the maximum bit rate of 320 bps without significant loss of data quality. During the part of the orbit when the experiment is switched on, data are recovered by one of the ESTRACK ground stations at Redu (Belgium) and (until August 1977) Fairbanks (Alaska). All data are recorded in the ground station on digital magnetic tapes which are despatched at regular intervals to the Operations Centre (ESOC) in Darmstadt (Germany) where they form the basis of the final data processing. In addition, data recorded at Redu can be transmitted directly to ESOC, either in real time or, by playing back the digital tape, at the end of a pass. Real-time data are used for monitoring the correct functioning of spacecraft and experiment subsystems, especially during telecommanding operations.

From the data transmitted 'post-pass' to ESOC a sample, equivalent on average to about 30% of all data acquired, is made available to the experimenters' 'Fast Routine Facility'. In this facility the scientific collaboration has set up a suite of programs for the complete scientific analysis of these data, using predicted orbit and attitude information provided by ESOC. This permits a thorough check on the scientific as well as the technical performance of the various experiment units, providing where necessary the possibility of a fast feedback to keep the equipment in the optimum operational mode. In addition preliminary scientific conclusions can be reached, which can be taken into account in planning the future observation programme and in establishing priorities for the analysis of the final processed data. Such preliminary conclusions have been published in IAU circulars when it has been considered useful to alert other investigators to the possibility of correlative observations.

Achievements

Gamma-ray study

Large-scale galactic emission

Data from 11 of the observations listed in Table 3 have been used to study the spatial and energy distributions of gamma radiation from the Galaxy. Representative latitude profiles for 10 longitude regions are shown in Figure 4. The narrow profiles observed in the range $305° < l^{II} < 40°$ are consistent with that expected from the superposition of near-Gaussian distributions of different widths, corresponding to the varying angular resolution of the experiment over the wide range of energies. Selection of higher-energy photons has made it possible to place an upper limit of about 2° on the width of the emitting region in these central parts of the Galaxy. At greater angular separations from the galactic centre the emission intensity profile becomes broader (and weaker) and in the anticentre region (after subtracting the contributions from the two

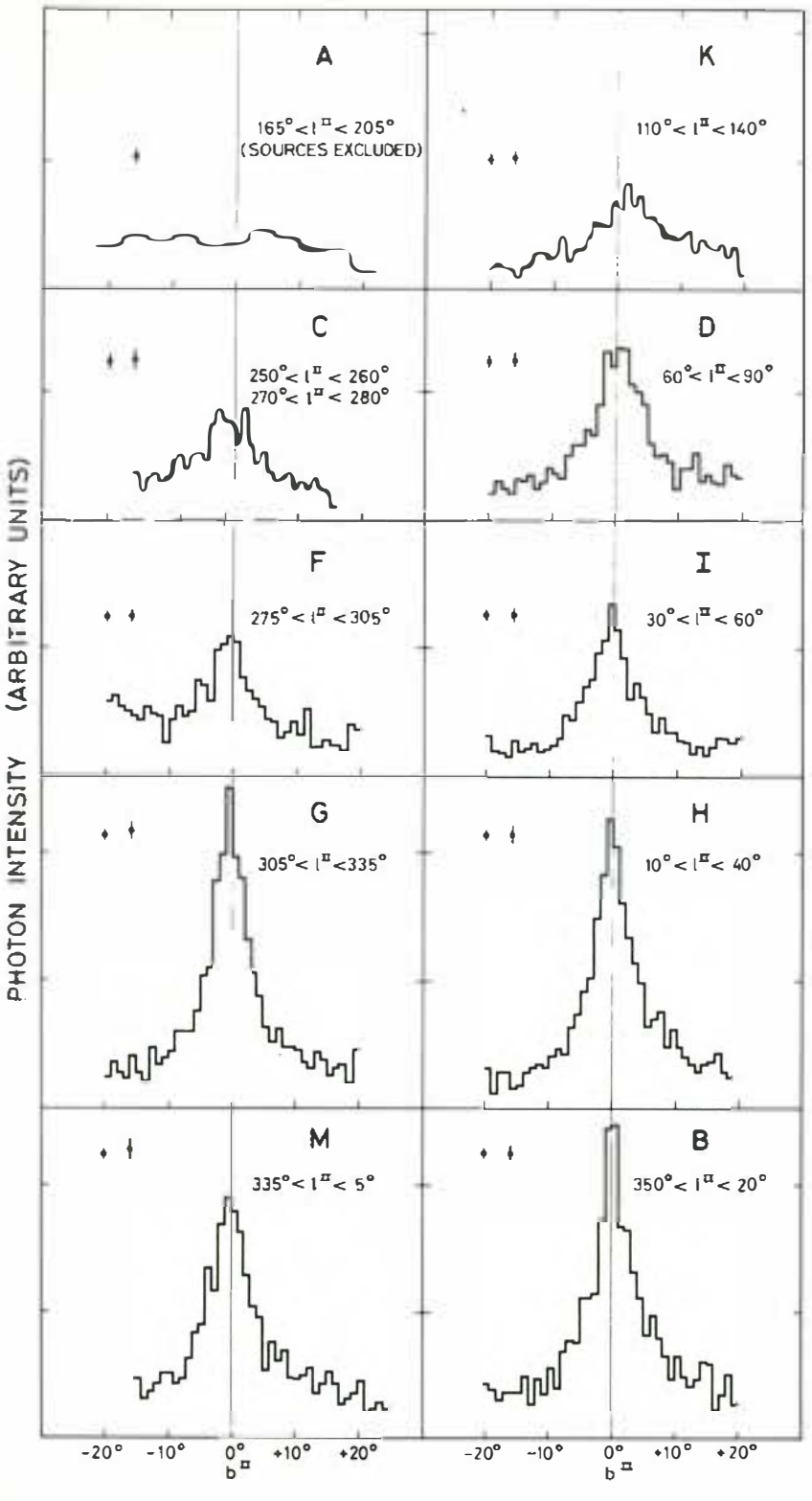

Figure 4. Latitude profiles of the intensity of gamma-rays of energy >100 MeV, averaged over the longitude intervals indicated. Typical statistical errors are for the values in the wings (left) and the peak (right).

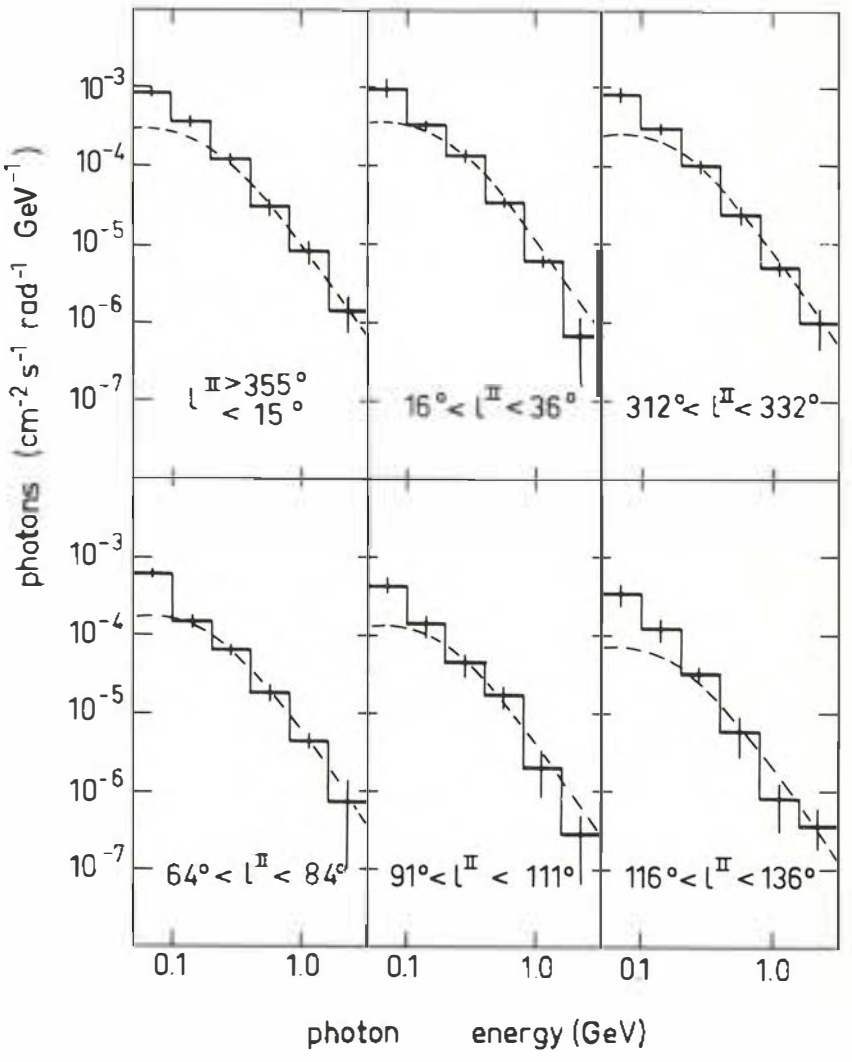

Figure 5. Energy spectra of the gamma radiation from 6 regions of the galactic disc. The error bars represent both statistical uncertainties and fluctuation of the background. The dashed lines indicate the expected spectral shape due to π^0 decay.

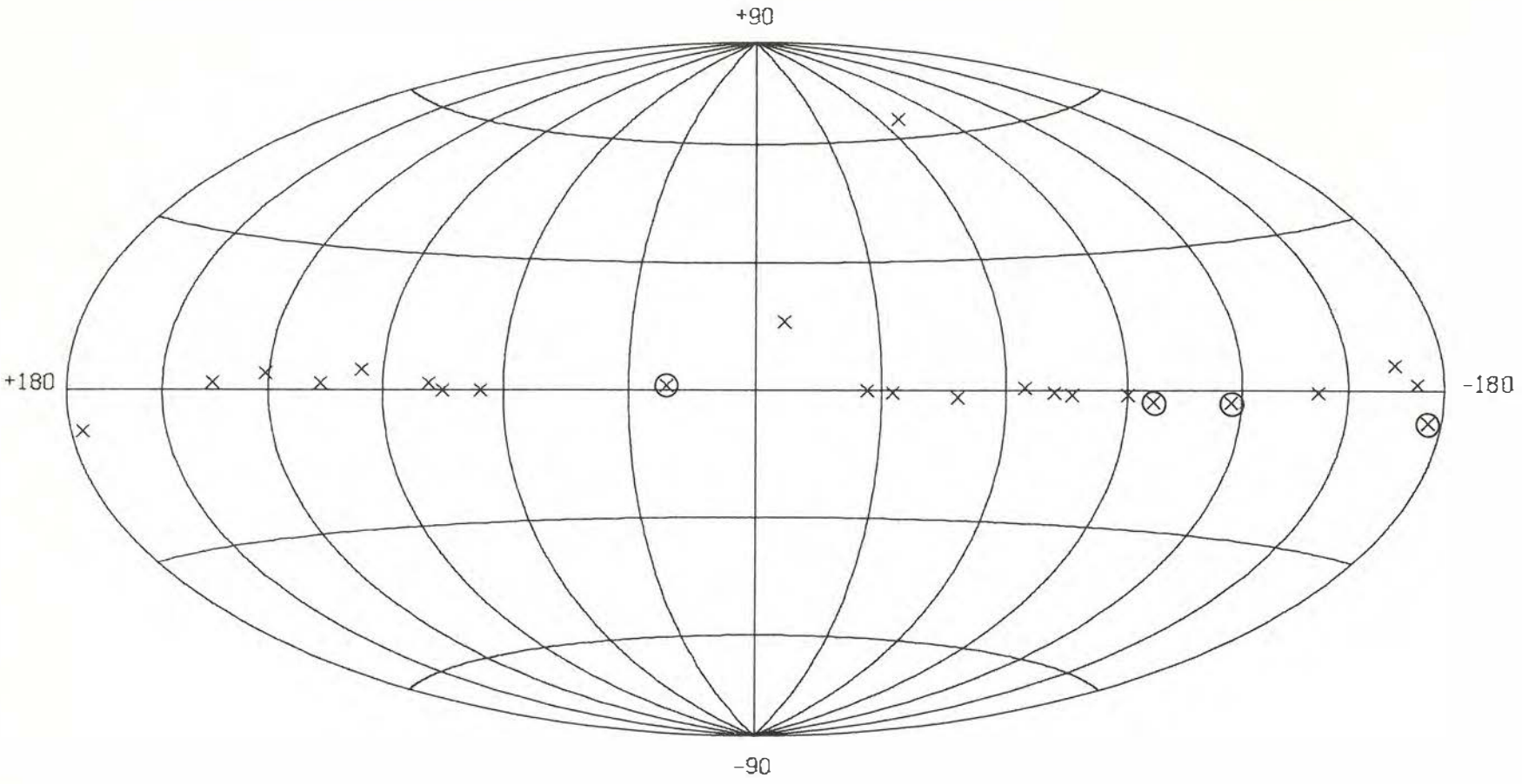

Figure 6. Positions of the gamma-ray sources detected by Cos-B, shown in the galactic co-ordinate system. The four pulsars are circled.

well-established localised sources) there is little evidence for any emission from the galactic disc. The variation of the intensity with longitude is in good agreement with the familiar picture derived from the results of the American SAS-2 satellite, but the better angular resolution of Cos-B has highlighted many regions of intense localised emission, which are discussed below.

From six observations, covering half the range of longitudes, it has been possible to derive the energy spectrum of the galactic radiation. Figure 5 shows that the shape of the spectrum does not vary significantly with longitude. The interpretation of this spectrum is of great astrophysical significance. Its inconsistency with the classical spectrum due to π° decay indicates that, in addition to the expected production in collisions of cosmic-ray protons with interstellar matter, there must be a significant contribution from radiation processes of the electron component of the cosmic radiation.

Localised gamma-ray sources

A detailed study of the data revealed the existence of 24 point-like gamma-ray sources. Four of them were readily identified with radio pulsars and are further discussed below. Most of the others could not be easily identified with objects radiating at other wavelengths and only one of them had previously been reported. These sources are concentrated toward the galactic equator (see Figure 6) suggesting that most of them have a galactic nature with

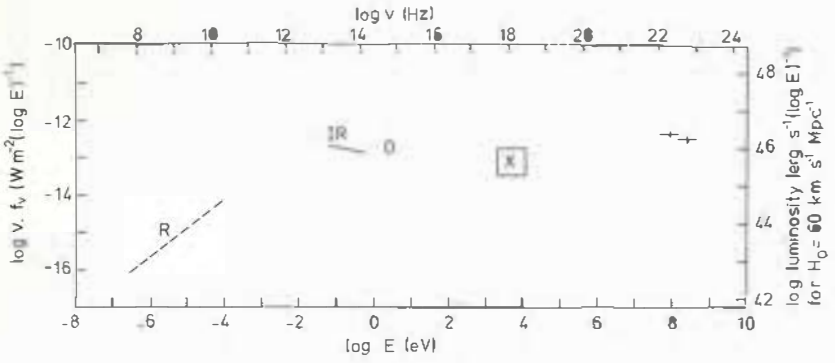

Figure 7. Spectrum of 3C273 from radio to gamma-ray energies. The intensity scale is given in units of power per decade.

typical distances in excess of 1 kpc. It has been proposed that such sources may make a significant contribution to the total gamma-ray luminosity of the Galaxy.

Figure 8. Smoothed contour map of the intensity of gamma radiation in the Cygnus region, showing the locations of three localised sources.

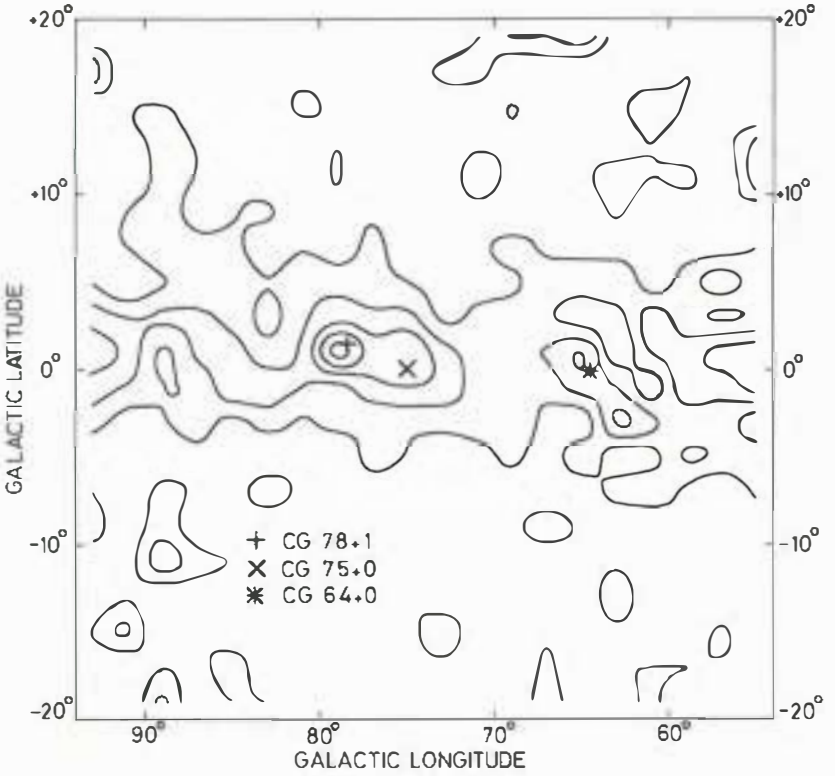

The only source found at a high galactic latitude ($|b^{II}| > 20°$) has been identified with an object outside our own galaxy. This is the quasar 3C273, which is seen to have a luminosity in gamma rays comparable with that at other wavelengths (Fig. 7). The discovery lends support to a suggestion that one of the other Cos-B sources (known as CG 135 + 1) may also be identified with a quasar. An object of this type was recently discovered by radio and optical astronomers following a precise measurement by SAS-3 of the position of the nearest known X-ray source to CG 135+1. Whether or not this identification is confirmed (other candidates have been proposed), there is no doubt that the discovery of this new quasar (the nearest one known at the present time) has been a direct consequence of the Cos-B measurement.

Figure 8 is a contour map of gamma-ray intensity in the Cygnus region showing the location of 3 of the Cos-B sources. In this region the SAS-2 satellite detected gamma-rays exhibiting a 4.8 hr periodicity from the X-ray source Cyg X-3. Although no localised enhancement was detected by Cos-B at a position consistent with Cyg X-3 a search of the data from around that source was made for an indication of the periodicity. The result of this search was completely negative, indicating that at the time of the Cos-B observation (December 1975) Cyg X-3 did not emit gamma-rays with its 1973 intensity, as reported by the SAS-2 group.

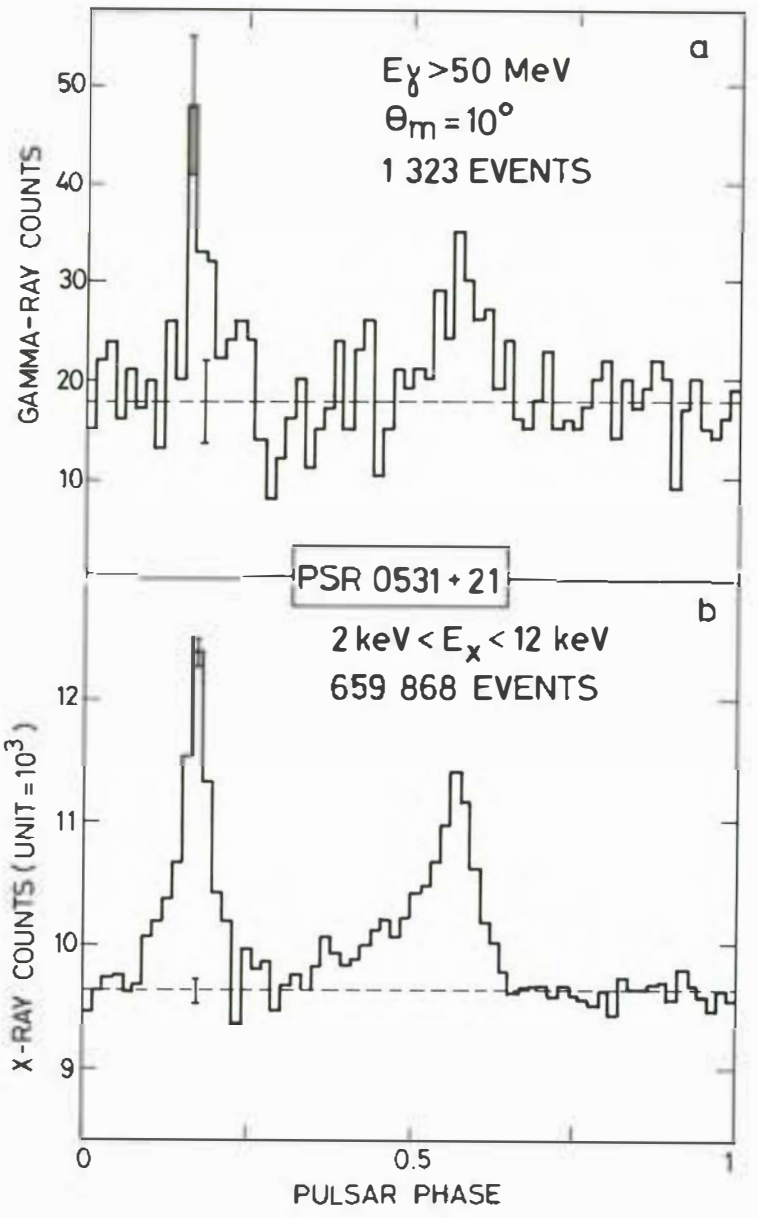

Figure 9. Gamma-ray (a) and X-ray (b) light curves of PSR 0531 + 21 integrated over periods of one month and 1.5 d respectively. The pulsar phase is divided into 66 bins. The broken lines indicate the average numbers of counts per bin excluding those bins containing the pulses and the region between the pulses.

Gamma-ray pulsars

The two well-established gamma-ray pulsars, PSR 0531 + 21 (Crab) and PSR 0833 − 45 (Vela), have each been studied by Cos-B during two observations. Using the accurate timing information of the on-board clock it was possible to investigate the time structures of the radiation from the two pulsars and their relationships to the known radio-pulsar light curves. To eliminate Doppler effects due to the motions of the satellite around the Earth and of the Earth around the Sun, the individual gamma-ray arrival times in the satellite reference frame were transformed to the solar-system barycentre. The barycentre arrival times were folded with the period of the pulsars, using values of the period and period derivatives determined from radio observations.

Figure 9 shows the gamma-ray light curve of PSR 0531 + 21 for energies above 50 MeV, derived by selecting photons incident within 10° of the pulsar direction. For comparison the light curve of 2-12 keV X-rays, derived by applying the same procedure to the data from the pulsar synchroniser, is also shown. There is a strong similarity between the curves, both showing two peaks separated by 0.4 of the 33 ms pulsar period.

PSR 0833 − 45 does not emit a measurable flux of X-rays but is the brightest object in the gamma-ray sky. It has a gamma-ray light curve similar to that of PSR 0531 + 21 with two peaks of widths ~3 ms and ~5 ms (Fig. 10). It has recently been possible to establish the exact phase relationship between the gamma-ray pulses and those at radio (and hence also at optical) wavelengths. In collaboration with the Radiophysics Division of the Australian Commonwealth Scientific and Industrial Research Organisation

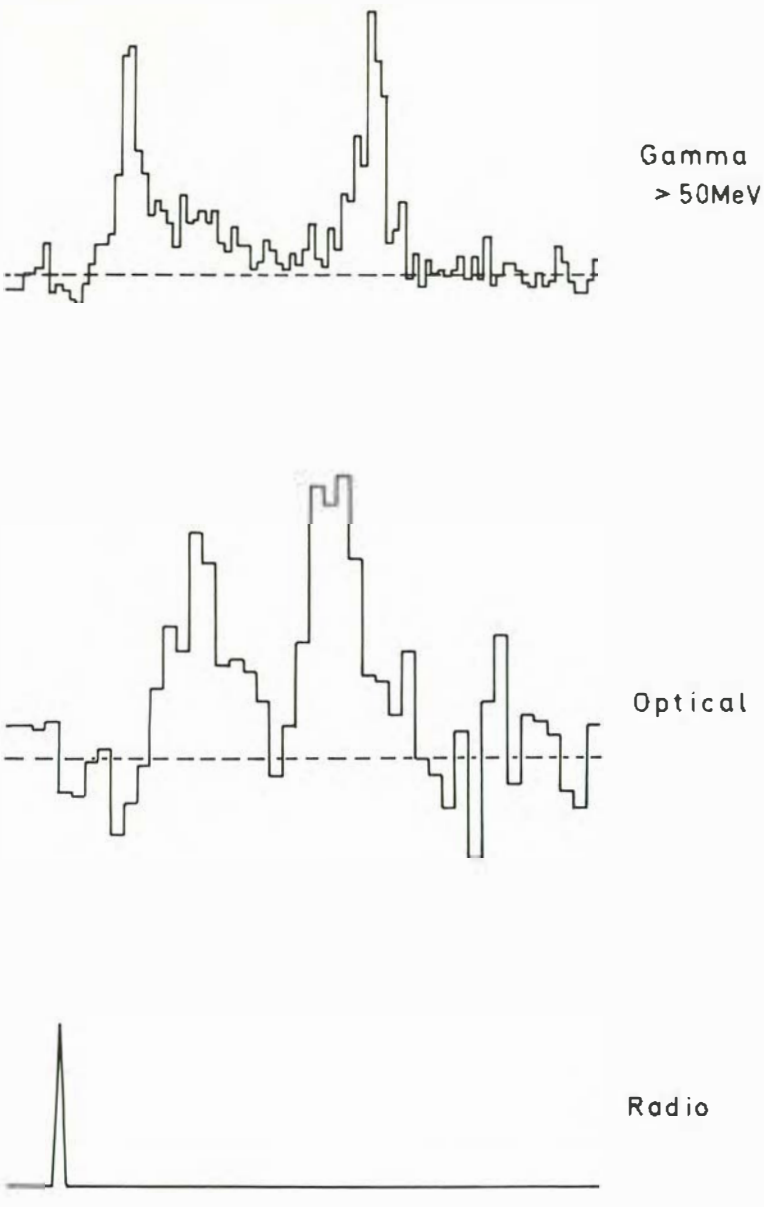

Figure 10. Comparison of light curves of the Vela pulsar (PSR 0833 – 45) as measured at gamma-ray, optical and radio wavelengths (data from Cos-B, The Anglo-Australian Telescope and CSIRO/NASA Tidbinbilla). The abcissa represents 89 ms full scale.

(CSIRO), the absolute times of the pulse peaks at the solar-system barycentre have been compared with those of the radio pulse, derived from measurements at the NASA Deep Space Station, Tidbinbilla. The comparison is shown in Figure 10, together with the optical profile obtained from observations made with the Anglo-Australian Telescope. The striking differences will play an important part in the interpretation of these curves in terms of models of the emission processes for the different types of radiation.

For both pulsars, the separation between the peaks is 0.4 ± 0.03 of the period (33 ms and 89 ms respectively). Most of the gamma radiation is emitted within these narrow peaks – at least 78% in the case of PSR 0531 + 21 and at least 91% in the case of PSR 0833 – 45. Cos-B has provided the first measurements of the energy spectra of the pulsed radiation from these pulsars to extend over the range 50 MeV to 4 GeV, shown in Figures 11 and 12. That for PSR 0531 + 21 can be represented by a single power law which is also consistent with other measurements down to 100 keV. The spectrum of PSR 0833 – 45 is not easily fitted by a single power law, its slope decreasing below about 500 MeV.

A logical follow-up to these results has been to search for evidence of pulsed gamma-ray emission from the known radio pulsars. Because of the low rate of accumulation of gamma-ray events it is necessary to fold the data from a whole month's observation with periods of the order of ms. Accurate knowledge is therefore required, not only of the pulsar period P but also of its derivative $\dot{P}$. Although published data are available for some 150 of the 300 known radio pulsars, most of these require extrapolations of up to 5 years to the epoch of the Cos-B observations. In only a fraction of

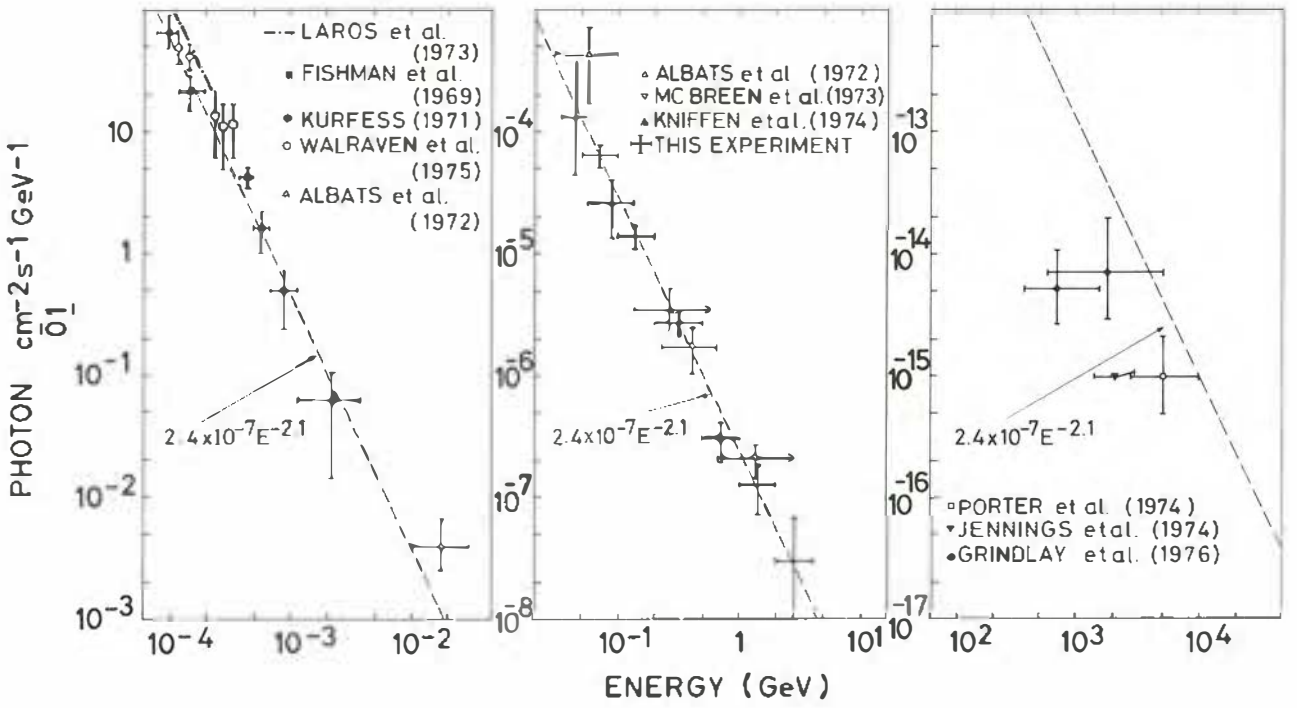

Figure 11. The differential energy spectrum for the pulsed emission from PSR 0531 + 21 from 100 keV to 10 TeV. The broken line is the fit derived from the Cos-B data points.

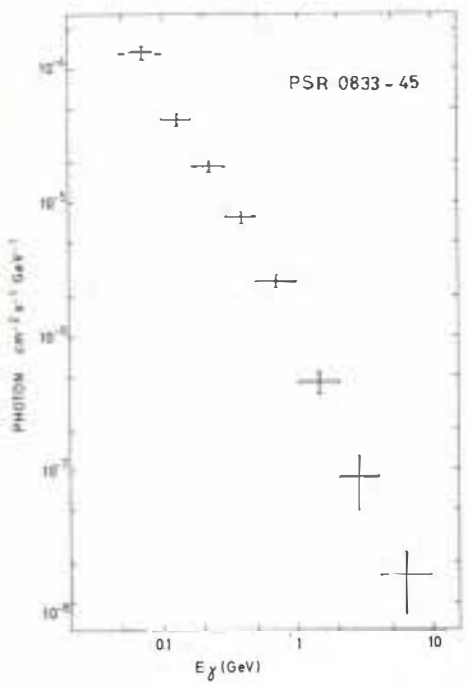

Figure 12. The differential energy spectrum of the pulsed component of the gamma radiation from PSR 0833– 45. Statistical errors are indicated.

the cases is the extrapolated uncertainty in the parameters so small that the light curve will not be smeared out. A study of 32 such pulsars which had been within the field of view of Cos-B yielded none for which there was any indication of pulsed emission above the 2 σ level of confidence.

For other pulsars a scanning of P and $\dot{P}$ within the extrapolated uncertainties has to be performed. The additional degrees of freedom so introduced require that a very critical examination be made of any positive indications. The measured properties of PSR 0531 + 21 and PSR 0833 –45 were used to estimate the gamma-ray energy which might be released by other radio pulsars. In a list of 15 which are considered to be the most promising candidates for observation by Cos-B there are several for which data are already available. At the time of writing positive results have been obtained in two cases – PSR 0740 – 28 and PSR 1822 – 09. The gamma-ray light curves of these two pulsars are shown in Figure 13. It is immediately evident that all four show the same general shape with two peaks separated by 0.4 of the period, although the periods themselves range over a factor of more than 20. However the pulsars have different gamma-ray energy spectra, as is indicated by the energy ranges for which the curves in Figure 13 have been

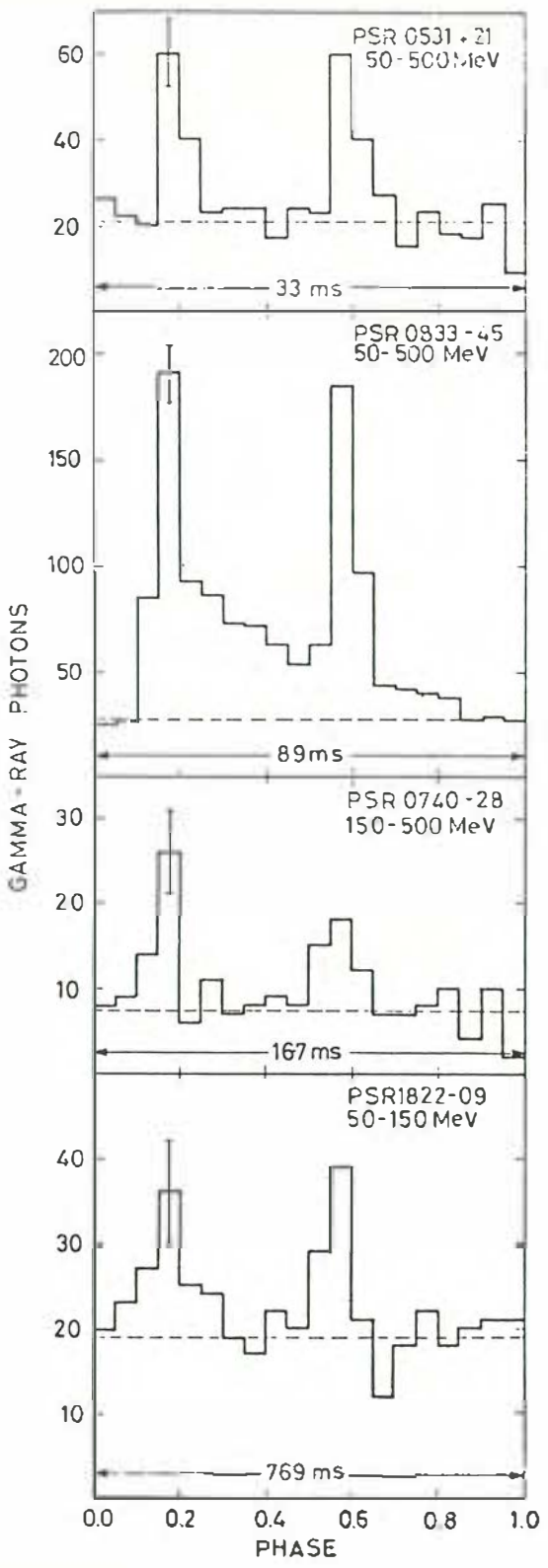

Figure 13. Light curves of the four gamma-ray pulsars detected by Cos-B in the photon-energy ranges indicated. The period of each pulsar is shown.

derived. PSR 0531 +21 and PSR 0833 −45 are the two youngest pulsars known and are still losing rotational energy at a relatively high rate. The detection of gamma radiation from two older pulsars (both with ages greater than 10^5 yr or 100 times that of PSR 0531 +21) indicates that they are much more efficient in converting their energy loss to gamma rays.

As a result of the publicity given to these investigations a number of radio observatories have started new programmes of pulsar observations. These will yield contemporary parameters which will be of great value for the analysis of Cos-B data acquired during the continuing mission and will permit interpolation to provide more accurate data for use with earlier results.

X-ray study

Although the gamma-ray experiment has a wide field of view, during several observation periods the axis of the experiment has been pointed to a specific object in order to ensure that it is within the more restricted field of view of the pulsar synchroniser. Several other strong X-ray sources have at some time been near enough to the pointing direction to permit a study of the behaviour of their X-ray emission continuously (apart from periods of passage through the radiation belts) over periods of a month. The periodic behaviours of Cyg X-1, Cyg X-3, Vel X-1, Cen X-3 and Cir X-1 have all been studied.

Cos-B observed the Cygnus region in November/December 1975 and again in June/July 1977. During the first of these periods Cyg X-1 was in a high state of activity and it was possible to confirm the chaotic behaviour of its emission on all time scales in this condition. Cyg X-3 was in a low state, but it was still possible to detect the 4.8 h modulation of its intensity, which was not seen at gamma-ray energies. Detailed study of this source was prevented by the strong contribution of Cyg X-1 to the counting rate. In 1977 Cyg X-3 was seen with about the same efficiency, but the pointing direction was such that Cyg X-1 was outside the field of view of the pulsar synchroniser. In this situation it was possible to derive new

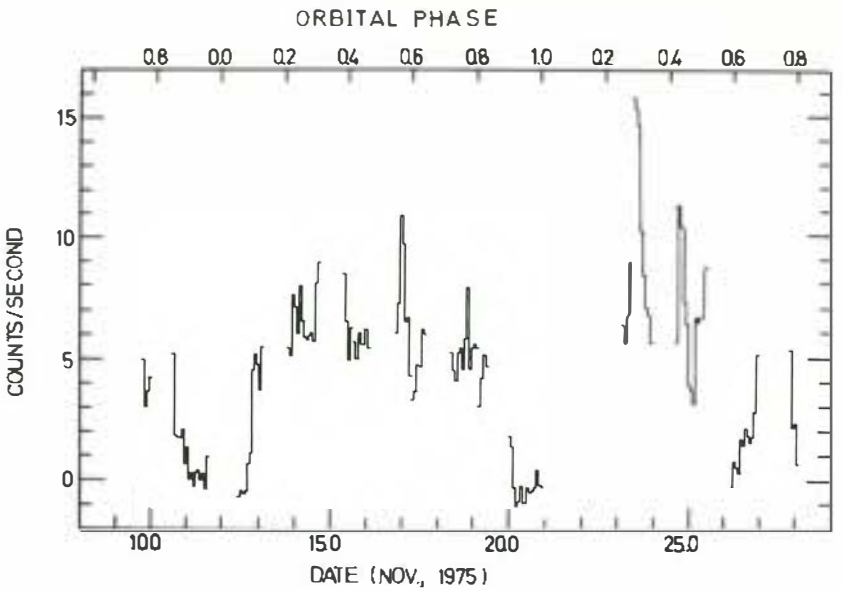

Figure 14. The observed counting rate from the source 4U0900-40 in the 2-12 keV energy range, averaged over 66 min intervals. The background counting rate, determined from the eclipse measurements, has been subtracted. Most of the gaps in the data correspond to passage of the satellite through the Earth's radiation belts.

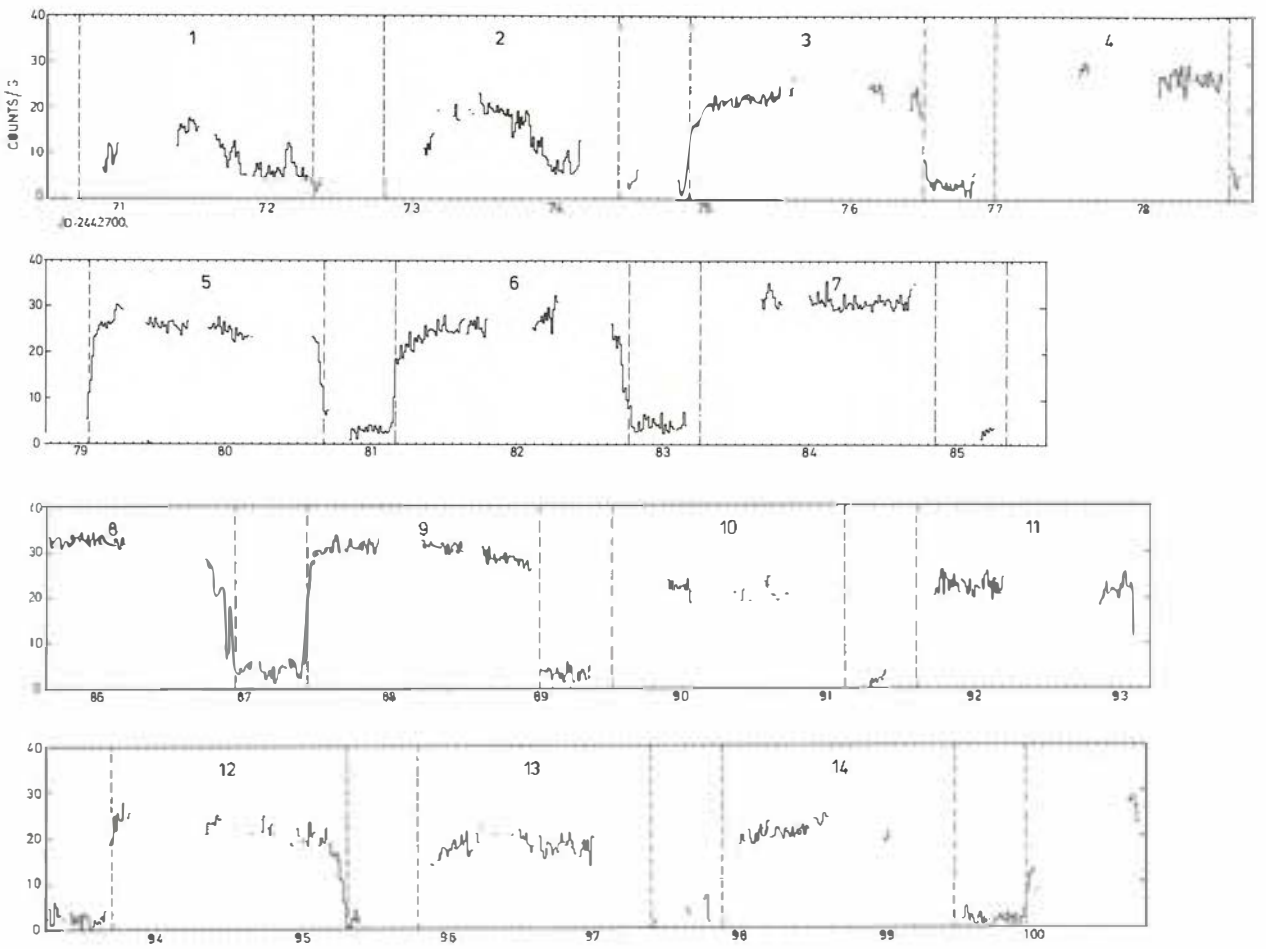

Figure 15. The counting rate from Cen X-3 in 1024s bins during 14 consecutive binary cycles. Data gaps are due to contamination by charged particles.

values for the period P of Cyg X-3 and its derivative $\dot{P}$, giving a value of $\dot{P}/P = (5.2 \pm 1.2) \times 10^{-6}$ yr^{-1} which is a factor 3 below the upper limit previously derived from the ANS satellite.

Vel X-1 (4U0900-40) is an eclipsing binary with an orbital period ~9d. The long continuous observation by Cos-B in 1975 enabled the counting rate to be studied over two complete cycles. Figure 14 shows in addition to the two eclipses, the strong intrinsic variability of the source in time scales of hours. This source also exhibits pulsations of period 283 s. By studying the Doppler variation of this period, it was possible to determine from the Cos-B data more accurate values for the orbital elements of 3U0900−40 than were previously available. Comparison of the measured period with that determined by SAS-3 five months earlier led to the unexpected conclusion that the period had increased during that time, though the 1976 observation by Cos-B indicated that on the longer time scale the source shows the same decrease of pulsation period exhibited by other X-ray pulsars.

During the Cos-B observation of Cen X-3 in December 1975/ January 1976 the binary system executed a total of 14 revolutionary cycles. The measured orbital period of 2.08711 ± 0.00001 d indicated a somewhat slower decrease in period than had been derived from earlier measurements. During this period the source underwent a transition from a low-intensity state to one in which it reached twice the maximum value observed by Uhuru (Fig. 15). The long observation by Cos-B permitted the 4.8 s periodicity of Cen X-3 to be studied as a function of time. The results appear to indicate that the period derivative varies on a time scale of days. All of these conclusions place significant new constraints on models of the mechanisms of X-ray emission and absorption in Cen X-3.

Conclusions

Although those Cos-B results that have so far been published are derived from less than a third of the data accumulated to date, they represent a major advance on several fronts in the field of gamma-ray astronomy. Substantial reserves of data are currently being analysed, including some from parts of the sky which were not investigated by SAS-2, the most successful gamma-ray astronomy satellite before Cos-B. At the same time work continues in the direction of extracting more information from the data already studied. This is a direct consequence of the first round of publications which have triggered a variety of correlative studies in other energy ranges and have inspired many theoretical papers on the production of gamma rays in the Galaxy and in localised sources. Such studies invariably raise new ways of testing hypotheses, some simply by making a different analysis of the data available, others by carrying out new or repeated measurements. It is thus fortunate that Cos-B has exceeded its design lifetime and it is to be hoped that it will continue to serve the community of gamma-ray astronomers for months to come.

Geos-1 & 2

Magnetospheric dynamics

Geos-1 was launched on 20 April 1977. As a result of a launcher malfunction a transfer orbit with low apogee was reached. The deficiency was such that the apogee boost motor could not be used for injection into geostationary orbit, and only a 12-hour eccentric rescue orbit was reached. In view of the limited scientific value of this rescue mission, the launch of the refurbished qualification model was approved in December 1977 and executed on 14 July 1978. A nominal geostationary orbit was reached.

Introduction

One of the early discoveries of space research was the existence of a continuous plasma stream moving radially outwards from the Sun into interplanetary space. This plasma stream distorts the dipolar magnetic field of the Earth and confines it to a cavity of finite dimensions. This cavity, which is 20-30 Earth radii in diameter and more than 100 Earth radii long, is called the terrestrial magnetosphere. Surprisingly, satellites launched in the sixties and early seventies and dedicated to exploration of the solar wind and the magnetosphere established that the particle population inside the magnetosphere is much more energetic in total than the bulk population of the solar wind. Since that time magnetospheric research has concentrated on obtaining answers to three most important questions:

1. Where do these energetic magnetospheric particles originate? The only possible sources are the solar wind or the Earth's atmosphere, both of which contain particles of low energy.
2. How are such low-energy particles accelerated?
3. How do they penetrate the magnetopause and how are they transported?

It was felt by the European scientific community that these questions could best be tackled by a satellite in the geostationary orbit. This orbit has distinct advantages and it is most surprising that apart from some 'piggy-back' packages on communication and meteorological satellites no magnetospheric research has been done so far from any other geostationary satellite. In 1969 the Geos mission was introduced into ESRO's scientific programme. The objective of this mission was to carry out integrated particle, wave, field and plasma measurements in the geostationary orbit.

Table 1. Geos experiments.

Experiment	*Scientific groups*	*Measurement*	*Technique*
S300	CRPE, Issy-les-Moulineaux, France Space Science Dept., ESTEC, Holland Danish Space Research Institute, Lyngby	AC magnetic fields up to 30 kHz DC/AC electric fields and plasma resonances up to 80 kHz Mutual and self-impedance	Search-coil magnetometer Electric aerials Emission and reception of VLF signals
S302	Mullard Space Science Lab., Dorking, UK	Study of thermal plasma	2 electrostatic analysers
S303	University of Bern, Switzerland and Max Planck Institute Garching, Germany	Composition, energy spectra & angular distribution of ions	Combined electrostatic and magnetic analyser
S310	Kiruna Geophysical Observatory, Kiruna, Sweden	Pitch-angle distribution of electrons and protons in the 0.2 – 20 keV energy range	10 electrostatic analysers
S321	Max Planck Institute, Lindau, Germany	Pitch-angle distribution for electrons (20-300 keV) and protons (20 keV-2 MeV)	Magnetic deflection system followed by solid-state detectors
S329	Max Planck Institute, Garching, Germany	DC electric field and grad|B|	Tracing of electron beam over one or more gyrations
S331	CNR, Frascati, Italy	DC and ULF magnetic field	Fluxgate magnetometer

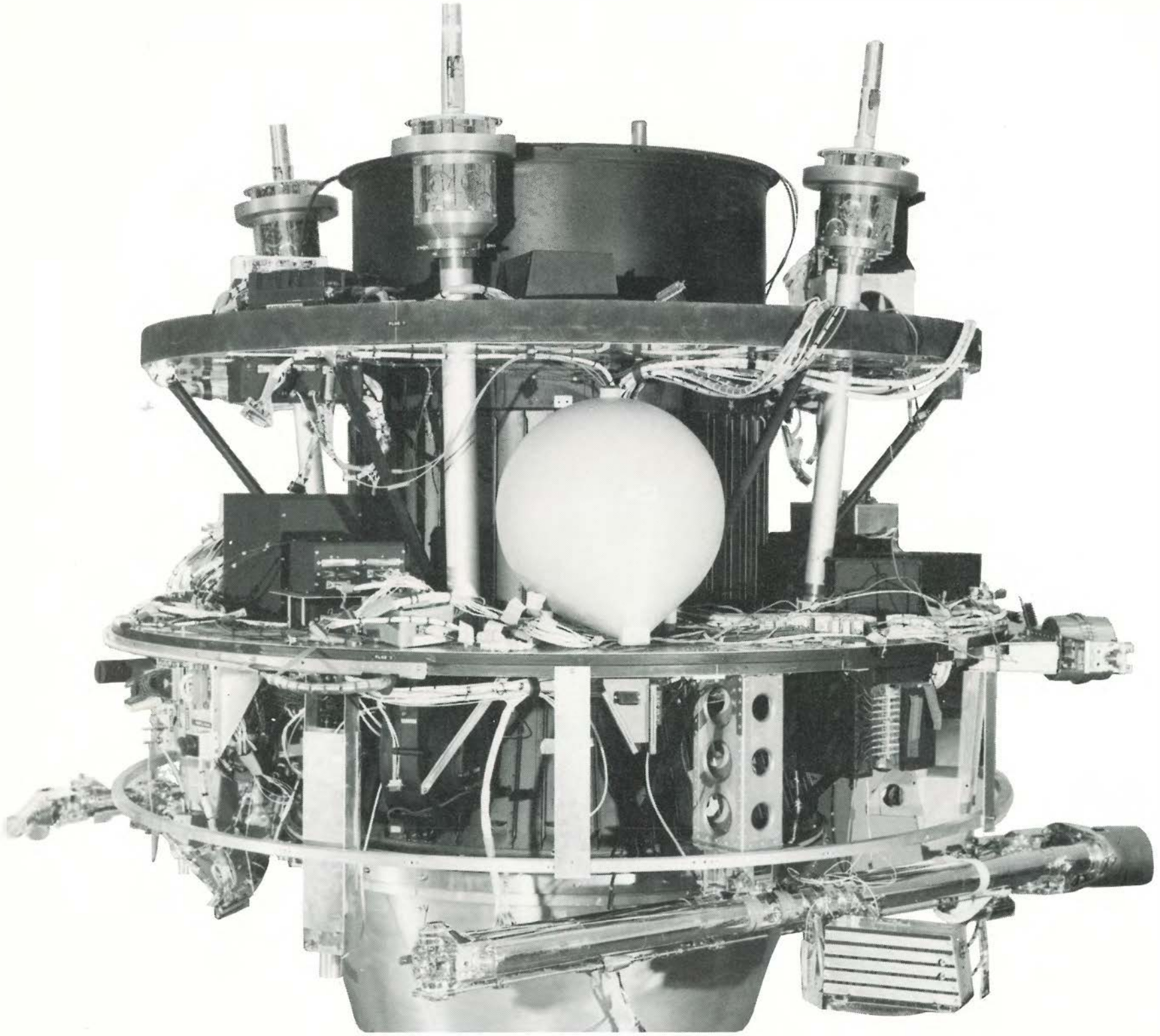

Advantages of the geostationary orbit

The position of the geostationary orbit in the frame of reference of the magnetosphere is shown in Figure 1.

It is situated between two boundaries of fundamental importance for magnetospheric dynamics, the 'plasmapause' and the 'inner edge of the plasma sheet'. The former terminates a near-Earth reservoir having a dense but cool particle population at a distance of some $3\,R_E$ from the Earth, while the latter marks the transition to a low-density but high-temperature population, at about 8-$10\,R_E$. The two boundaries are not fixed and change their positions as a function of solar activity and solar-wind intensity. During very quiet periods the whole magnetosphere expands and the plasmapause may move beyond the geostationary orbit. During periods of disturbance, the magnetosphere is compressed, the plasmasphere shrinks, and the inner edge of the plasma sheet crosses the geostationary orbit. The compression can go so far that the geostationary orbit will fall outside the magnetopause. Geos is thus in an ideal position to monitor these important transitional processes.

The stationary character of the Geos orbit makes it possible to establish the average geophysical conditions in the equatorial plane at a geocentric distance of $6.6\,R_E$. Any deviations from this average is therefore indicative of temporal variations, so that Geos is able to discriminate to a certain degree between temporal and spatial variations. Such discrimination has proved difficult with previous satellite missions and can only be achieved completely if a suitable pair of satellites is employed.

Another attractive feature of the geostationary orbit is its magnetic conjugacy to the auroral zone. Geos is positioned on magnetic field lines which connect with both the northern and southern auroral ovals. Because particles are guided along magnetic field lines, the particle population monitored by Geos should contain those particles that generate the well-known auroral displays. Co-

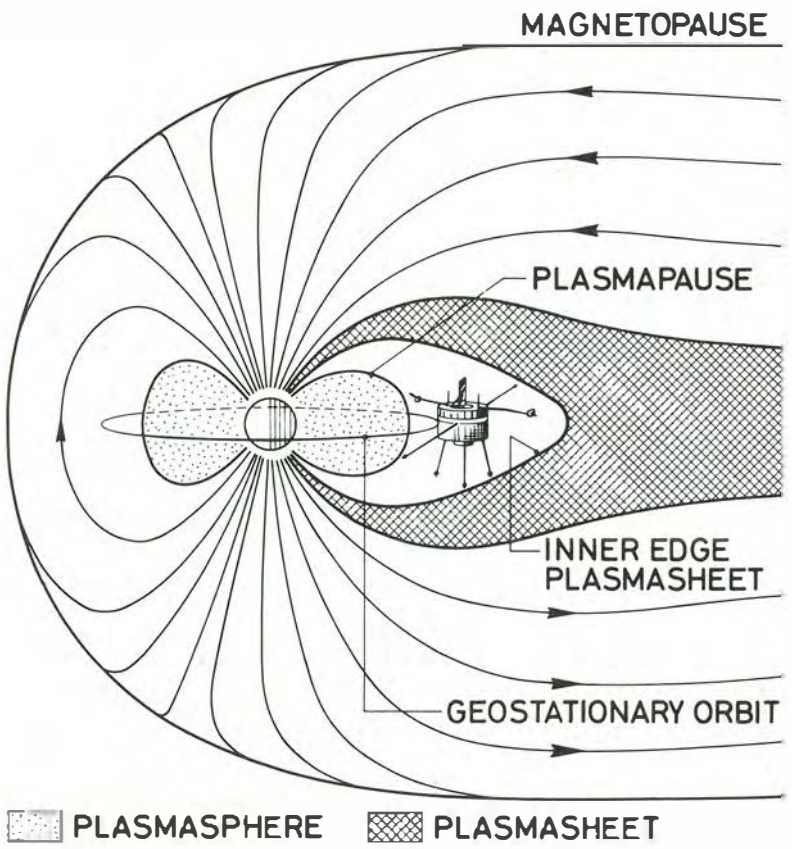

Figure 1. The position of the geostationary orbit in the frame of reference of the terrestrial magnetosphere. The orbit is situated in the very centre of this magnetic cavity and ideally suited for its exploration.

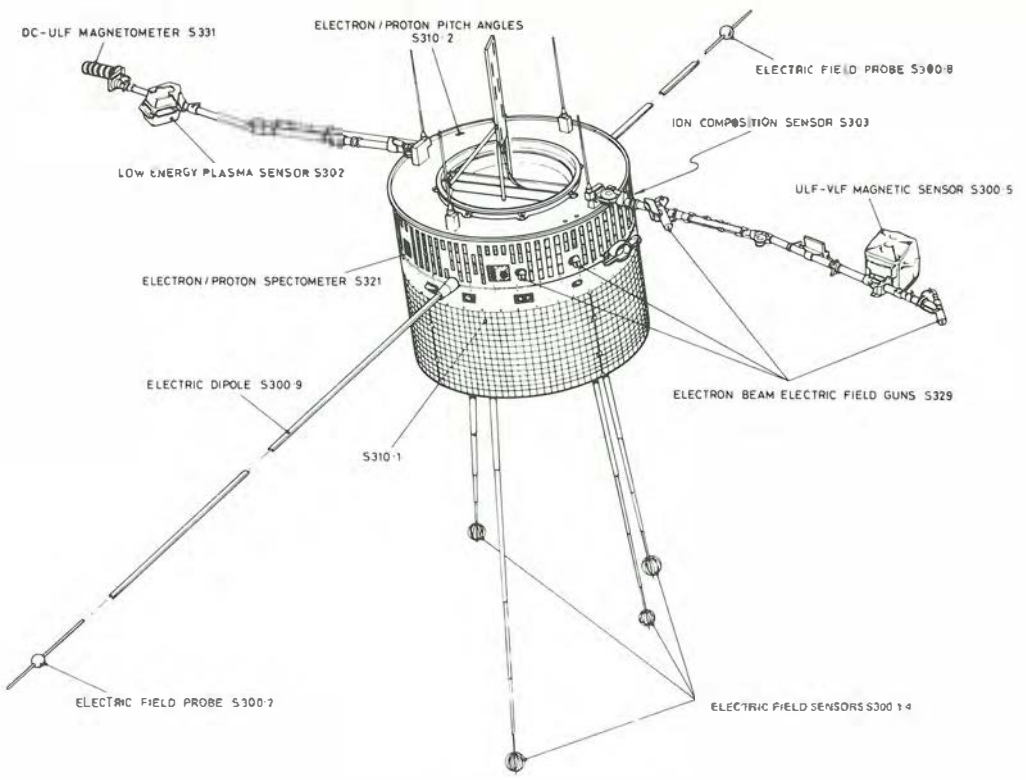

Figure 2. Accommodation of all experiment sensors carried by Geos in orbital configuration. A total of 4 radial and 4 axial deployable booms was necessary to satisfy all experiment accommodation requirements. In particular field, wave and low-energy particle detectors had to be mounted away from the main satellite body.

ordinated ground-based experiments carried out at the footprints of the Geos field lines therefore increase our knowledge of the origin and acceleration of auroral particles.

Payload operation also benefits greatly from the stationary character of the orbit and the satellite's resulting constant visibility from its ground station. Downlink and uplink communication is maintained for 24 hours per day throughout the mission. The experiment data, arriving at a rate of approximately 100 000 bit/s, are treated in real time by an on-line ground-based computer system. The optimum mode of payload operation is determined automatically and the necessary telecommands can be sent at some 100 bit/s. These factors allow the operational flexibility of the payload to be fully exploited.

The payload

The attractiveness of the Geos mission stems also from the composition, sophistication and flexibility of its payload, which is designed to conduct simultaneous wave and particle measurements whilst monitoring the basic background parameters, such as electric and magnetic fields, as well as the total plasma density. Waves are measured in six components with frequency coverage up to 80 kHz, while particle experiments explore energies extending from the suprathermal to the MeV range with high spatial and temporal resolution. In the past, experimental difficulties have prohibited the reliable measurement of electric fields and plasma densities in magnetospheric regions outside the plasmasphere. By applying newly developed techniques and partly active experiments on Geos, we are now achieving reliable measurements of these most important parameters, which have until recently been inaccessible. In fact, Geos is the first spacecraft to employ active experiments – the resonance technique for density measurements and an electron beam experiment for electric field measurements in the outer magnetosphere.

The payload, summarised in Table 1, consists of seven experiments, of which four measure particles in various energy ranges, and three fields and waves in various frequency domains. Figure 2 shows how the various experiment sensors are accommodated on the spacecraft. It is worth pointing out that this spacecraft has been proved to be a very clean measuring platform from the electromagnetic, electrostatic and chemical points of view.

Geos-1

Because of its unique orbit and the sophistication of its payload, Geos was selected to be the reference spacecraft in a world-wide study period called 'The International Magnetospheric Study' (IMS). To the community involved in this study and in particular to the Geos experimenters, Geos-1's failure in April 1977 to reach the planned geostationary orbit came as a great disappointment. Nothing better than a 12-hour eccentric orbit with apogee at 38 000 km and perigee at 2050 km could be achieved by this spacecraft and many of the above-mentioned advantages of the original Geos mission were lost. In its emergency orbit, Geos-1

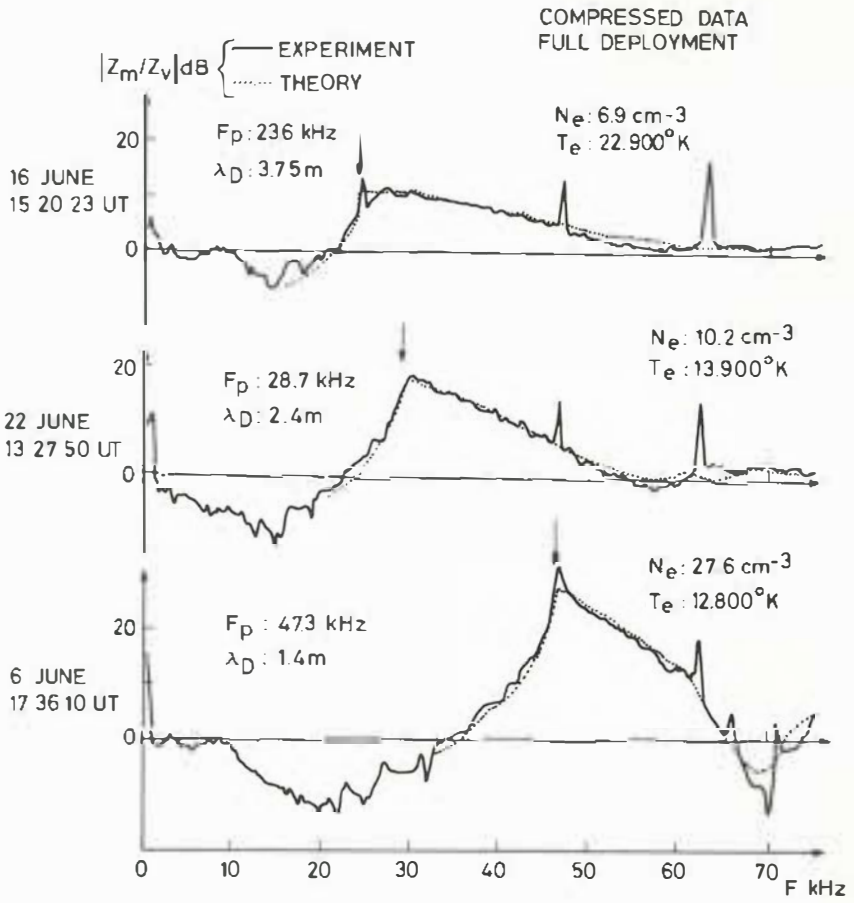

Figure 3. Results from the active so-called 'mutual impedance' experiment on Geos-1. The measured plasma impedance is plotted as a function of frequency. A pronounced maximum occurs at the plasma frequency. Knowledge of this frequency is equivalent to knowing the plasma density. In addition, curve-fitting techniques can be applied to determine the plasma temperature.

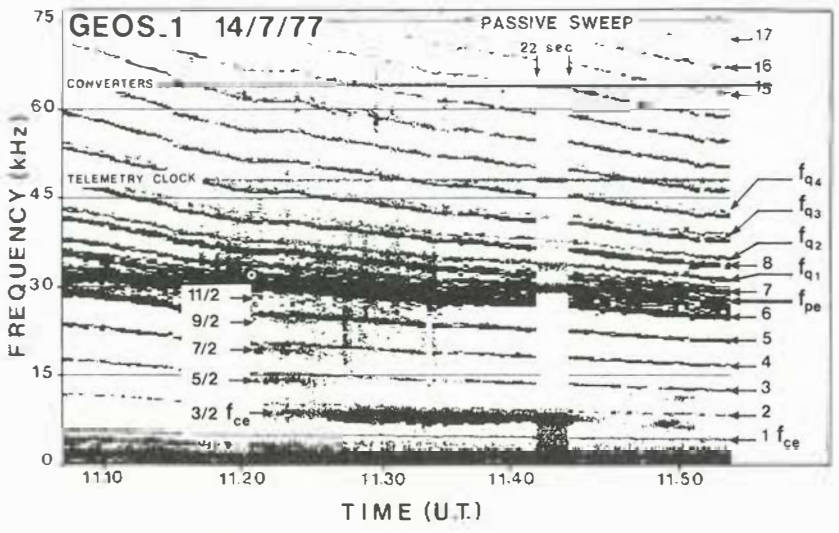

Figure 4. Results from the Geos wave experiment. A time frequency plot with wave intensity in grey scale has been used to present the data. It can be seen that besides the plasma frequency and the electron gyrofrequency severe additional resonances and harmonics are triggered by the V LF transmitter which is part of the Geos wave experiment.

Figure 5. Typical results from the Geos electron-beam electric-field experiment. The experiment measures the deflection of an electron beam – fired over a distance of several kilometers – to determine the electric field. Each of the superimposed traces represents the output from the electron beam detector during one satellite spin period. The separation of the peaks in the electron-beam current quantifies the electric field.

started to return novel scientific data of high quality in spite of difficulties with saturation at lower altitudes in some experiments. Previously unknown quantities (plasma density and electric fields) were measured with good accuracy and for the first time it was possible to combine particle measurement with the results of a sophisticated wave experiment. Geos-1 when at apogee also conducted for the first time high-precision mass spectrometry in the outer magnetosphere.

Only four highlights of Geos-1 results can be given here. Figure 3 demonstrates the capability of the active wave experiment to measure both the density and the temperature of the plasma in the distant magnetosphere. Figure 4 is a snapshot from the passive wave experiment when operated in conjunction with the VLF transmitter on Geos-1. A wealth of previously unseen plasma resonances is made visible. These observations contribute to progress in basic plasma physics.

Figure 5 shows results from the most novel experiment flown on Geos-1, the electron-beam electric-field experiment. Before the launch of Geos-1 this experiment was considered most ingenious in principle, but for various reasons there was doubt that it would work in the distant magnetosphere. Figure 5 is an impressive demonstration that the experiment works as expected and that reliable data on electron fields are being returned. Figure 6 shows results from the Geos mass spectrometer. The data obtained from this experiment are casting a new light on our understanding of magnetospheric transport mechanisms.

After 14 months of orbital operations, the Geos-1 mission must be classified as scientifically useful. Owing to the flexibility of the Geos payload and the excellent functioning of the spacecraft, Geos-1 managed to make a significant contribution to the ongoing IMS, in spite of the fact that it had to operate in an emergency orbit quite unlike the geostationary orbit planned for it.

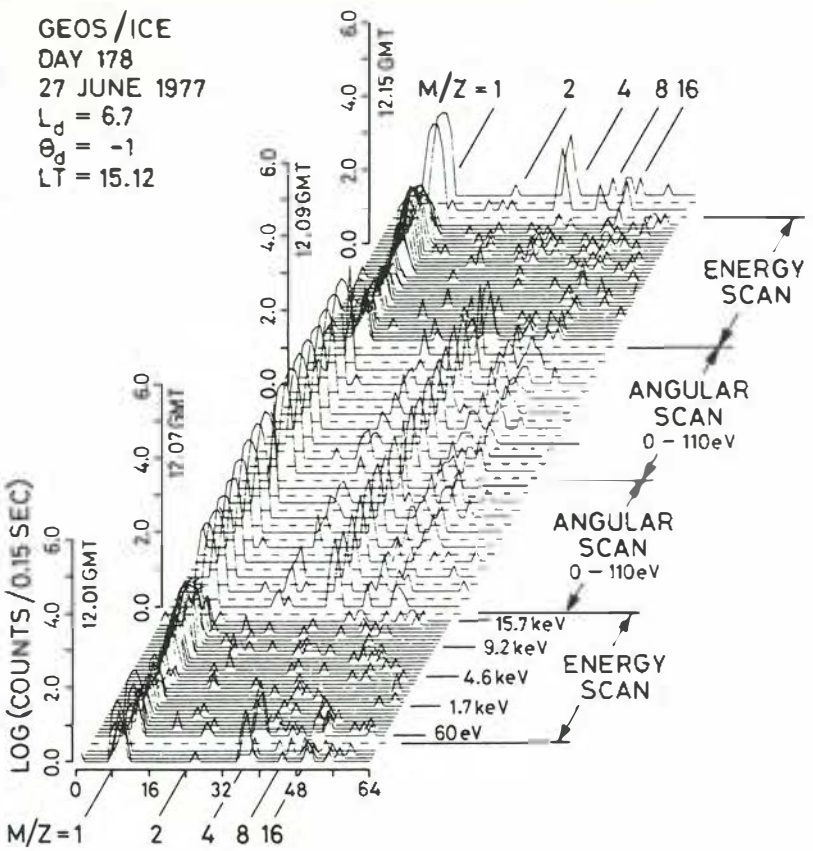

Figure 6. Results from the Geos-1 mass spectrometer. The three-dimentional picture gives a sequence of mass spectra obtained at various energies or for the angular scan subdivided into nine different viewing directions. Most noticeable is the presence of doubly charged helium and oxygen in the angular scan data (0–110 eV energy range).

Geos-2

Very soon after Geos-1 had failed to achieve the planned truly geostationary orbit, the scientific community urged ESA to look into the possibility of launching a second model of this very sophisticated spacecraft.

A fully operational Qualification Model was still available and all experimenters were still in possession of spare instruments. It was therefore argued that a relatively small additional sum was necessary to bring the full Geos mission, as originally conceived, to fruition.

ESA's Scientific Advisory Committees endorsed these points of view and the Council agreed first to an accelerated refurbishment of the Qualification Model and later, in December 1977, to financing the launch of the spacecraft by a Delta Vehicle. This decision, of course, entailed the cancellation of the plan to launch the Qualification Model by Ariane in 1979, a project that had been given the name Geosari.

Geos-2 was launched on 14 July 1978 and reached the planned truly geostationary orbit a few days later. Based on the experience gained with Geos-1, the spacecraft and payload commissioning went very smoothly. Routine operations started in early August 1978 and detailed evaluation of the data received has been in progress since then.

Figure 7 gives a highly condensed and selected output from Geos-2 over a period of 24 hours. This output is called a 'Daily Summary'. It is generated by ESOC normally within 1 week of data acquisition and is distributed worldwide to the IMS community. It is on such summaries that scientific co-operation between Geos experimenters and their colleagues working in other IMS programmes is based.

Figure 7. Daily summary plots of Geos-2 data showing compressed magnetic and electric wave field data (upper part) and particle data (lower part). These plots are generated by ESOC within one week of data acquisition and are distributed worldwide. (The periodic pattern in the VLF electric field data is due to the operation of the active plasma resonance experiment and has no scientific significance).

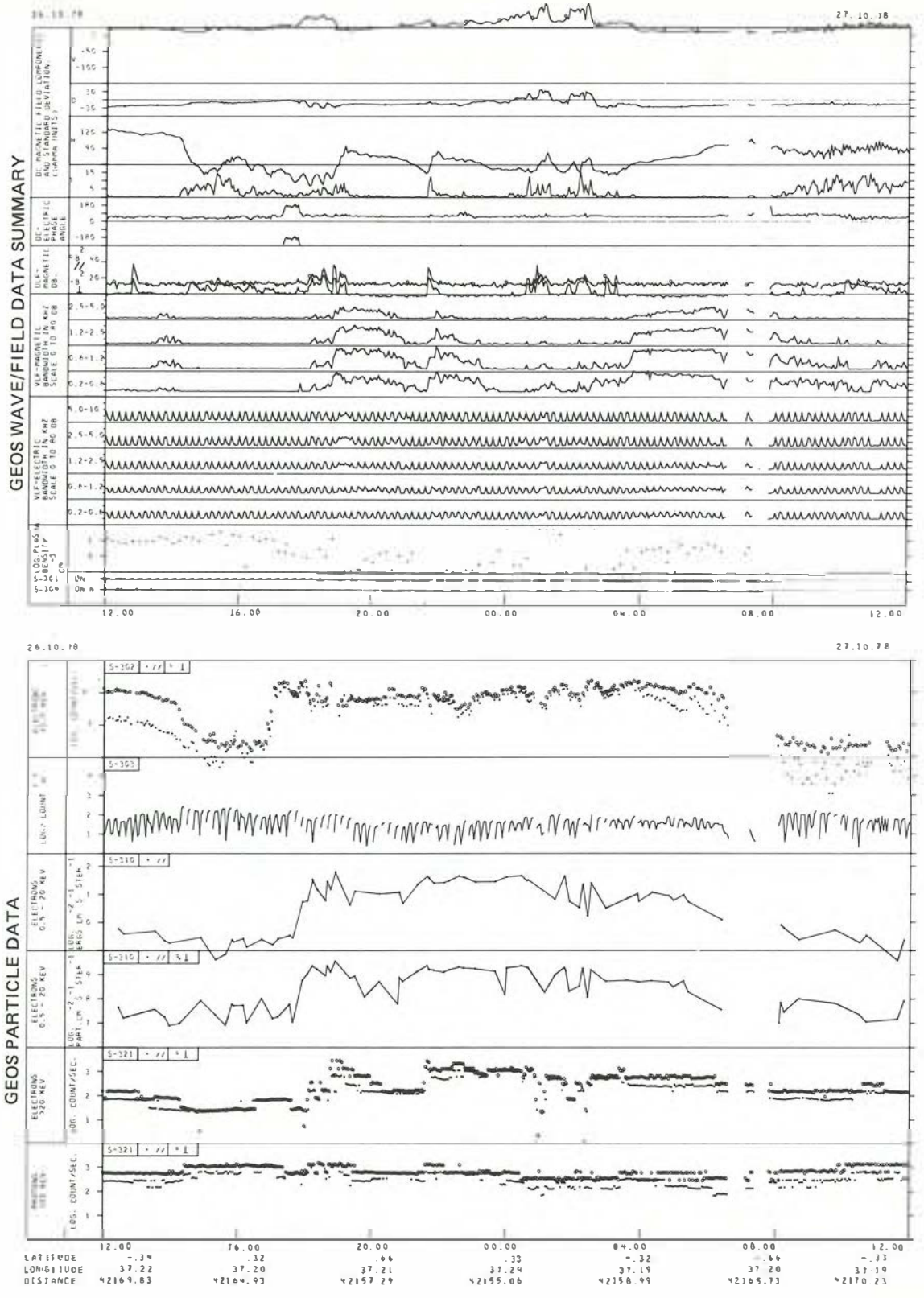

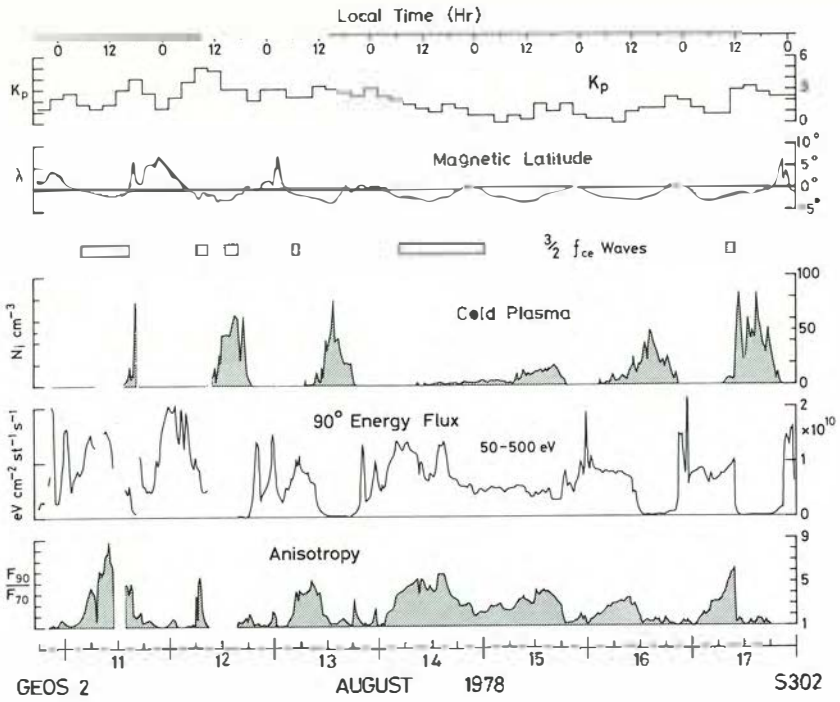

Figure 8. Results from the Geos-2 low-energy plasma experiment combined with results from the wave experiment. It is interesting to note that a particular wave generation mechanism only becomes operative in the absence of cold plasmas and in the presence of a particle population of higher energy and greater anisotropy.

At the time of writing, analysis of Geos-2 data was in full swing. One interesting result from a preliminary wave/particle study is presented here to illustrate the potential of the Geos-2 data. Figure 8 shows data acquired by the Geos-2 low-energy plasma experiment combined with Geos-2 wave data and also plotted against the magnetospheric disturbance index K_p. The proximity of Geos-2 to the geomagnetic equator is also indicated in the figure. The preliminary conclusion that can be drawn from this combination of Geos-2 data is that a particular wave-generation mechanism is dependent on the absence of cold plasma and on the presence of a particle population of higher energies having a velocity distribution primarily perpendicular to the magnetic field direction.

As a final remark, it may be mentioned that Geos-1 acquired scientific data between 3 May 1977 and 23 June 1978 for an average of 10 hours per day, while Geos-2 has been fully operational since 3 August 1978 on a 24-hour per day basis. Towards the end of 1978, it was possible to reactivate Geos-1 for 3 hours per day and a scientifically very valuable parallel operation of the two Geos spacecraft at different points in the magnetosphere was achieved.

Sounding Rockets

Results of ESRO's sounding-rocket programme

Although the first launching in ESRO's sounding-rocket programme took place in 1964, *the programme only reached full strength in* 1966 *with the opening of the Organisation's own rocket range near Kiruna, in Sweden. The programme was effectively terminated in July* 1971, *when the ESRO Council agreed to a reform of the Organisation, through a resolution which included a clause to the effect that, following a certain transition period, sounding-rocket activities would no longer form part of the Organisation's ordinary activities. As a result of this decision, ESRO's last sounding-rocket payloads were launched in* 1972.

During the seven years that it lasted, ESRO's sounding-rocket programme played an important role in promoting space research in Europe. Many scientific groups gained their first experience in building space hardware through this programme, and the multi-experiment, multi-national rocket payloads provided good practical training for the more demanding work in connection with satellite experiments. Scientists from the Organisation's smaller Member States, which did not have national rocket programmes, were particularly appreciative of the opportunities that the ESRO programme offered.

Important new results were obtained in the exploration of the upper atmosphere and ionosphere, particularly near the auroral zone. The programme also provided many opportunities for testing new experiments, and for conducting new science in the fields of solar physics and astrophysics by means of stabilised rockets. For the sake of brevity, we will concentrate here on a few examples of the scientific results achieved rather than attempt to cover the large number of scientific disciplines represented, in detail.

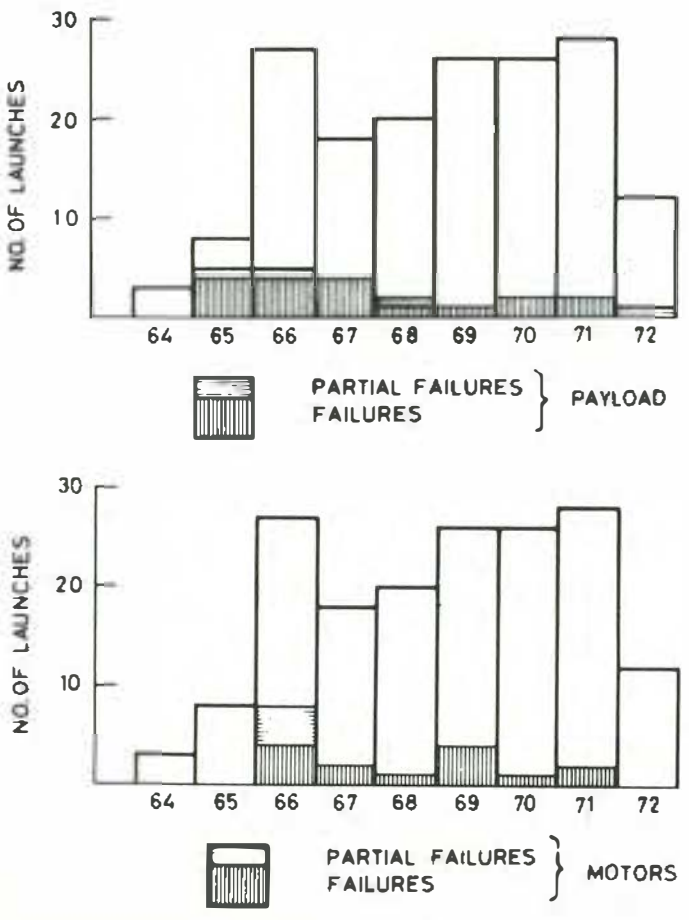

Figure 1. Rockets launched in the ESRO programme and the success rates for payloads and rockets.

Summary of programmes and launches

The annual launching campaigns and the success rates that were achieved are summarised in Figure 1. In the early days of the programme, all the rockets launched were concerned with studies of the atmosphere and ionosphere. In the last four years, however, pointing rockets for studying the Sun and stellar objects were also launched. A total of 12 Sun-pointing rockets were launched, 10 of which were successful. Only four stellar-pointing rockets were launched, two with European pointing systems, and two with an American system; all were subject to attitude-control failures. The disappointing results must be viewed against the developmental nature of the stellar-pointing systems.

After the opening of Esrange, near Kiruna, in 1966, a large number of rockets were launched to study the atmosphere and ionosphere near the auroral zone. During the years 1969 to the end of 1972, there was an uninterrupted sequence of 44 successful launchings, a success rate that clearly heralded European industry's and ESRO's mastery of sounding-rocket technology.

In examining the statistics of Figures 1 and 2 it must be borne in mind that no distinction has been made between small simple payloads and large complex pointing payloads, and the percentage of complicated payloads was of course higher during the latter years of the programme.

As shown in Figure 2, by far the greatest percentage of launchings took place at Esrange and at the Sardinia range. Operations at Esrange were characterised by relatively simple payloads, but complicated launch conditions. A large proportion of the payloads launched from Sardinia were pointing payloads requiring more elaborate preparation, but then launch conditions were more favourable.

Ile du Levant (France) and the Island of Karystos (Greece) were used for special campaigns, and the Andøya range for launchings of such rockets as the Dragon, which could not be launched from Kiruna. Woomera (Australia) was also used, to launch star-pointing rockets intended for observation of the southern sky.

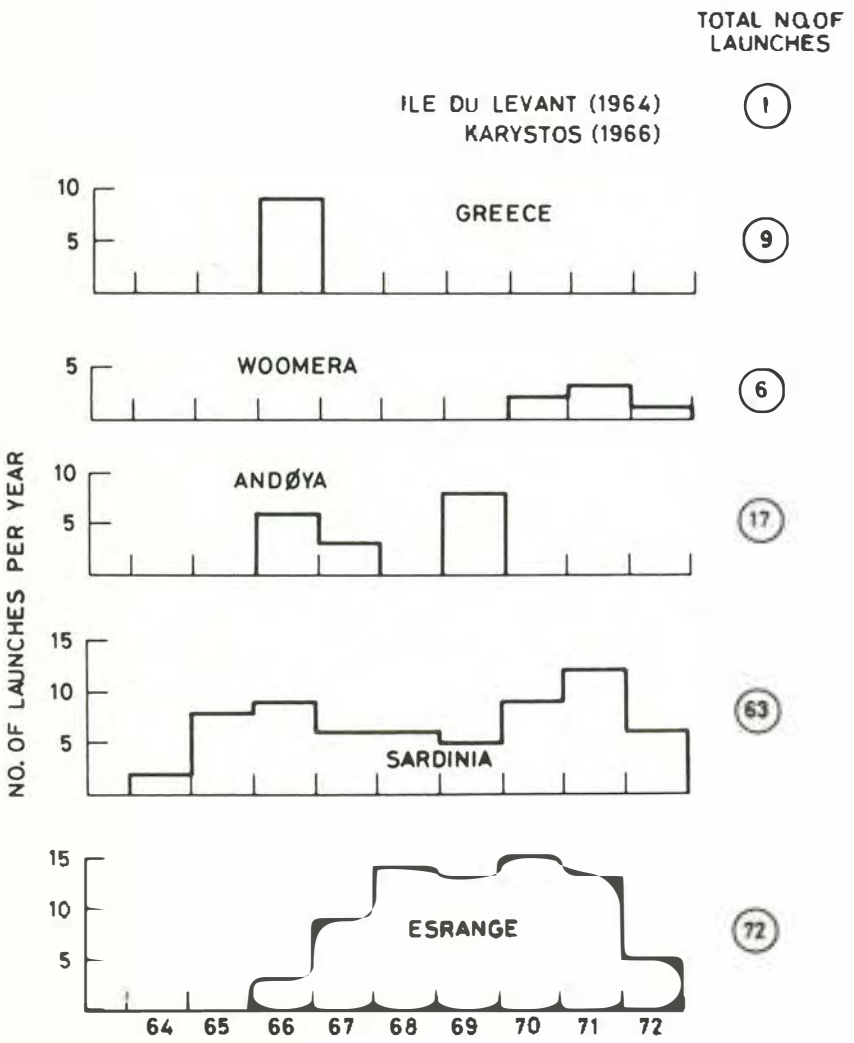

Figure 2. Distribution of rocket launches between ranges used in ESRO's rocket programme.

Scientific results

Studies of atmosphere and ionosphere

Rocket-borne investigations of the auroral atmosphere and ionosphere were one of the main drivers when the sounding-rocket programme was started. These investigations made it possible to establish such parameters as density, temperature of neutral and ionised constituents and their motions by direct measurement. As a result, the perturbations occurring during geophysical disturbances have subsequently been described and energetic particle precipitations established. The studies gradually evolved from an understanding of the average parameters, on the basis of both accumulated experience and a parallel improvement in instrument sophistication.

Towards the end of the ESRO rocket programme, the goals were directed more towards the gathering of a set of measurements under special geophysical conditions. Broadly speaking, the aim was then to study the energy flow between the solar wind, magnetosphere and the atmosphere/ionosphere, and all the detailed processes resulting from that flow.

It could be established that particle accelerations sometimes occurred near the equatorial plane on magnetic field lines connected to the auroral zone, and under different conditions nearer to the ionosphere.

The studies of particle precipitation and the wave-particle-plasma interactions generated yielded results in many cases not only of geophysical interest, but also of importance to fundamental plasma physics.

Example 1: Mass-spectrometer measurements

Development of mass spectrometers for rockets was begun at three main institutes in Europe (University of Bern, University of Bonn and Max Planck Institute, Heidelberg). All had long histories of mass-spectrometry work and sought to adapt their knowledge to rocket technology. Important results concerning neutral and ion composition were obtained on a number of flights. Measurements down to 60 km altitude called for cryo-pumped systems and it was possible to see important science related to atmospheric and ionospheric composition emerge as the technology was refined from flight to flight.

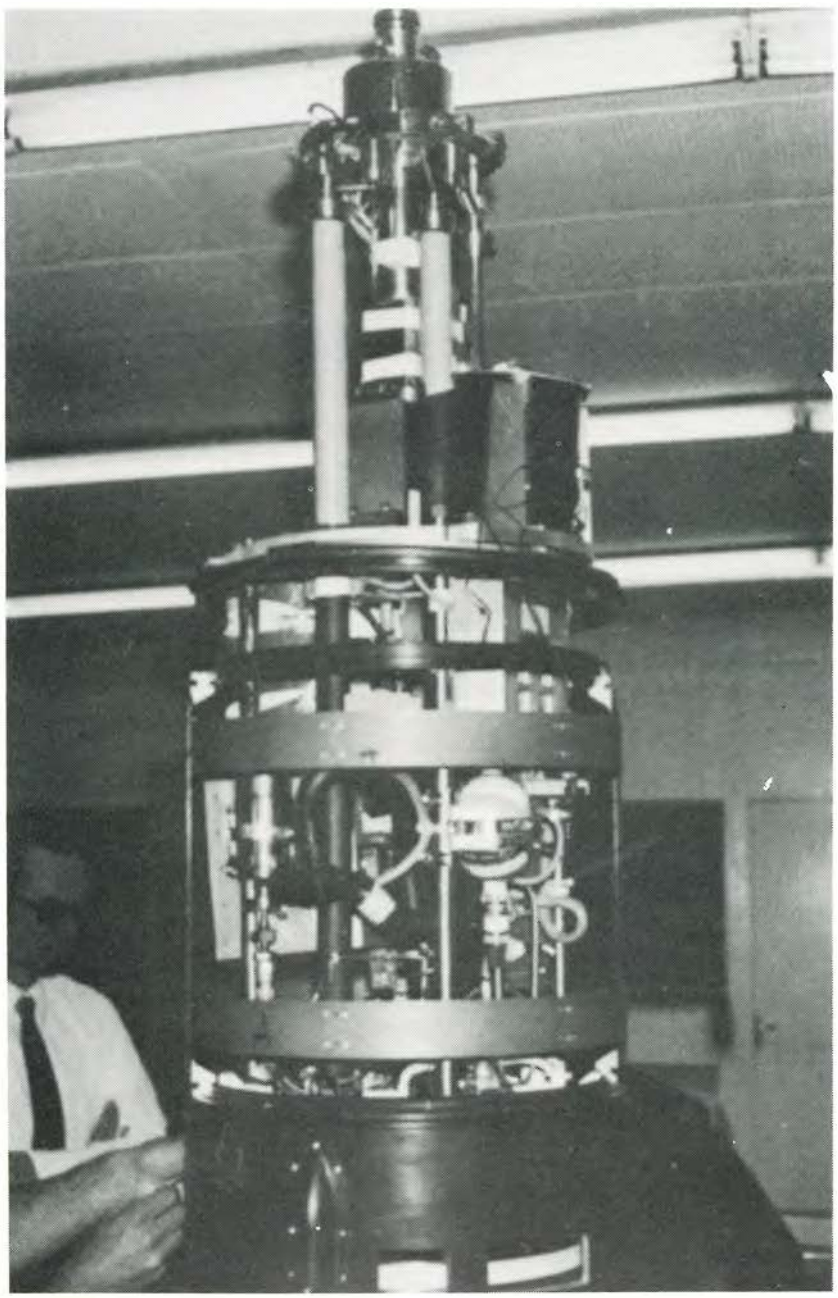

Figure 3. Payload S75 required complicated cooling systems for the experiments on board.

Interestingly, the experience gained with the rocket launchings has proved to form the basis for very successful mass-analyser studies using satellites: the University of Bonn flew a very successful experiment on ESRO-4 and, together with MPI, Heidelberg, now has an experiment on NASA's Venus Orbiter. The University of Bern has achieved new and important results with the analysis of high-energy-ion results from the Geos and ISEE satellite missions.

One of the successful launchings of a mass-spectrometer was that on a Skylark rocket (payload S-75) by the University of Bonn. The aim of experiment R242 was to measure atmospheric composition, including trace components (including carbon dioxide and the chemically reactive atomic oxygen and ozone), and to extend the altitude region of this measurement down to the mesopause. For this region a helium-cooled ion source had been developed, the front part of which was cooled efficiently to 20°K in order to freeze the shock ahead of the instrument. The payload, including the rather complicated cooling systems needed for the two experiments, is shown in Figure 3. Two successful flights of this particular payload were made from Sardinia, on 25 and 30 of March 1972.

The good quality of the spectra obtained can be seen from Figure 4a, which shows almost no background signals prior to cap ejection, and peaks from major and minor constituents thereafter. Mass-spectrometer current profiles corresponding to N_2, O_2, Ar, CO_2 and 0_3 can be seen in Figure 4b as a function of altitude.

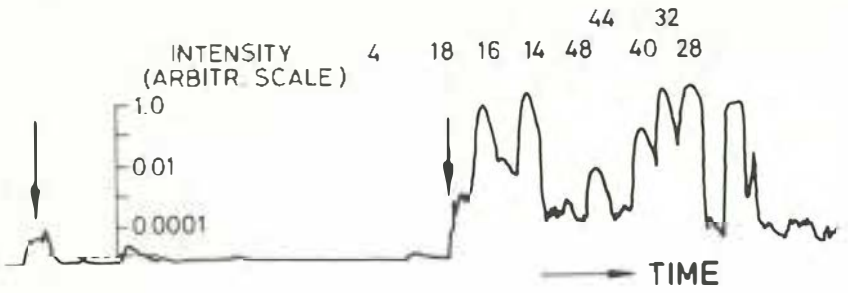

Figure 4a. Example of mass spectrum of neutral molecules obtained with helium-cooled mass spectrometer after cap release (arrow). Noise level is extremely low before cap release.

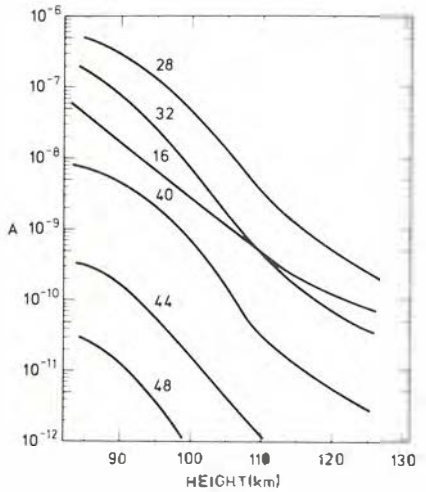

Figure 4b. Mass spectrometer ion currents as a function of altitude for various neutral species obtained during the flight of S75.

Example 2: Measurement of solar radiation

The results of an experiment R220: Absolute solar UV flux, from Institut d'Aéronomie Spatiale, Brussels – flown together with a UV experiment provided by the University of Munich and a mass-spectrometer provided by the University of Bonn, can be considered representative of the solar-radiation measurements undertaken as part of the ESRO sounding-rocket programme.

These two Sun-stabilised payloads were designed to measure the solar flux in the wavelength range 1216 Å to about 2100Å, the altitude-dependent extinction of this radiation, and the correlation between these data and independent, simultaneous mass-spectrometric density determinations of the main absorber of the radiation, namely molecular oxygen. The two Skylark rockets were launched from the Salto di Quirra range in Sardinia on 28 February 1972, to altitudes of 242 km (S84) and 251 km (S90). The short interval between launchings made it possible to study both night and day conditions without marked changes in the Sun's radiation and the atmosphere.

Experiment R220 consisted of an Ebert-Fastie spectrometer used over three wavelength intervals. A lithium fluoride window was placed in front of the entrance slit to integrate radiation over the complete solar disk and the three exit slits were uncovered in sequence by means of a sliding shutter.

The results obtained are shown in Figure 5. The value obtained at Lyman-α is lower than the usually accepted average value of 3×10^{11} photons/cm^2/s. The S84 and S90 flights took place when the Zurich Sun-spot number, as well as the 10.7 cm solar flux, was low. This can be correlated with low Lyman-α fluxes also observed from the OSO-V satellite. The flux values presented here are lower at 1450 Å and 1700 Å than the published values. It is now certain that the apparent blackbody temperature of the Sun can decrease by some 800 K from 2100 to 1600Å. The steps are possibly as follows:

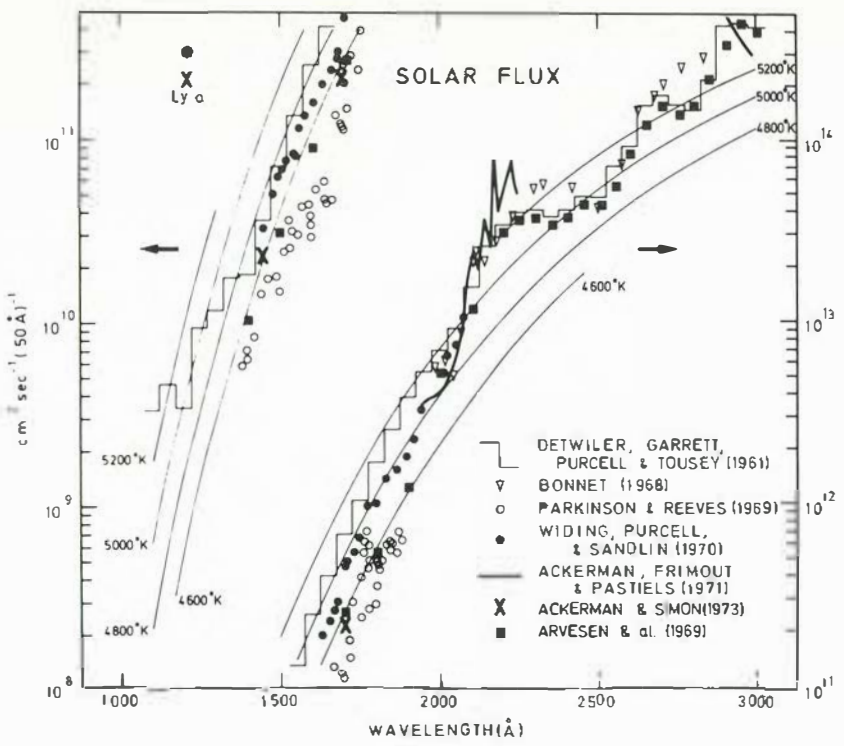

Figure 5. Solar flux as measured by experiment R220 compared with the results of earlier experiments.

5200 K at 2100Å, 4800 K at 2000Å, 4650 K at 1900 Å, 4550 K at 1700 Å and 4600 K at 1450 Å with a minimum at 1600 Å of the order of 4400 K.

Continuation of sounding-rocket research

Germany, the United Kingdom, Spain and three of the Scandinavian countries have continued to pursue national programmes, often with participation by other European and American groups. The trend in these national programmes has been towards greater detail in the study of the dynamic behaviour of atmosphere and ionosphere and their coupling to the magnetosphere, often by making comparisons with satellite-derived data (e.g. from Geos).

ESA is still involved to a small extent in the furtherance of its early sounding-rocket research in that it still maintains a 'Secretariat for the Esrange Special Project', and it periodically co-sponsors symposia at which the science derived from rocket as well as satellite experiments are presented and correlated.